SCUOLA NORMALE SUPERIORE

Ph.D. THESIS

IN BIOPHYSICAL SCIENCES

Advanced nanofabrication techniques and materials for mechanotransduction studies and tissue engineering applications.

CANDIDATE
Cecilia Masciullo

ADVISOR
Marco Cecchini

2019

Cover: Don Shank

"Mind World" (2015, Digital Painting).

FLUCTUAT NEC MERGITUR.

CONTENTS

1 Abstract.

Although peripheral nerves display regenerative abilities compared to the central nervous system, regeneration after centimeters nerve loss is very limited. To date, peripheral nerve injuries represent a major cause for morbidity and disability in the affected patients. Severe nerve lesions might occur at any age and result from many different types of traumas. In particular, young males are often involved in peripheral nerve injuries after car accidents and traumatic limb amputations. The incidence of peripheral nerve injuries lies at about 300,000 cases per year in Europe: the socio-economic impact is therefore high, comparable to diseases such as diabetes (European Commission report, 2016). Moreover, peripheral nerve lesions result to be clinically relevant with an incidence of 2/100,000 persons per year, value recorded only for hand amputation traumas. Hence, there is a considerable need for innovative therapies in the area of repair and regeneration of peripheral nerve injuries.

Nowadays, functional recovery after a nerve injury is achieved through the regeneration of the severed axons and the reinnervation of target tissues. In particular, nerve regeneration is fostered by a set of phenomena at the cellular level that recreate the connection from the proximal up to the distal stump. Nonetheless, a number of factors can interfere with functional recovery, hindering the complete healing of denervated target tissues.

In this context, tissue engineering can substantially enhance the repair of neural tissues through the use of artificial scaffolds. Although standard micro- and nanofabrication techniques have been employed to produce biomimetic scaffolds during the last two decades, it is still difficult to recreate the physiological complexity in an *in vitro* system.

The results reported in this thesis include novel nanofabrication techniques and materials for mechanotransduction studies and tissue engineering applications. In particular, the main topic of my Ph.D. project concerns the development and use of innovative biomaterials and nanoimprint lithography schemes for biomedical applications.

The current work is organized as follows. After this introduction (**Chapter 1**), I will provide a comprehensive overview of the current literature on engineered polymers, identifying the key-features that make them leading candidates to regenerative medicine applications.

In particular, I will focus on fabrication techniques, mechanotransduction processes, peripheral nerve regeneration and neural scaffolds technologies, and nanostructured scaffolds (**Chapter 2**).

In **Chapter 3** I will show the fabrication of novel microstructured phantoms to mimic vascularized tissues for photoacoustic system optimization. I will also investigate the possible use of novel light-responsive hydrogels for biomedical applications. Both of these studies will have the final aim of characterizing novel materials before their *in vivo* experimental tests.

Chapter 4 will be dedicated to the development and use of high-resolution *intermediate molds* for nanoimprint lithography (NIL). In this section I will detail the optimization of perfluoropolyether (PFPE) as a soft mold for NIL, proving enhanced resolution and fidelity of the replica process.

In **Chapter 5** I will demonstrate the applicability of PFPE intermediate molds for the fabrication of transparent and biocompatible cyclic olefin copolymer (COC) and polyethylene terephthalate (PET) scaffolds, patterned with two original types of sub-100 nm topographies, named *nanoripples* and *nanogratings*.

Preliminary results on topographical gradients of directionality will be reported in **Chapter 6**. I carried out this research activity mostly at ETH in Zurich, where I have been involved firsthand in the design of novel micropatterned structures as well as their fabrication, and *in vitro* cell migration assays.

Finally, in **Chapter 7** I will summarize my research achievements, highlighting the contribution of the present work to the complex issue of peripheral nerve regeneration, and their potential for a medium-term clinical translation.

2 Engineered polymers for regenerative medicine applications.

Regenerative medicine is an emerging multidisciplinary field that aims to restore, maintain or enhance tissues and hence organ functions. Regeneration of tissues can be achieved by the synergistic activity of living cells, which will provide biological functionality, and materials, which act as scaffolds to support cell proliferation.

Mammalian cells behave in vivo *in response to the biological signals that they receive from the surrounding environment, which is structured by nanometer-scale components. Therefore, materials used for repairing the human body have to reproduce the correct signals that guide the cells towards the desired behavior. Nowadays, the interest in nanomedicine keeps growing because the application of nanotechnology tools to the structure development at the molecular level improves the interactions between material surfaces and biological entities. Although cells have micrometer dimensions, they evolve in vivo in close contact with the extracellular matrix (**ECM**), a three-dimensional network of extracellular macromolecules, which constitutes the topographical and structural features of nanometric size. The interactions between the cells and the ECM influence the cell growth, guide the cell mobility and affect the general behavior of cells. Nanotechnologies provide the possibility to fabricate surfaces, structures and materials with nanoscale features that can mimic the natural environment of cells and promote functions, such as cell adhesion, motility and differentiation.*

*In this chapter I will focus on aspects of nanotechnology relevant to biomaterials science. Specifically, the fabrication of polymeric materials, such as scaffolds for tissue engineering (**TE**), and the surfaces nanopatterning techniques aimed at eliciting specific biological responses from the host tissue will be addressed. Then, after a brief description of current scaffolding approaches in nerve grafts, I will highlight the role of nano-engineered biomaterial in preliminary* in vitro *studies for nerve regeneration process fulfillment.*

2.1 Selected micro and nano-fabrication techniques for biocompatible materials.

The development of nanotechnology is based on the study of fabrication techniques capable of producing nanometric-size structures rapidly and precisely [1], [2]. In fact, nanofabrication is the process of making functional structures with patterns having minimum dimension lower then 100nm [3], [4], [5].

Normally, fabrication methods used to develop micro and nanostructures are labeled as top-down and bottom-up, according to the process involved [4], [6]. In the bottom-up approaches the surface is structured by the self-assembly of small building blocks such as copolymers, micelles or particles [3]. While these methods afford the large-scale production of monodisperse devices with sub-micrometric size, controlling size, shape, structure and defects on the final devices is not a trivial task. To avoid these limitations, top-down methods were introduced.

Top-down processes aim at creating nanoscale structures with the desired shape starting from large blocks and reducing their size in a controlled way until the required scale is reached [5]. Photolithography and electron beam lithography, hot embossing and nanoimprint lithography are examples of top-down approaches [3].They have shown a great potential in patterning nanostructures, especially ordered arrays [6].

In this section, I shall illustrate top-down approaches to fabricate biocompatible nanostructures, introducing several powerful non-conventional lithographic methods.

2.1.1 *Soft lithography patterning techniques.*

In order to develop biocompatible nanometric features at low cost and overcome some limits of the conventional lithographic methods, new patterning techniques have been explored and developed. All those methods use a patterned stamp, mold or mask to generate polymeric micro/nano patterns or micro/nanostructures [7]. These methods are generally referred to as *soft lithography* techniques, and they have been developed as an alternative to conventional lithography. In fact, soft lithographic techniques are low in capital costs, straightforward to apply, easy to learn. Furthermore, they can generate patterns on non-planar surfaces and can be used with a variety of materials [7].

Examples of these techniques are *Micro-contact printing*, *Micro-molding* in capillaries, *micro-transfer molding*, *replica molding*, *hot embossing*.

Micro-contact printing (**μCP**) [8] is a soft lithographic method which employs a micro/nanopattern elastomeric stamp, typically made in poly (dimethyl siloxane) (**PDMS**), with a chemical ink capable of forming patterns of self-assembled monolayer (**SAMs**) by contact with the target substrate [9]. Although μCP is extremely useful for a wide range of applications, it suffers from the limited resolution in reproducing features in the sub-micron range (from 1 μm to 100 nm).

Replica molding (**REM**) [10] [11] enables faithful duplication of three-dimensional topologies with feature size ≥ 100 nm in a single-step using PDMS molds. They are prepared by casting against rigid masters using a procedure similar to that used in μCP. The relief features on the PDMS mold can, in turn, be faithfully replicated by using this structure as a mold for forming structures in a second ultraviolet (UV)-curable (or thermally curable) prepolymer [10]. The use of an elastomeric mold, rather than a rigid one, simplifies the separation between the replica and the mold. Furthermore, its use reduces the possible damage of the initial mold and it enables faithful duplication of complex microstructures in multiple copies in a simple and inexpensive way [12], [13]. Although μCP and REM are extremely useful for a wide range of applications, particularly for the biomedical ones [14]–[16], their employment in the sub-micron range is hampered by resolution limits. Moreover, stamp deformation during its detachment from the template and during the patterning of the new substrate represents a severe hurdle to the widespread use of these techniques [17],[18]. Additionally, almost all organic solvents induce PDMS swelling, thus changing the feature dimensions [19].

*Micro-molding in capillaries (**MIMIC**) and micro-transfer molding (**mTM**)* are other two soft lithographic techniques which exploit the conformal contact between a PDMS mold and a support to create a network of microstructures.

In the MIMIC case [20], the PDMS mold is placed on the surface of a substrate, forming a network of empty channels. Then, a low-viscosity prepolymer is placed at the open ends of the channels, and this liquid spontaneously fills the channels by capillary force. After curing the prepolymer, the PDMS mold is removed, leaving the patterned microstructures. Interestingly, the very slow filling

for very small capillaries limits its usefulness to structures with a width lower than 2 mm.

In mTM [7], [21], a drop of liquid prepolymer is applied to the patterned surface of a PDMS mold and the excess liquid is removed by scraping with a flat PDMS block or by blowing off with a stream of nitrogen. The filled mold is then placed in contact with a substrate and light radiated or heated. After the liquid precursor has cured to a solid, the mold is carefully peeled away to leave a patterned microstructure on the surface of the substrate. The most significant advantage of mTM over other microlithographic techniques is the ease with which it can fabricate microstructures on nonplanar surfaces, a characteristic that is essential for building three-dimensional microstructures layer by layer.

Although using mTM it becomes possible to obtain multilayer structures and to pattern 100 nm wide features, mold deformation is one of the main challenges that can be encountered. For example, the prepolymers are mainly organic and aqueous materials that must be removed when the liquid is converted into a solid. During the drying and sintering process, the thin film may diverge from the original shape due to shrinkage [22]. For similar reasons, closed loop structures cannot be replicated by microtransfer molding in one single step. This is because as the elastomeric resin pours over the loop and is cured, the loop ends up becoming topologically locked in the elastomer, being unable to be released [23]. Layer by layer fabrication approaches are thus necessary to mold closed loops via microtransfer molding.

2.1.1.1 *Hot embossing.*

Hot embossing of thermoplastics is a cost-effective replication technology to transfer nano/microstructure patterns form a master mold onto a thermoplastic material at set pressure and temperature [24], [25]. In fact, the process is composed by two major steps: heating the mold and the thermoplastic substrate to embossing temperature (*i.e.* above the glass transition temperature $\mathbf{T}_g$ of the thermoplastic polymer) and cooling down to demolding temperature [26], [27]. A thermoplastic material experiences the glassy state, rubbery state and flow state at increasing temperature [28], [29], as shown in **Figure 2.1**. When the operating temperature is

below T_g (glassy state), the deformation given by pressure is ideally elastic [30]. As the temperature goes up (*i.e.* above its T_g and below its melting point $\mathbf{T_f}$), the thermoplastic polymer acts like an incompressible rubber and it softens reversibly when heated, but hardens when cooled back [31]. Finally, with a further increase of temperature, the viscous flow state can be reached and the deformation is thus irreversible in the flow state [28], [29]. Hot embossing is carried out between T_g and T_f.

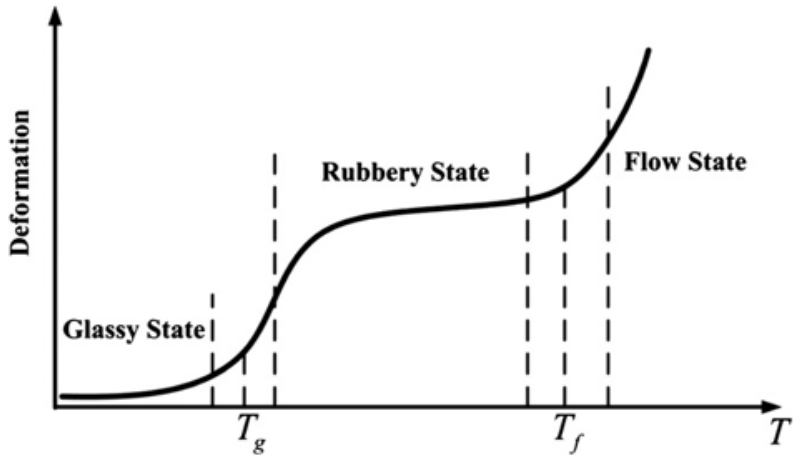

Figure 2.1 **Thermoplastic polymers behavior vs. temperature** in three states: glassy state, rubbery state and flow state. The figure is reported from [25].

By simply changing the disposition or the shape of the molding tool, three different forming principles of micro hot embossing can be distinguished: *plate-to-plate* (**P2P**), *plate-to-roll* (**P2R**), *roll-to-roll* (**R2R**) (**Figure 2.2**).

Among these, P2P is the most conventional method, which contains a mold plate with micro or nanostructures and a substrate plate (**Figure 2.2 a**). Thanks to the high accuracy and controllability of this process, P2P is widely used for industrial production of compact disc (**CD**) and digital versatile disc (**DVD**), as examples. In fact, as relatively mature technology, P2P apparatuses are commercially available and sold by industries as Jenoptik Mikrotechnik GmbH, Wickert Press, Evgroup, SUSS Microtec, Karlsruhe Institute of Technology and Obducat AB [32]–[37].

Nevertheless, P2P is a discontinuous batch-wise mode facing drawbacks of limited efficiency and in some cases rather small replication areas [38], [39]. Moreover, the fabrication of patterns with high aspect ratio (*i.e.* ratio between feature height and width) is limited by demolding-related defects, such as broken

and distorted features. In fact, thermal contraction of polymers is significantly different from that of the molds, usually fabricated in hard materials such as silicon or nickel. As a result, if the cool-down step is not optimized, the thermal capacity mismatch between the two materials generates a large thermal stress during demolding, thus making it difficult to separate polymeric features from the mold. It was demonstrated by Dirckx's group [40] that both adhesion and sidewall friction played a fundamental role in demolding. In particular, coatings such as amorphous silicon carbide and Teflon-like fluoropolymer reduce demolding energy [41]. Unfortunately, long cycle time for heating and cooling as well as low pattern uniformity for very large-areas are unsolved problems that compromise in some cases the overall success of P2P technique. To solve those issues, *rubber-assisted embossing*, *ultrasonic-vibration* and *gas-assisted embossing* strategies were introduced. Briefly, in *rubber-assisted embossing* [42], [43], the thermoplastic film is pressurized between the hard mold surface and a rubber pad, performing the desired conformal contact process.

Ultrasonic-vibration embossing is based on intermolecular friction at the interface between the mold and the imprinted material [44], [45]. Compared with conductive or convective heat transfer, this fabrication method results faster and more efficient.

Recently, gas pressure has been introduced as load during hot embossing (*gas-assisted embossing*) to generate uniform pressure over large areas [46], [47]. It was proved that it is possible to fabricate uniform micro/nanostructures on large polymeric area, up to 18 cm^2 [48].

Therefore, compared to other conventional processes, the hot embossing enables fine-pattern processing using only a stamp. Owing to these advantages, studies on hot embossing have been widely conducted. As example, differently from P2P, where the entire polymer is imprinted simultaneously after heating above Tg, in P2R only the small area in contact with the roller has a temperature higher than Tg, as shown in **Figure 2.2 b**. Moreover, molding and demolding steps are continuously performed, so that the process efficiency depends from fabrication parameters such as imprint pressure and rolling speed, as well as temperature. Normally, features with low aspect ratio imprinted on a low-viscosity polymer have the highest embossing rate, compared to other conditions [49]. Another P2R

configuration relies on putting a flat mold directly on a substrate and rolling a smooth roller on the flat mold as shown in **Figure 2.2 c**.

Furthermore, R2R hot embossing was developed with the aim of increasing the speed of embossing production for micro and nanopatterns [50]. When the substrate is heated to T_g by an induction roller, microstructures on the mold are simultaneously transferred to the substrate surface. If the speed is too high, T_g is not reached and there is no replica on the polymer. On the contrary, the polymer film can be molten and torn apart if the speed is too low [51].

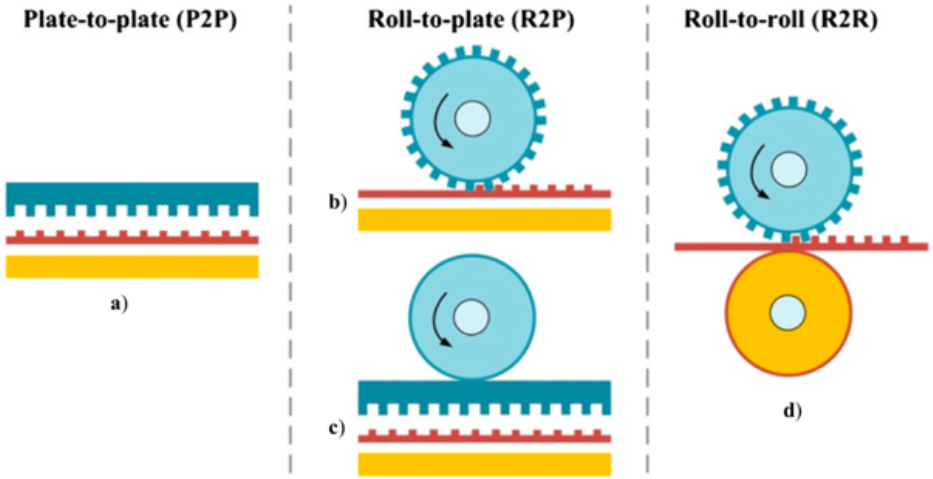

Figure 2.2 **Schematic diagrams of three modes of micro hot embossing.** The schematic of P2P hot embossing is illustrated in a) which contains a micro/nano-structured mold and a substrate plate. b-c) R2P, characterized by a rotation cylinder and a flat plate, is proposed to meet the increasing demand for large-area patterned polymeric films. There are two typical R2P modes: b) rolling a cylindrical micro/nano-structured mold on a flat and solid substrate, or putting a mold in contact with a substrate and rolling a smooth roller on the system, as shown in c). d) The continuous and high-throughput fabrication method for patterned polymeric films is R2R hot embossing, characterized by two rollers with a polymer film in between. The figure is reported from [25].

In order to overcome some limits of the conventional hot embossing techniques as high replacement costs for mold pattern change, Yun and coauthors [52] proposed an *impact-imprint type* hot embossing technique. This new embossing method requires a fine-shaped printing head which applies force onto a heated substrate. The pattern is fabricated by controlling the position of the printing head, dot by dot. The main advantage of this technique is that various patterns can be embossed in real-time but, on the contrary, a mismatch in size of 7 % between final pattern and printing head is observed.

2.1.1.2 Nanoimprint Lithography.

Thermal Nanoimprint Lithography.

In literature, hot embossing and NIL are often used with the same meaning, particularly when the replicated patterns bear sub-micrometric dimensions. The plausible difference between hot embossing and NIL is the thickness of the polymer to be structured: thanks to hot embossing, a bulk material is nanostructured directly on its surface, while NIL process involves the use of a thin thermoplastic film or resist [53], [54].

In particular, for *thermal NIL*, the fabrication principle is based on a nanopatterned hard mold employed to deform a thermoplastic polymer under controlled pressure and temperature, as shown in **Figure 2.3**. The increased polymer temperature reduces the viscosity of the material, so that the applied pressure helps the molten polymer to flow into the cavities. As in a standard hot embossing process, the final cooling of the system freezes the pattern on the target surface, thus providing a negative copy of the master.

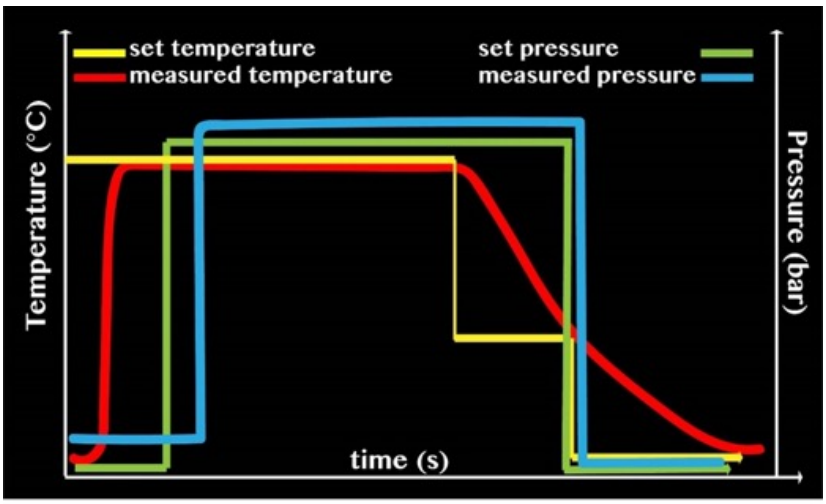

Figure 2.3 **Schematic diagram of a NIL process**. Yellow curve: set temperature, red curve: measured temperature. Green curve: set pressure, cyan curve: measured pressure.

With such technique, Chou et al. [53] achieved a minimum resolution of 25 nm in patterning holes of 25 nm in diameter, spatially separated by a distance of 95 nm,

on a poly(methyl methacrylate) (PMMA) film. More recently, Schvartzman et al [55] imprinted PMMA pillars of 10 nm in diameter.

One of the major challenges related to this technique is the mold lifetime. NIL molds have to be replaced after ~ 50 consecutive imprints or less. In fact, high pressure and heating and cooling cycles cause stress and wear to NIL molds. In particular, the mold can be damaged by polymer attachment on its surface during the imprint process.

To solve this issue, two different methods have been introduced: a hydrophobic coating on the mold surface (*i.e.* silane coating), and the use of hydrophobic polymeric molds, such as PDMS [56], [57], ethylene tetrafluoroethylene (**ETFE**) [58], [59], or PFPE, as I did in [60], [61].

Hydrophobic coating is the standard technique for preserving the integrity of hard molds and polymeric replicas, and for minimizing defects on both surfaces. Furthermore, the remarkable thinness of silane coating (< 2 nm) fosters a strong bonding of the coating onto mold surface [62]. On the other hand, mold breakage remains a problem during the demolding step. In fact, after the NIL process, the rigidity of the hard mold makes it very difficult to clearly separate it from the substrate. Conventionally, a scalpel or a razor blade have been employed to separate the mold from the substrate, but if the detaching procedure is not properly executed, it might introduce mold surface damages and cracks [56].

2.1.1.3 UV-Nanoimprint Lithography.

The ultraviolet NIL (**UV-NIL**) process has several prominent advantages over the thermal NIL, including the capability of U-NIL to be conducted at room temperature without the need of elevated temperature imprinting. Therefore, this helps to eliminate the issues resulting from thermal expansion variations between the mold, substrate and polymeric resist [3], [63].

In particular, an optically transparent mold (made of quartz, indium thin oxide or other UV-transparent materials) [64] is pressed into the polymeric solution at room temperature, and then the solution is polymerized by UV irradiation. Due to the typical low viscosity of the resist, a pressure of few bars (1-5 bars) [65] is sufficient to perform the imprint process. Acrylate formulations are very often used

in UV-NIL processes because of their commercial availability, low viscosity and rapid photopolymerization. On the other hand, the use of acrylates requires an inert atmosphere, since oxygen is a strong radical inhibitor for this process [66]. While UV-NIL offers several advantages, it is important that many parameters such as polymerization time, surface energy of the mold and polymer transparency are carefully evaluated, as they can critically affect the replication and demolding processes. Furthermore, shrinkage is an important factor to be optimized in order to avoid replica cracking during demolding. In fact, during UV curing, the resist volume shrinks. Thanks to a ring opening polymerization, epoxy resist has a very limited shrinkage rate, in general ~ 3 %. On the other hand, acrylates and vinyl-ether resists show shrinkage rates of ~ 10 %. Indeed, due to the thin residual resist thickness and the mechanical rigidity of the substrate, the bottom of the fabricated structures is not able to relax. Consequently, the resist shrinkage will induce a change in the top lateral dimensions and height of the features, reducing their lateral slope. In order to limit the shrinkage, resist formulations are made with monomers presenting a reduced shrinkage. Hence, steric hindrance might be used. Another possibility is to include an oligomer or a polymer in the resist formulation as a binder, but taking into account the increased resist viscosity [67]. In addition, insufficient UV irradiation might cause distortion and structure collapse [68].

2.1.1.4 Step-and-Flash and reverse Nanoimprint Lithography.

Step and Flash nanoImprint Lithography (**SFIL**) is considered to be one of the most promising alternatives to conventional soft lithography techniques. SFIL uses a low viscosity monomer (<5 cPs) that is dispensed as droplets deposited on the substrate, rather than as a spun-on film (**Figure 2.4**) [69].

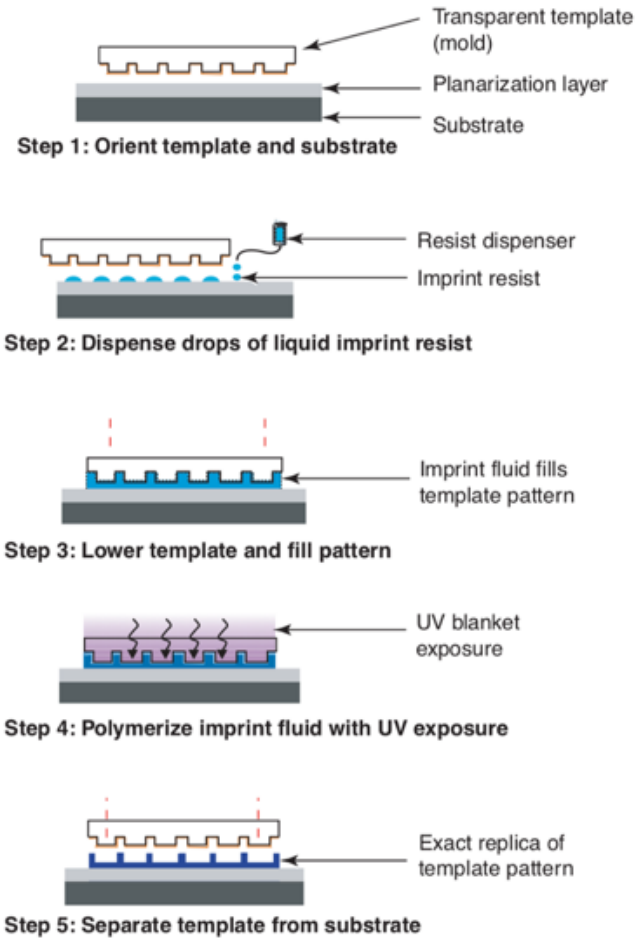

Figure 2.4 **Schematic illustration of SFIL process**. Drops of a low-viscosity monomer are deposited onto the substrate and contacted with the transparent mold, causing the drops to spread, merge and fill the mold. The monomer is UV exposed, and the mold is separated, leaving a replica of the mold pattern. The figure is reported from [70].

A transparent quartz mold with relief nanostructures contacts the monomer, and the drops spread, merge and fill the features in the mold. The monomer is then exposed to UV light via backside illumination, and the patterned structure is left on the substrate when the mold is removed. This process uses the lowest imprint pressures possible (~2 bar), so the low viscosity resists readily flow to fill the recesses of the mold. SFIL offers the opportunity of modifying the material chemistry, drop by drop, when creating the surface pattern.

The advantages of SFIL include feature resolution (limited only by template fabrication), large patterned areas, high throughput, process easiness and

robustness, room temperature and low-pressure processing conditions, device manufacturing costs reduction.

The main drawback is instead the pattern peeling from planarization layer, caused by the demolding process [71]. One successful strategy to avoid the pattern peeling is to reduce the mold surface energy with respect to the substrate one, exploited also for reverse nanoimprinting. Simply, the polymer is spin-coated onto a transparent mold instead of the planarization layer, filling areas of surface relief patterns, then transferred on the planarization layer by one of the NIL techniques [29]. This last technique is particularly useful to transfer patterns on substrates that are not suitable for spin coating [72].

2.1.1.5 Nanoimprint by Melt Processing.

The key difference between nanoimprint by melt processing (**NIMP**) and thermal NIL is that the NIMP process uses low-viscous plasticized polymers in the flow state (as shown in **Figure 2.1**). In the case of NIL, a high-molecular weight polymer is often spun on substrate, then heated to a temperature higher than T_g of the thermoplastic polymer. After the highly viscous polymer has reached the set temperature, the polymer is patterned by pressing the hard mold onto its surface, under high pressure.

The NIMP process begins with a low-molecular weight polymer mixed with a proper plasticizer, chosen for its compatibility with the low-molecular weight polymer and processability. The mixture is suddenly deposited on a base-plate, similarly to the drop of UV curable resist placed on substrate, in the case of UV-NIL. Then, the base-plate temperature is increased so that the polymer melts completely to form a low-viscosity drop.

Owing to the low viscosity of the polymer drop, the pressure required for replica process is typically ten times less than in thermal NIL (~ few bars) and comparable to the one employed for SFIL process. In addition, the lifetime of the mold is much longer, compared to a thermal NIL, since the required pressure is an order of magnitude lower than the standard replica process [52], [65].

2.1.2 *Initiated Chemical vapor deposition polymerization (iCVD).*

Nowadays chemical vapor deposition (**CVD**) is widely applied in microelectronics, optoelectronics and energy conversion industries [73], [74], [75] to produce inorganic thin films and materials, carbon nanotubes and graphene sheets [76], [77]. More recently, CVD was employed also to fabricate and engineer polymeric thin films or hydrogels (*i.e.* polymeric networks that take in and store a considerable amount of water).

In fact, what it is called *initiated chemical vapor deposition polymerization* (iCVD) foresees that volatile monomers and an initiator molecule flow inside a temperature- and vacuum-controlled chamber, as in a standard CVD process. Therefore, the initiator molecule forms radicals, which react with the monomers on the cooled substrate by thermal decomposition [78], UV radiation [79], or plasma treatment [80]. Finally, the CVD polymer forms on the cooled substrate [81].
The iCVD process operates at low surface temperatures (ranging from 20 to 60 °C), promoting monomers absorption on the substrates [82]. The relatively low temperature of the iCVD process is particularly suitable for easily functionalizing hydrogel surfaces, as their chemical structure is fully retained [83].

2.2 Nanotopographies for mechanotransduction studies.

*Nowadays, nanotechnology and the related fabrication techniques ensure the fabrication of biocompatible interfaces, the extracellular matrix (**ECM**), that can reproduce the biomechanical cues that are required for tissue morphogenesis, differentiation and homeostasis. In particular, the microfabrication and nanolithography techniques mentioned in the previous section ensure the development of micrometric and sub-micrometric features on biocompatible materials that can be employed as scaffolds in different tissue regeneration fields.*

*In this section I shall introduce tissue engineering (**TE**) as a combination of engineering methods, materials and biochemical factors to heal or replace a biological tissue. Then, I will thoroughly discuss the role of ECM in the mechanosensing and mechanotransduction processes, with a highlight on its interaction cells.*
In the following, I will briefly review scaffold approaches for TE applications. Starting from the requirements that scaffolds have to provide to mimic the ECM functions, I will then provide a concise presentation of the synthetic and the natural materials already employed as TE scaffolds, together with the latest developments in this field.

2.2.1 *Tissue engineering.*

TE is continuously expanding thanks to the interaction between different research fields such as biology, chemistry, material science, nanotechnology and to the development of novel micro-nano fabrication techniques [84]. The ultimate aim is the implantation of constructs (*i.e. scaffolds*) into the body not only to repair an injury but, in some cases, to replace the function of a failing organ [85].

TE materials have to be as similar as possible to the original environment, in order to mimic tissues for research purposes and that can help regeneration of injured tissues. Regenerative medicine is often used as a synonymous of TE, although regenerative medicine implies the use of stem cells to heal or replace the injured tissue [86].

2.2.2 *The role of ECM in mechanosensing and mechanotransduction.*

As already mentioned, the TE substrates should mimic some critical environmental features of the *in vivo* tissue. In particular, the ECM plays several key biological

functions including providing not only physical sustain and spatial organization to the tissue, but also mechanical and chemical cues to cells [87],thus promoting their proliferation and differentiation [88].

In nature, tissues are composed by both cellular and acellular components: the acellular ones are referred to as ECM. In fact, the structure and composition of ECM widely vary between different tissue types, but the leading components of ECM remain proteoglycans, collagen, laminin and fibronectin proteins. In particular, these proteins are organized in folded domains whose sequences are highly preserved. The cells adhesion receptors, *e.g.* the *integrins*, bind folded domains, thus controlling cell-matrix interaction and transducing signal to cell cytoskeleton [89], [90]. Due to their major role in mechanosensitive processes, the cell-matrix complexes have been studied thoroughly. In fact, integrins, zyxin, talin, vinculin, Src, and focal adhesion kinase, the core components of focal adhesion (**FA**) complexes, deeply influence actin polymerization, cell migration and differentiation [91], [92].

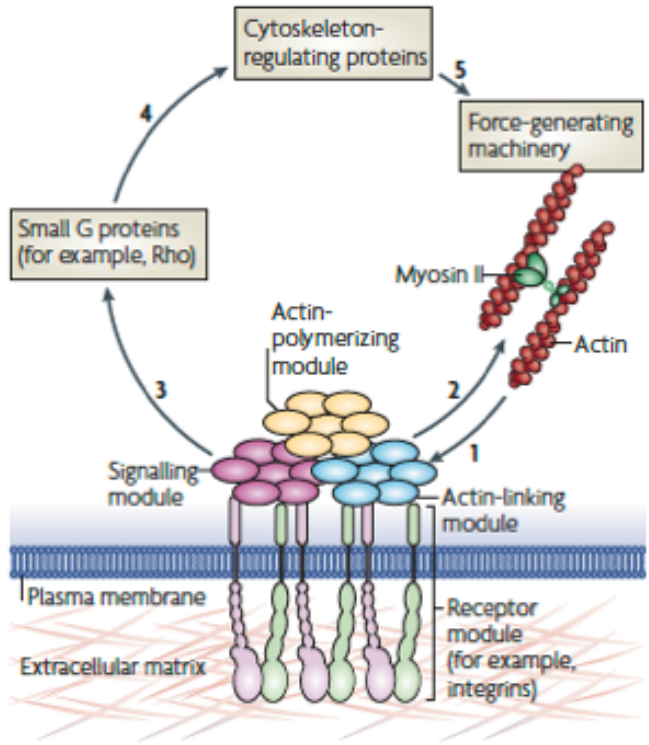

Figure 2.5 **Focal adhesions: structure and function.** Forces that are generated by actin polymerization and myosin II-dependent contractility (step 1) affect specific mechanosensitive proteins in the actin-linking module (talin and vinculin), the receptor module (represented by integrins, and co-receptors, the associated actin-polymerizing module (for example, zyxin) and the signalling module (represented by, for example, focal adhesion kinase). Acting in concert, these interacting modules, with their particular mechanosensitive components, form a mechanoresponsive network. The effect on the actin cytoskeleton (step 2) depends on the integrated response of the entire system to interactions with the matrix and to applied mechanical forces. Stimulation of the signaling module eventually leads to the activation of guanine nucleotide-exchange factors and GTPase-activating proteins, leading to activation or inactivation of small G proteins, such as Rho and Rac (step 3). These G proteins affect actin polymerization and actomyosin contractility through cytoskeleton-regulating proteins (step 4), thus modulating the force-generating machinery (step 5). The figure is reported from [93].

As depicted in **Figure 2.5**, FAs are intersection nodes where the environmental mechanical signals are transduced to intracellular forces and chemical signals through cytoskeletal connections and signaling proteins [94]. In fact, actin cytoskeleton and actin-associated proteins change their physical properties in response to a mechanical stimulus, as in the case of their application on actin network, which can influence myosin and actin activity [95]. Notably, mechanotransduction at FA level is bidirectional: forces are both transduced from ECM to FA adhesion complexes and vice versa [96]. Moreover, integrin

transmembrane adhesion receptors are the primary mechanosensors at FAs level: once a force is applied, FAs change their state from bent to extended, increasing their affinity for ECM ligands [97].

Besides the well-described role of integrin-mediated adhesion in the regulation of cell proliferation, the mechanotransduction process is not just limited to cytosol, yet it comprises also cell nucleus. Among others, the Hippo signaling pathway has emerged as a critical effector process by which changes in cell tension affect cell proliferation [98]. Hippo pathway activation leads to the nuclear exclusion of the mechanosensitive transcriptional activators, namely Yes-Associated Protein (**YAP**) and the transcriptional coactivator (**TAZ**) [99]. In fact, both cell shape and substrate stiffness control Hippo signaling activity, simply by the formation of stress fibers in response to an alteration in substrate stiffness. However, this mechanism is still not well understood.

In recent years, it has become increasingly clear that cellular responses to external signaling cannot be merely determined by the sensing of chemical ligands on ECM, but a wide range of physical cues must also be taken into account [93].

2.2.2.1 Substrate topographies.

Since natural tissues are composed by nano-sized biomolecules and ECM nano-cues, all features with typical dimension around 500 nm or smaller (*e.g.* nanoparticles [100], nanofibers [101], nanogratings [102]) can closely mimic native biological systems, helping cell growth and tissue regeneration.

In 1912 Harrison was the first to show that cell shape and migration were strictly linked to substrate topography [103]. Later, Weiss [104] showed that cells can move and migrate by contact guidance mechanism (*i.e.*, *cell-shape adaptation to the local extracellular environment* [105]).

Since then, many studies were conducted to clarify the cell-substrate interactions on patterned substrates, using different materials, features and cells [106], [107], [108].

Particularly, topographical factors as size, shape and geometry of the single feature can exert strong effects on many cells' behaviors, such as adhesion, migration, alignment and differentiation [109], [110], [111].

Although it is well known that the cell response to topography is strongly dependent on cell type, the influence of topographical size (in terms of width, spacing and depth of features) was found for many cell types. Micro- and nano-topographies regulate the whole cell morphology and spatial distribution, as well as in the subcellular sensing mechanisms [112].

Scaffolds engineered with mimicked-natural topography have been tested to rebuild tissues *in vitro*, such as corneal substitutes [113] and vascular graft [114].

2.2.3 *Scaffolding approaches in TE.*

Since the role of scaffolds in TE is analogous to the ECM functions in native tissues, and those functions are linked to their architectural, biological and mechanical features, a TE scaffold satisfies at least one the following properties:
Biocompatibility: cells must adhere and migrate along the surface and potentially through the scaffold. Moreover, the scaffold must avoid any immune reaction that can reduce healing process or cause rejection by the body [115];
Biodegradability: neither the scaffold material nor its degradation products should provoke inflammation or toxicity when implanted *in vivo* [116];
Porosity: the interconnected pore structure and high pore density ensure the cellular penetration and the adequate diffusion of nutrients to cells. Scaffold porosity also helps diffusion of cell waste and scaffold degradation products out of the scaffold itself. Moreover, cells interact with scaffolds *via* chemical groups (*i.e.* ligand, as Arg-Gly-Asp, the RGD sequence), therefore synthetic pores have to lead a minimal ligand density to allow cell binding [117];
Mechanical properties: the engineered scaffold should have mechanical properties matching the ones of the host tissue and must allow surgical handling during implantation [118].

Over the last two decades, the scaffolding approaches for TE have significantly evolved. In general, biomaterials for TE can be classified in two categories, according to their sources, namely synthetic and natural. However, the use of a decellularized ECM of a tissue is another promising trend, as well as cell sheets with

self-secreted ECM and cell encapsulation in self-assembled hydrogel matrixes, herein reported.

Synthetic scaffolds.

Although many synthetic biomaterials have a regulatory approval from Food and Drug Administration (**FDA**) for their employment in surgery [119], they were far from being the optimal choice for many TE purposes. In fact, their hydrolytic biodegradation releases acids that can be cytotoxic, as in the case of polylactic, polyglycolic and polycaprolactone [120].

One example of optimized synthetic scaffold is **PuraMatrix**™ (3DM, Cambridge, MA), which is composed by synthetic nanofibers of oligopeptide fragments. This scaffold has customizable properties such as injectability, optimal porosity and resorption rates [121].

Natural scaffolds.

Natural scaffold materials can be obtained from their natural source and can be processed to enhance their natural porosity. Those materials can be in their native form, such as ECM from allograft or xenograft, or can be protein-based materials (*e.g.* collagen, fibrin) or polysaccharide-based materials (*e.g.* chitosan, alginate, hyaluronic acid) [122], [123]).

Despite their excellent biocompatibility, natural materials have a limited mechanical rigidity and durability over time: in literature there are several examples of reinforcing strategies, such as development of composites with synthetic materials [124] or photochemical crosslink of the scaffold [125].

Decellularized ECM matrix.

Nowadays, there is an increasing interest in using decellularized tissue matrices from allogenic or xenogeneic tissues, after the removal of antigens but preserving ECM components. Notably, ECM from decellularized tissues is exploited not only for replacing tissues with an analogous structure, as the vessels for the allogenic vascular grafts [126], yet also to replace tissues with different biological function with respect to the native one, as it happens with amnion membrane for peripheral nerve regeneration [127].

By the use of this technique, rapid advancements were obtained with heart, liver and lung tissues [128]. Nevertheless, the methods employed in recellularization of whole-organ scaffolds are typically adaptations of techniques from a wide range of procedures including traditional cell culture, tissue-engineering methods, cell-transplantation therapies. In particular, this process may also lead to an inhomogeneous distribution of the decellularized matrix and the complete removal of cell components may cause an immune response upon implantation [129].

Cell sheets with self-secreted ECM.

In this TE approach, cells secrete their own matrix on thermoresponsive polymers upon confluence and then their controlled detachment is obtained by temperature regulation, which modulates the hydrophobicity of the polymer. Cell sheet engineering method is excellent for epithelium, endothelium and cell-dense tissues [130].

For example, in order to fabricate a 300 μm myocardial patch, this method must be repeated ten times. In fact, each ECM layer is 30 μm-thick, so the main disadvantage of this technique is the fabrication yield [131].

Cell encapsulation in self-assembled hydrogel matrixes.

This fabrication technique combines the scaffold fabrication and cell seeding into a one-step procedure, because living cells are entrapped into the liquid biomaterials (*e.g*. agarose [132], chitosan [133], poly(ethylene) glycol [134] and polyvinyl alcohol [135]) before polymerization starts. The most famous applications of this fabrication

method is xenogenic pancreatic cell transplantation for diabetes [136]. Nevertheless applications for central nervous system and promising anti-angiogenic results with endostatin-transfected cells encapsulated in alginate for the treatment of malignant brain tumors [137] and liver failure [138], have also been reported in the literature [118].

2.3 Scaffolds for nerve regeneration.

*Tissue engineered nerve grafts (**TENGs**) is an emerging approach alternative to the gold standard for peripheral nerve repair, the autologous nerve graft. In fact, spontaneous peripheral nerve repair is nearly incomplete with poor functional recovery, although the peripheral nervous system (**PNS**) has a greater ability of axonal self-regeneration if compared to the central nervous system (**CNS**)* [139].

The nerve autografting remains the gold standard clinical treatment for peripheral nerve defects, but the main disadvantage of this method is the morbidity of the donor site, additional intra- and postoperative risks, the limited graft availability and the limitation of use in motor or mixed (motor and sensory), nerve defects [140]. *Motor nerve grafts are more suitable for these situations, but the benefit does not surpass the disadvantage of sacrificing their initial function* [141].

Nevertheless, the limitations of the autografts have led researchers to develop artificial neural scaffolds as replacements, and overall the artificial scaffold technology have demonstrated promising results. In particular, material scientists have contributed substantially to the sharpening of nerve regeneration processes, by the development of novel fabrication techniques, scaffold architectures and lumen surface modifications. Moreover, growth factor supplements, stem cell transplantation and cell surface glycoengineering could enhance the efficiency of the biomimetic features of neural scaffolds, thus working synergistically for nerve regeneration process fulfillment [142].

*In this section I will briefly highlight the peripheral nerve anatomy and the role of Schwann cells (**SCs**) after an injury. I will then summarize commercial tubes already approved by the Food and Drug Administration (**FDA**) for human use. Starting from nerve guidance channel (**NGC**), considered as the most straightforward strategy for peripheral nerve regeneration, I will then provide a brief review of the synergistic use of the NGCs together with stem cells and growth factor supplementation, besides the use of the metabolic glycoengineering. In the last part of this section I will summarize the role of nanostructures in the PNS regeneration.*

2.3.1 *Peripheral nerves and Wallerian degeneration.*

In order to develop a proper device, neural scaffolds should mimic the anatomy of the peripheral nerves as much as possible.

In fact, in the peripheral nervous system, bundles of nerve fibers or axons conduct information to and from the central nervous system. In myelinated nerve fibers, these axons are surrounded by a myelin sheath composed of concentric layers of SCs, helping to increase neuronal signaling speeds. Those nerve fibers are surrounded by connective tissues (*endoneurium*, *perineurium* and *epineurium*), capillaries and vessels, as shown in **Figure 2.6**.

Particularly, the endoneurium holds axons and SCs together, composing the endoneurium tube, which is surrounded by the connective tissue of perineurium. The perineurium, in turn, is made of collagen fibrils (type I and III) and elastic fibers interspersed between 15 layers of perineurial cells [143], [144]. Both endoneurium and perineurium have a basal lamina made of laminin, fibronectin and proteoglycans. Altogether, the endoneurial tubes, blood vessels and perineurium compose the nerve fascicles covered by the epineurium, with a thickness ranging from 1.3 to 100 μm [145].

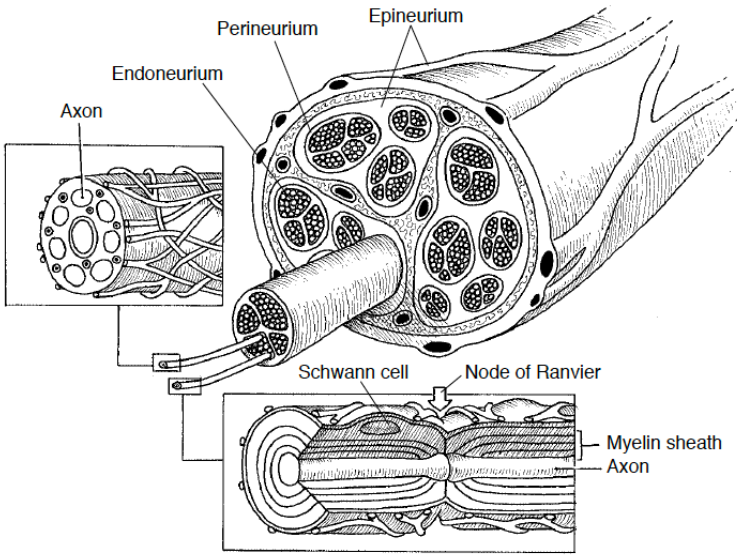

Figure 2.6 **Cross-sectional anatomy of the peripheral nerve.** The left inset shows an unmyelinated fiber. The bottom inset shows a myelinated fiber. The epineurium is the connective tissue layer of the peripheral nerve. Its main function is to nourish and protect the fascicles. The outer layers of the epineurium are condensed into a sheath. Within and through the epineurium lie several fascicles, each surrounded by a perineurial sheath. The perineurial layer is the major contributor to nerve tensile strength. The endoneurium is the innermost loose collagenous matrix within the fascicles. Axons run through the endoneurium and are protected and nourished by this layer. The figure is reported from [146].

The PNS has far greater regeneration potential than the central nervous system mainly due to the different response of the respective glial cells to injuries [147]. In fact, the SCs convert to a regenerative phenotype, thereby promoting the formation of a basal lamina and providing abundant cues to trigger neuronal regenerative response [144].

As depicted in **Figure 2.7**, the distal stump of the injured nerve undergoes a series of molecular and cellular changes known as *Wallerian degeneration* (**Figure 2.7 a**). Within a few hours, both the axon and the myelin in the distal stump degenerate and macrophages migrate to the site of injury and contribute to debris clearance (**Figure 2.7 b**). In the first 24 h, SCs proliferate and switch from a myelinating to a regenerative phenotype and exhibit up-regulation of several molecules that assist the parallel degenerative and regenerative processes.

In particular, when the debris has been removed by the combined action of SCs and macrophages, SCs align forming columns called bands of Büngner (**Figure 2.7 c**). This forms a permissive environment rich in trophic factors, enabling guided axonal regeneration (**Figure 2.7 d**) [148].

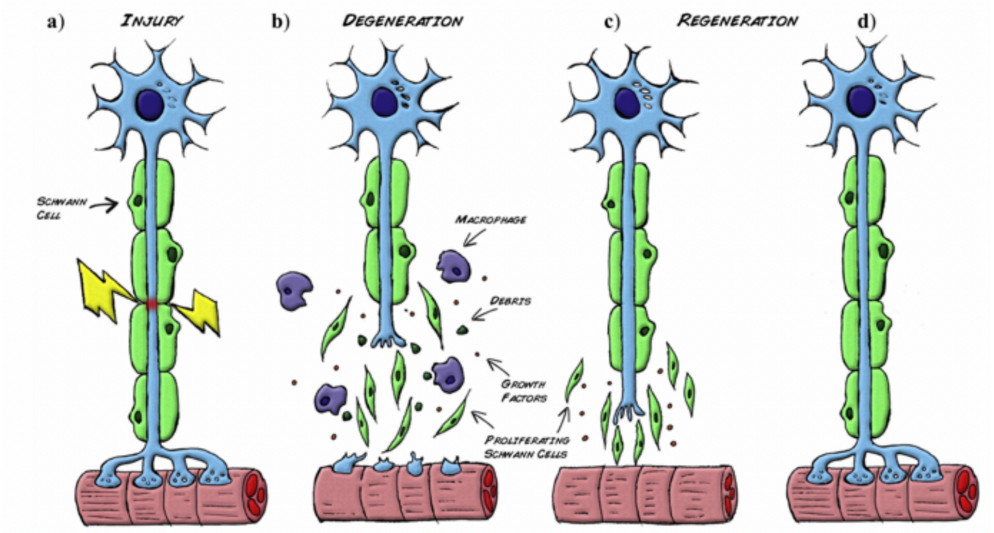

Figure 2.7 **Wallerian degeneration.** a) Following injury, b) Schwann cells detach from the axons, start proliferating and help the recruited macrophages to clear the cellular and myelin debris. c-d) At the same time expression of stimulating factors by SCs create a favorable environment for nerve regrowth towards the target organ. The figure is reported from [148].

2.3.2 *Commercially-available devices and new engineered approaches for neural scaffolds.*

In order to accomplish its role in TENGs, the neural scaffold are designed to guide and protect the injured nerve regrowth and to deliver biochemical cues [149].

To date, various bio-absorbable nerve tubes have been approved by US FDA for human use. Among them, it is worth mentioning the type I-collagen scaffolds ***Neuragen***™, ***NeuroMatrix***™ and ***NeuraWrap***™, the scaffolds based on poly(glycolic acid) (**PGA**), such as ***Neurotube***™, and those fabricated in poly(D,L-lactide-co-e-caprolactone) (**PLCL**): ***Neurolac***™ and ***NeuroMend***™.

Notably, ***Neuragen***™ was the first to be commercialized (2001), it is available in various inner diameters (1.5-7mm) and two different lengths (2 and 3 cm). Compared to more rigid materials (silicone), the ***Neuragen***™ achieved results similar to autograft [150], and it exhibited no compression neuropathy. Moreover, it remained intact up to 4 years post implantation [151]. For PGA-based tubes, ***Neurotube***™ has an internal diameter of 2.3 mm, 4 and 8 mm and length of 2 cm or 4 cm. Its main employment is for digital nerve defects not exceeding 3 mm [152].

In the case of PLCL tubes, Secer and colleagues evaluated 455 patients with ulnar nerve injuries caused by gunshot wounds and treated with ***Neurolac***™.
They found that reinnervation time depends on the severity of the lesion and how far the proximal stump of the ulnar nerve is from the target muscles. Overall, the optimal recovery after the repair of gunshot-inflicted ulnar nerve injuries is strictly dependent on the entity of repair, the time frame from the injury to surgical operation (between 2 to 4 weeks post injury to allow the delineation of proximal and distal stump damage), the surgical approach, and the length of the graft [153].

Despite the promising results in human patients, tube swelling and auto mutilation incidents raised concerns about scaffolds biocompatibility and degradation rate tested on a black hooded rats of 10 mm-long gap injury [154].

2.3.3 *Strategies for an enhanced peripheral nerve regeneration.*

The transition from an engineered biomaterial to optimized neural scaffolds involves two correlated aspects, the scaffold configuration and fabrication, both of which significantly affect the performance of the final scaffold.

Initially, biomaterials were engineered into the simplest configuration, which is a hollow single tube. This scaffold was named NGC, which had an empty lumen. In order to improve the scaffold performance, NGC with an internal micro architecture or an internal multi-component composition within its lumen were fabricated. As an example, one or more intraluminal channels could be introduced to construct a multichannel NGC, thus mimicking the architecture of nerve bundles and reducing dispersion of regenerating axons [155]

Another exploited strategy to improve nerve regeneration is the inclusion of physical fillers into the NGC lumen to mimic the endoneurial structure, typical of autologous nerve grafts [156]. In literature a chitosan-based NGC and PGA intraluminal filaments were employed to bridge a 30 mm-long sciatic nerve gap in dogs, thus enhancing the ingrowth of blood vessels, guiding SCs and allowing diffusion of nutrients [157].

2.3.3.1 Synergy with other peripheral nerve regeneration strategies.

Although NGCs are the main technology for the restore of peripheral nerve activity, they have been shown to be effective only for lesions shorter than 10 mm in rats or 30 mm in primates. If used alone, the scaffold strategy was not successful for larger gaps. Schwann cells, neural stem cells, embryonic stem cells and marrow stromal cells have been the most studied support cells [158]. Moreover, growth factor supplementation, metabolic glycoengineering and modification of the cell surfaces can be also incorporated to optimize the peripheral nerve repair [159], [160].

Stem cell transplantation.

Stem cell transplantation is a widely used strategy for peripheral nerve regeneration. In fact, stem cells can secrete appropriate pro-regenerative factors. Promising examples of stem cell used in peripheral nerve repair are bone marrow mesenchymal stem cells and adipose-derived stem cells.

Bone marrow mesenchymal stem cells (**BMSCs**) are easily obtained through the aspiration of the bone marrow and expanded in large scale by *in vitro* culture. BMSCs have found increasing applications in cell-based therapies, including neural injury. Moreover, autologous SCs are difficult to obtain in large number and

allogenic SCs are involved in immunological reactions [161]. Therefore, BMSCs are becoming a promising alternative to SCs, showing a considerable success in experimental studies with the repair of 50 mm-long gap in dog sciatic nerves [162] and a 50-mm long median nerve gap in rhesus monkeys [163].

Adipose-derived stem cells (**ADSCs**) are superior to BMSCs in some aspects, from their harvesting to their availability. Either undifferentiated or differentiated ADSCs combined with neural scaffolds have bridged peripheral nerve gaps of different lengths, up to 1 cm rat sciatic nerve gap [164], [165], [166]. Pre-clinical studies have demonstrated the role of stem cell transplantation as successful therapy combined with traditional methods of peripheral nerve repair. However, current technologies have yet to identify optimized conditions for clinical use in terms of both efficacy and safety [167].

Growth factor supplementation.

The local presence of growth factors at the injurie sites can play a fundamental role in improving the peripheral nerve injury treatment. Their supportive action may be hindered by the obvious decrease over time of cellular production of growth factors, which makes it necessary the continuous exogenous supply of growth factors. The most commonly used growth factors include brain-derived growth factor, nerve growth factor and glial cell-derived neurotrophic factor [168]. Moreover, these delivery systems ensure positive impacts on nerve reconstruction, in particular they enhance the adsorption of growth factors on the surface or bulk of the scaffold or the entrapment of growth factors during scaffold fabrication [168].

Several studies report different techniques to immobilize *nerve growth factor* (**NGF**) onto scaffolds, among which crosslinking is the most commonly used. In particular, genipin enhances crosslink yield in the case of a scaffold fabricated with chitosan and NGF, further processed into an NGC. After *in vitro* tests [169], an *in vivo* study was subsequently reported where a 10 mm-long rat sciatic nerve was bridged with the aid of this functionalized scaffold [170].

Metabolic Glycoengineering.

A substantial enhancement in the nerve regeneration process can be achieved by improving the interaction between cells and scaffolds. This can be obtained either by acting on scaffolds morphology, or by modifying the biological behavior of the cells themselves.

Metabolic glycoengineering (**MGE**) manipulates the cell biosynthetic pathways of oligosaccharides and glycoconjugates by using sugar analogs [171]. In fact, altering glycans on cell surface may improve cell adhesion and differentiation [172]. Moreover, MGE technique has the ability to alter cell adhesion via the activation of integrins [173]; furthermore carbohydrate-based cell surface modification has been studied *in vivo* [174], demonstrating an improved peripheral nerve regeneration and unleashing its potential for clinical translation.

Nanostructured scaffolds for peripheral nerve regeneration.

As I have already mentioned, the *in vivo* interactions between scaffolds and host cells/tissues are complex and bi-directional: not only the scaffold elicits cell and tissue responses, yet also cells and tissues modify the local environment provided by scaffold itself, through the deposition of ECM molecules [175].

In order to better investigate those mutual interactions, nanoscale topographies were added on the neural scaffold surface. In fact, those nanometric features have the same size of the natural architecture of the ECM cues [176] [177] and induce contact guidance in nerve regeneration. Moreover, nano features promote the adhesion of the surrounding cells to scaffolds and the infiltration of neural and glial processes. Additionally, these features can be arranged to provide topographical cues to guide axons across large injury gaps [178].
As previously discussed, there are three different size scales to take into account for scaffold design: the functional tissue level (>100 μm), the cellular level (1-100 μm) and the subcellular-or nanostructured- one (<1 μm) [179].

Considering these three size scales in tissues, the nanostructured level is the less understood, but it is as relevant as the other two. As an example of nanostructures in PNS, the major ECM component is laminin, which exhibits a typical 70 nm configuration [180]. In literature there are several studies aimed at

eliciting interactions between gratings (anisotropic topographies composed of alternating ridges and grooves) and neural cells. The main goal of those studies has been to orient neurite outgrowth for the establishment of *in vitro* neural networks and the targeted reconnection of axons after injury *in vivo*. As an example, adult sympathetic neurons orient their neurites along the main direction of nanoscale grooves (100 – 400 nm widths, 300 nm depth) [181]; however, 100 nm grooves were less effective at promoting parallel neurite alignment. In addition, smaller neurites (<1 μm) were better aligned than the larger ones.

Comparing microscale and nanoscale widths, two of the most straightforward studies have emphasized that wider and deeper grooves (ridges and grooves with microscale widths) result to orient hippocampal neurites along the main anisotropy direction [182], while narrower and shallower grooves induce a more perpendicular neurite orientation [106].

Furthermore, the topographical effects of nanogratings (ridges width: 350 nm, height: 350 nm) increased the upregulation of neural markers of human mesenchymal cells (**hMSCs**) and, consequently, neuronal differentiation without additional soluble cues, if compared to microscale patterns (ridges width: 1 μm or 10 μm, height: 350 nm) [183].

Nanostructures are mainly incorporated into polymeric-based scaffolds during fabrication processes, aiming to improve their bulk and surface properties by the use of several manufacturing methods, such as electrospinning [184], phase separation and self-assembly [185]. Promising results have been reported concerning *in vitro* studies of polymeric scaffolds patterned with nanogratings for peripheral nerve repair [61], [105], [186]–[188].

3 Novel materials engineered for biomedical applications.

*Cross-disciplinary research has attracted much attention in recent years, and is fundamental for developing advanced biomaterials. In this chapter I will describe the smart design, development and potential biomedical applications of novel biomaterials. More specifically, I will focus my discussion on tissue-mimicking polydimethylsiloxane (**PDMS**) devices and environmentally-sensitive hydrogels. In the case of PDMS devices, by the use of modern nanomaterial technologies and fabrication techniques it became possible to obtain photoacoustic effects by optical interactions at the nanoscale. These systems have the potential to provide cost-effective molecular imaging and therapy in medicine* [189].*Then, I will illustrate a new type of biocompatible and multi-responsive hydrogels* [190], *obtained by initiated Chemical Vapor Deposition (**iCVD**). I will detail the fabrication steps to obtain a hydrogel which couples responsiveness to both light and aqueous environment; hydrogels share many characteristics with living tissues* [191], *such as high water content in the swollen state, porosity, and soft consistency.*

3.1 Microstructured tissue-mimicking phantoms for photoacoustic imaging.

In order to reduce patient's pain, health risks and social costs, the development of non-invasive techniques for diagnostic purposes became necessary. In fact, optical imaging systems coupled with molecular contrast agents are extremely sensitive tools for studying living systems.

In this context, photoacoustic imaging (**PAI**) and therapies are emerging techniques that combine the high-contrast and spectroscopic specificity of optical methods with the spatial resolution of ultrasonic imaging [192], [193]. In PAI, ultrasounds are generated by optical excitation, usually provided by a laser. Particularly, the light is absorbed by endogenous chromophores (*e.g.* hemoglobin, melanin, water or lipids [194]) or exogenous contrast agents, which produce a localized increase of temperature [195]. The consequent thermoelastic expansion generates broadband acoustic waves that can be detected using ultrasounds receivers. Since ultrasounds travel through tissue with minimal scattering and

attenuation, PAI is capable of locating optically absorbing objects deep within tissue, providing advantages over other optical methods.

With the final aim to standardize the PAI performances and compare experimental results, there is a need to develop reference protocols and dedicated test-objects (*i.e.* phantoms) with fine geometry, especially designed for semi-quantitative evaluation of the performance of the PAI system [196]. One of the main issues is mimicking the structure of vascularized tissues for the assessment of suitable contrast agents under different conditions of excitation wavelength, duration of irradiation, dilution, spatial distribution and surrounding material. Tissue mimicking phantoms are especially needed for complete characterization of novel materials prior to the *in vivo* experimental tests [197]. As already mentioned, in order to enhance the sensitivity and spectroscopic specificity of photoacoustic signals, exogenous contrast agents (CAs) are used. CAs are substances chosen for their physical properties (*i.e.* high optical absorption and acoustic emission wavelengths) and interaction with living tissues (*i.e.* minimal interplay with healthy tissues and efficient targeting of diseased ones). The fitness of a CA for a certain application can be defined only in combination with the detection apparatus, testing on phantoms, capable of mimicking soft-tissue properties [198].

The aim of those two works was to design and develop PDMS device composed by micrometric channels for a semi quantitative evaluation of the performance of a PAI system using nano-sized contrast agents (*i.e.* gold nanorods GNRs). Thereafter, tissue mimicking PDMS phantom was designed and tested adding titanium dioxide and black ink, enabling the optical absorption and scattering coefficients to be similar to those of biological tissues.

3.1.1 *Microfluidic phantoms.*

The devices presented here are microfluidic chips engineered to mimic the mechanical, topographical, absorption and scattering properties of vascularized soft-tissues.

The devices were fabricated by means of standard PDMS soft lithography using a SU8 custom-made mold (see ***Materials and methods*** section of this chapter for additional details). The fluidic layer is composed by six parallel channels whose lateral size varies from 50 to 500 μm, comparable with those of the tiniest fluidic

elements found in human bodies (*i.e.* the blood vessels composing the microcirculation [199]).

In particular, the microchannels have a lateral size of 50, 100, 200, 300, 400 and 500 μm (**Figure 3.1 a**), and a thickness of 50 μm. The optical and acoustic properties of PDMS make it a suitable material for PAI, because its optical transparency leads to low attenuation during optical excitation and its acoustic impedance (parameter derived from the mass density of the material and the velocity of the acoustic wave in it) is comparable with those of soft tissues [200]. In the first case [198], the microchannels were loaded with 87 nM solution of GNRs in water. **Figure 3.1 b** shows the quantification of the photoacoustic signal collected as a function of channel width, for all the six channels. As expected, the signal increased linearly with the width of the channel. In this particular chip, the signal from the 50 μm-channel could not be detected, suggesting that the detection limit was reached.

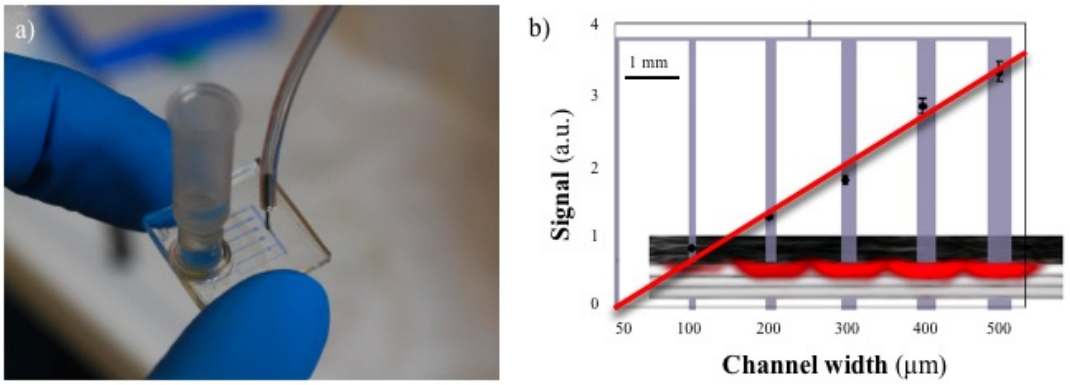

Figure 3.1 **PDMS microfluidic phantom**. a) Picture of the microfluidic phantom. b) Plot of the intensity photoacoustic signal and linear fit of the distribution (red line). The ultrasonic signal (grayscale) present both with or without adding CAs to the channel, is superimposed to the PAI (red bands) one. The geometry of the microchannel network is represented in blue, the width and the spacing of the channels is in scale with the PAI. The figure is adapted from [201].

Then, a tissue mimicking-PDMS phantom was fabricated by adding titanium dioxide (TiO_2, 0.73 mg/ mL) to the curing agent and black India ink (0.25 mg/ mL) to the pre-polymer. The absorption spectrum of a region of mouse spleen at 2 mm of depth under the skin with PDMS was compared to the tissue mimicking-PDMS

phantom. It was found that the tissue mimicking-PDMS generates a higher PAI signal with respect to the PDMS one.

Therefore, PAI signal generated by the tissue mimicking-PDMS, unlike PDMS, can be considered as comparable to that of biological tissue.

Since tissue mimicking-PDMS phantom imitates biological tissue without any CAs, a thin tissue mimicking-PDMS layer (50 x 10 x 3 mm^3) [197] was coupled together with the PDMS phantom and GNRs. It was found that the acquired GNRs absorption spectrum is in agreement with the one acquired by the spectrophotometer. In fact, the thin tissue mimicking-PDMS layer helps distinguishing the typical GNRs absorbance signal.

3.1.2 *Conclusions.*

Here, I have proposed novel microfluidics PDMS phantoms conceived for photoacoustic applications. Since there are no-well standardized approaches for evaluating PAI system quality, my efforts have been directed at evaluating critical parameters such as the phantoms material and the spatial resolution. In particular, the reduced size of the chip and the precise control over channel-network geometry allows for a great versatility in modeling the structure of vascularized tissues.

A further improvement to PDMS phantom was given by adding titanium dioxide and black India ink to the PDMS mixture, so that the absorption and reduced scattering coefficients were tuned in order to be similar to those of biological tissues, as in reference [202]. Overall, phantom devices possess intriguing features that make them promising tools for the construction of phantoms for PAI.

3.2 Novel Light-Responsive Biocompatible Hydrogels Produced by Initiated Chemical Vapor Deposition.

The hydrogels presented in this section are multi-responsive hydrogels synthetized by iCVD. The possibility to control the degree and rate of swelling by light irradiation was never investigated before this work and can be employed for drug delivery or microfluidic systems, as well as tissue engineering devices.

Hydrogels are known for their dynamic swelling response to aqueous environments. The swelling in water result in changes in hydrogel mechanical properties, protein adsorption capabilities and hydrophilicity of the polymer [203], [204] ,[205]. Because of their high water content in the swollen state, porosity, and soft consistency, hydrogels have many characteristics similar to those of living tissue [191].

The aim of this study was to develop a light-responsive hydrogel, which coupling responsiveness to both light and aqueous environment. The light-responsive hydrogels fabricated and tested in this work were obtained by iCVD.

A peculiar feature of iCVD is that delicate surfaces, such as hydrogels or molecular layers, can be easily functionalized without damages to the structure. The iCVD process started from the deposition of a copolymer p-HEMA and ethylenglycoldimethacrylate EGDMA (**p-HEMA-co-EGDMA**), followed by the deposition of a top layer of a polymer of pentafluorophenyl acrylate (**p-PFPA**). The p-PFPA layer can be further functionalized with aminobenzene group as depicted in **Figure 3.2**. The isomerization of the azobenzene group under UV light induced a significant polarity change and the possibility to control the water uptake in the hydrogel film.

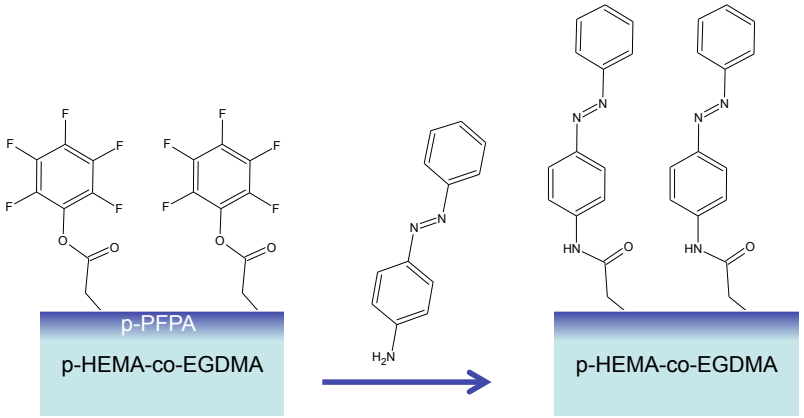

Figure 3.2 **Post-deposition functionalization of the hydrogels to covalently bind light-responsive azobenzene groups.**

The conversion of PFPA to azobenzene is more evident in the X-ray photoelectron spectroscopy (**XPS**) data reported in Figure 3.3. The decrease in % Fluorine is much stronger for the hydrogels top-coated with PFPA than for the homogenous copolymer that has PFPA incorporated throughout the hydrogel matrix. This suggests that the functionalized homogeneous copolymer contains a significant fraction of unreacted PFPA.

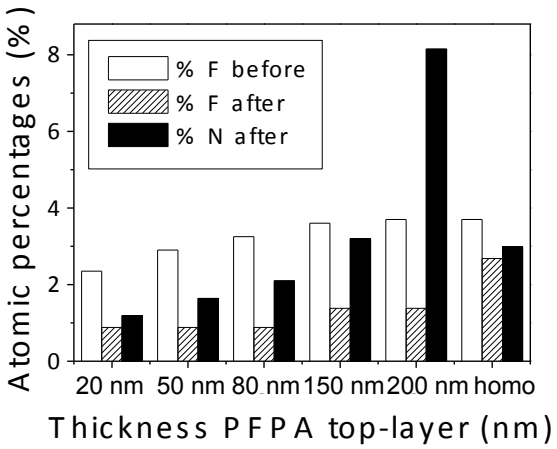

Figure 3.3 **Chemical analysis of the hydrogels before and after aminoazobenzene functionalization.** For different PFPA top-layer thickness, the surface atomic percentages of F and N as measured from XPS for all the samples. The label "homo" refers to the sample with homogeneous content of PFPA.

In order to observe the dynamic and reversible isomerization of the azobenzene, the thickness increase was measured *in-situ* during humidity and illumination cycles. The relative humidity (**RH**) can be continuously increased and decreased over 10 cycles from 82% to 50%, without having to stop the measurement and dry the sample, as it would have been required for measurements in aqueous environment. For the first three cycles, the sample was not illuminated. The thickness in this time-frame increased and decreased following the humidity stimulus, showing the reversibility of the polymer swelling upon exposure to humid air. Afterward, for each humidity cycle, the sample was exposed first to UV light and then to visible light, as shown in **Figure 3.4**.

The humidity and the light exposure affected a reversible change in the swelling of the hydrogels. The maxima of swelling, corresponding to the maxima of RH, were higher upon UV light exposure and went back to almost the original position upon exposure to green light.

It is noteworthy noticing that after several humidity and illumination cycles the thickness oscillated always in the same range: from 362 nm at RH= 50% to 375 nm at RH=82% upon UV-exposure. This reversibility speaks also for the stability of the hydrogel meshes in the time frame of the experiments.

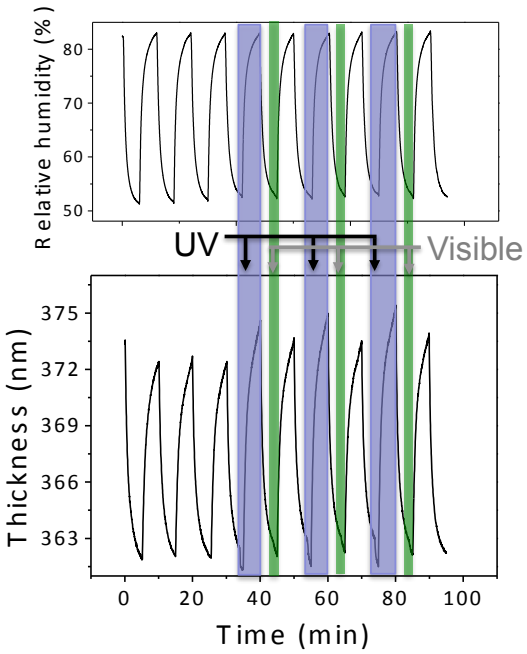

Figure 3.4 **Plot of the hydrogel thickness in time, upon exposure to humid air and to UV-visible light cycles.** The hydrogel, taken as representative, had 12% of azobenzene on the surface. The thick blue areas indicate the period of time in which the hydrogels were exposed to UV light and the thin green areas the time frames of visible light exposure. On top, the corresponding relative humidity oscillations are plotted as a function of time.

3.2.1 *Hydrogels cytocompatibility tests.*

Finally, to investigate a possible use for biomedical applications, the light-responsive hydrogels were tested to investigate their cytocompatibility, since pHEMA component is well-known as a synthetic biocompatible material useful for contact lens applications [206]. Three types of azobenzene functionalization were tested (*i.e.* homo, 12%, and 8%) with Rat Embryo Fibroblast (**REF**) cells, which were also previously grown on pHEMA substrates.

The choiche of REF cells relies on the successfull employment of this cell line in cytocompatibility assays, as reported by Lydon [207]. Moreover, there is a strong correlation between SCs and fibroblasts in the PNS.

In fact, upon a nerve cut, SCs dedifferentiate to a progenitor or stem cell state, proliferate and migrate into the nerve wound forming an environment that is supportive for axonal growth; they produce trophic factors to support the injured axons and prevent the neurons from undergoing apoptosis. Fibroblasts accumulate at the nerve wound and secrete proteins that promote scar formation, angiogenesis,

and inflammation [208]. In particular, the ephrin-B/EphB2 signaling between the two cell types results in cell sorting, followed by a directional collective cell migration of SCs out of the nerve stumps to guide the regrowing axons across the wound [209].

REF cells cultured on our novel hydrogels preserved their morphological phenotype, as shown in the bright-field microscopy images reported in **Figure 3.5**: their natural spindle shape was indeed retained, with a branched cytoplasm surrounding the elliptical nucleus. After 3 h from seeding (D0), the cells were mostly scattered on the surface of the hydrogels. Conversely, after 24 h (D1), the substrates showed to be crowded by REF cells, and from 72 h after seeding, the REFs locally formed clusters, maintaining their normal shape and proliferating until 96h (D4).

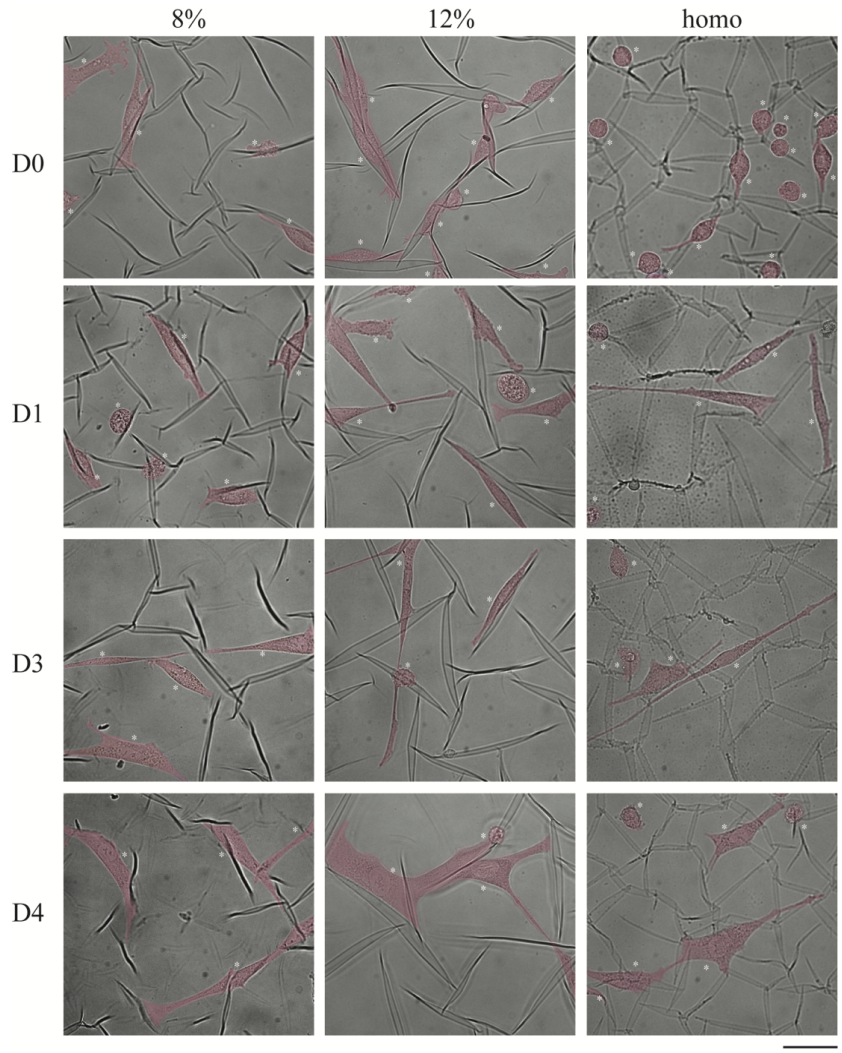

Figure 3.5 **Bright field images of REFs** (highlighted with a red-shadow mask and white stars) **cultured on top of light-responsive hydrogels** with three different surfaces percentage of azobenzene 8% , 12% and the homo-type, at 3 hour (D0), one day (D1), three days (D1) and four days (D4) after seeding. Scale bar: 50μm.

This healthy behavior was confirmed by the viability tests reported in **Figure 3.6**. After 3 h from seeding (D0), the REF cells found difficulties to adhere on the hydrogel surfaces rather than the plate control, in fact the intensity of WST signal produced by viable cells was lower. The fibroblasts started to adhere on top of the light-responsive hydrogels after 24 h (D1) from seeding, suggesting that REF cells were able to recover the initial decrease in viability, since the number of viable cells present on all type of hydrogels was comparable with the control plate. This positive

trend was maintained until the final time point of this experiment, *i.e.*, t = 96 h. Here, REFs cells increased their viability over 150% with respect to the plate value at D0.

All of this evidence lets us conclude that the light-responsive hydrogels are not cytotoxic for this cell line, namely the interaction with the biomaterial did not cause cell death or alterations of the cell morphotype.

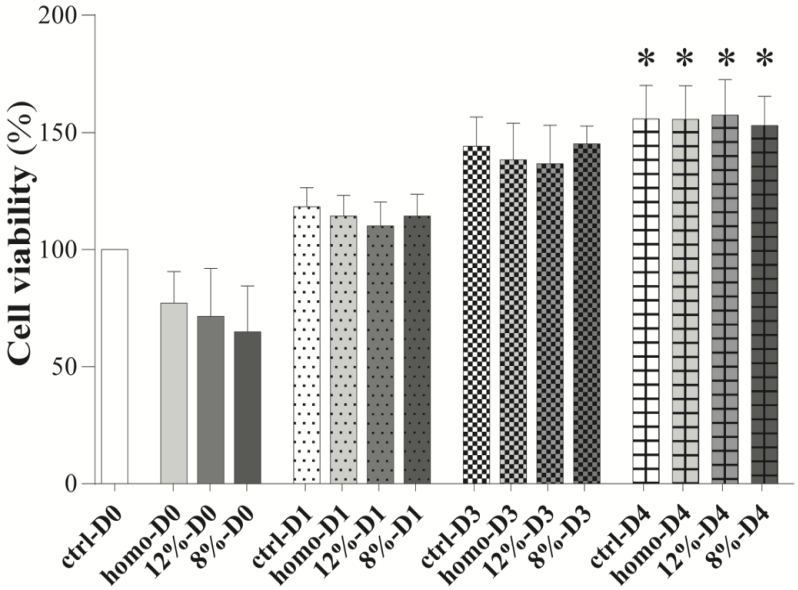

Figure 3.6 **REFs viability *vs.* different hydrogel substrates** at different time points as result of the WST essay, mean ± SEM, *P<0.05, One-Way ANOVA, Dunnett's multiple comparisons test *vs.* plate control at 3h from seeding (ctrl-D0).

3.2.2 *Conclusions.*

The multi-responsive hydrogels fabricated by iCVD here proposed performed their dynamic swelling response to aqueous environments and in response to UV light. This latter behavior is caused by the photoisomerization of azobenzene functionalization upon UV light exposure and was demonstrated both in aqueous and humid environment. The hydrogel biocompatibility was also tested. REF cells showed the same growth rate and morphotype that was shown by the same cell line on the control plate. I do believe that the reversible stimuli responsiveness of the material can definitely be used for biotechnology, light-controlled cell growth, or light-controlled drug delivery.

3.3 Materials and Methods.

Microfluidic phantoms.

The PDMS phantom is a custom PDMS microfluidic device composed of six parallel channels with sizes varying from 50 to 500 μm (in particular, 50, 100, 200, 300, 400, and 500 μm) and a thickness of 50 μm. The device was prepared by standard soft lithography. PDMS (Sylgard 184, Midland, Michigan, US) was prepared by mixing the prepolymer and the curing agent at a ratio of 10:1, pouring it into a custom-made microstructured mold, degassing to remove air bubbles, and baking at 80°C for 1 h.

The replica was cut with a scalpel and removed from the master mold, and fluidic accesses to the microchannels were set up using a 0.75 mm Harris Uni-Core puncher. Subsequently, the floor of the channels was created by sealing the device to a glass coverslip. This process was done by activating the two surfaces using oxygen plasma (25 s, $1.4e^{-1}$ mbar, 10 W for the PDMS and 60 s, $1.4e^{-1}$ mbar, 100 W for the glass) and bringing them in conformal contact immediately after the treatment. A covalent bonding was formed in ~1 h, preventing leakages of liquid during liquid actuation.

The PDMS phantom with microfluidic patterns could be cleaned with water and some acidic or organic solvents, but due to the micrometric channels, we cannot exclude a residual contamination, particularly when using nano-sized materials, such as GNRs.

The TM-PDMS phantom was fabricated by adding TiO2 (0.73 mg /mL) to the curing agent and India ink (0.25 mg /mL) to the silicone.
Both PDMS and TM-PDMS were stable over the duration of testing (approximately one month).

Gold Nanorods.

The GNRs presented in this chapter section were produced by the group of Dr. Ratto as described in detail in reference [198].

The GNRs were fabricated by autocatalytic reduction of chloroauric acid using ascorbic acid in combination with cetrimonium bromide, silver nitrate and gold nuclei. The nanoparticles were then grafted with poly (ethylene glycol) (PEG)

in a 100 mM acetate buffer (pH 5.0) containing 50 μM alpha mercapto omega methoxy PEG strands (molecular weight of ~5000 g mol^{-1}). Finally, the particles were transferred into ultrapure water at a nominal concentration of 20 mM Au (116 nM nanoparticles).

Hydrogel synthesis and characterization.

The polymer coatings here presented were fabricated and characterized by the group of prof. Coclite as described in detail in reference [82].

Briefly, p2-Hydroxyethyl methacrylate (HEMA, 97%, Aldrich, Germany) and Ethylene glycol dimethacrylate (EGDMA, 98%, Aldrich, Germany) with a top layer of Pentafluorophenyl Acrylate (PFPA, 98%, TCI, Germany) were deposited in a custom-build iCVD chamber on Silicon wafer.

Then the copolymer of HEMA and EGDMA (p-HEMA-co-EGDMA) was deposited up to a nominal thickness of 200 nm. Later, the flow of HEMA and EGDMA were turned off and the PFPA one was opened. Different deposition times of the p-PFPA layer were used, which turned in different nominal thicknesses of the PFPA layer, estimated from laser interferometry.

A post-deposition functionalization was performed on all the samples, to substitute the pentafluorophenyl groups with azobenzene moieties. For this purpose, the samples were immersed for 24h in a 20 mM solution of 4-Aminoazobenzene (Sigma Aldrich) in ethanol and then rinsed with ethanol and water to eliminated unreacted chemicals.

The chemical composition and structure of the polymers were evaluated by Fourier transform infrared (FT-IR) spectroscopy in transmission. The atomic composition of the polymers was determined by XPS.

The UV-Vis absorption spectra of the samples containing azobenzene were measured with a spectrometer before and after illumination at 365 nm with a blue LED to measure the isomerization trans-cis. After this, the samples were illuminated with green LED and positioned in the spectrometer to measure the kinetics of the stimulated cis-trans isomerization. The film thickness and the swelling in water and humidity were measured with spectroscopic ellipsometry.

The increase in thickness upon water immersion was measured for 4-5 min with a time resolution of 2 s, before and after sample illumination with a LED light. The

swelling in humidity was measured by flowing water vapor at RH=85%. Also in this case the data were collected with a time resolution of 2s.

Cell culture and viability tests.

In order to perform biocompatibility tests, the hydrogels were deposited directly on WillCo plates (GWST-3522) and sterilized for 10 minutes under UV tissue culture hood.

Rat Embryo Fibroblast cell line (REF cells) were seeded on top of three different types of hydrogels at density of 10×10^3 cells cm^{-2} and cultured under standard cell culture conditions (see other details in reference [82].

REF cell viability was evaluated at 3 h (D0), 24h (D1), 72h (D3) and 92h (D4) after seeding was measured by the 2-(2-methoxy-4-nitrophenyl)-3-(4-nitrophenyl)-5-(2,4-disulfophenyl)-2H-tetrazolium-monosodium salt (WST-8) assay (Sigma, #96992). REF cells were incubated in a 10% WST-8 solution (in medium) in a CO_2 incubator for 3 hours. The supernatant was carefully aspirated, transferred to a new plate, and the absorbance of each well was observed by a plate reader at a wavelength of 450 nm. The absorbance of formazan produced was directly proportional to the number of living cells.

Bright field Microscopy.

In order to confirm REF cells healthy behavior, we seeded REF cells at the same concentration on three types of hydrogels grown on top of WillCo dishes and then imaged at four different times (3h-96h). An Eclipse Ti inverted microscope (Nikon, Japan) equipped with a perfect focus system, an incubating chamber (Okolab, Italy) and a CCD ORCA R2 (Hamamatsu, Japan) was used with an 40x oil objective (N.A.: 1.30).

Statistical analysis.

All the experiments were repeated at least three times independently for each condition. Data are reported as the average value ± the standard error of the mean (mean ± SEM). Data were statistically analyzed by using GraphPad Prism commercial software (GraphPad Prism, 6.05 version). The mean values obtained in each repeated experiment were assumed to be normally distributed about the true

mean. One-way ANOVA (Dunnett's multiple comparison test) analysis was used, unless differently stated, to compare light-responsive hydrogels to the plate control condition. Statistical significance refers to results where $P < 0.05$ was obtained.

4 Intermediate Molds for Nanoimprint Lithography.

*Thermal nanoimprint lithography (**NIL**) is a high-throughput and low-cost soft lithography technique by which a surface pattern on a typically hard mold is physically imprinted into a thermoplastic material, which is often a polymer. Usually, high-resolution and large-area NIL molds are expensive and difficult to fabricate. Even though they are typically made of silicon or other hard materials like nickel or quartz, after a small number of imprinting cycles, they start cracking and, therefore, become unusable. Hence, one of the major challenges to date is increasing mold lifetime. In fact, high pressure and heating and cooling cycles cause stress and wear on NIL molds.*

*In this chapter I will introduce the concept of flexible and hydrophobic polymeric molds as intermediate molds, fabricated to preserve the initial mold and to improve the replica process throughput. To this end, I show an innovative two-step NIL process based on the use of a perfluoropolyether (**PFPE**) intermediate mold, to replicate sub-100 nm features from a silicon mold to the final thermoplastic material, Cyclic Olefin Copolymer (**COC**).*

4.1 PFPE intermediate molds for high-resolution Thermal NIL.

Intermediate molds are replicas of the original mold that are themselves used as molds to transfer micro or nanotopographies to the final material. This type of molds is mostly produced in plastic or soft materials by soft-lithography techniques and must guarantee high-fidelity copies and a sufficiently high number of processes before undergoing degradation [6]. Beyond the ease of fabrication, elastomeric materials can ensure good elastic adaptation and conformal contact with the substrate, which leads to intimate contact without voids [17].

The use of soft molds in replica molding processes has garnered much interest as a ubiquitous and versatile nanofabrication technique.

PDMS is widely used as soft-mold material because of its low surface energy and mechanical properties, which allow conformal contact and easy release from the initial mold and the final imprinted film [56], [210]. PDMS is also UV-transparent and has a very low Young's modulus (1.5 MPa) which gives it the flexibility required for a conformal contact, even over surface irregularities, without the risk of cracking [211]. However, the low Young's modulus of PDMS often limits

the replica process if the topographies are very small (*i.e.* hundreds of nm or less) and with high spatial density, which results in the feature collapses, for the most commonly used commercially avaible form of this material (Dow Corning Sylgard 184) [211]. Furthermore, PDMS often degrades after a few cycles of patterning [56], [207] and, more in general, PDMS-based elastomers swell significantly when exposed to most oil-soluble organic compounds [212].

Resistance to swelling is critically important in nearly all soft lithographic techniques where a mold is brought into contact with a small amount of curable organic monomer or resin and many of the organic liquids desirable to be molded. As the last drawback, PDMS exhibits poor solvent resistance and requires fluorination steps to allow for mold release [211].

Several types of PDMS materials have been developed to improve soft mold performances and overcome the disadvantages associated with Sylgard 184. Schmid et al. first developed a higher modulus h-PDMS (E ~ 9 MPa). Though the h-PDMS showed better resolution than the traditional Sylgard 184 for μCP, the molds were brittle and susceptible to cracking and delamination. On the other hand, Rogers et al. developed a photocurable version of PDMS (UV-PDMS) to overcome deformations associated with thermal curing of stamps. UV-PDMS mold materials successfully replicate 300 nm width by 300 nm spacing by 600 nm height lines that could not be replicated in either Sylgard 184 (feature collapse failure) or h-PDMS (fracture failure) [213], but this requires two subsequent steps of fabrication.

In addition to siloxane-based polymers, a variety of polymeric stamp materials have emerged that show increased resolution and material compatibility:

- Campos et al. recently reported the use of a photocurable poly[(3-mercaptopropyl)-methylsiloxane] (PMMS) thiolene-based mold to pattern sub-100 nm structures using a nanoimprint technique [214];
- Williams et al. report the use of a nanoimprint composite molding technique that features a high-modulus acrylate-based molding material used to

pattern 15 nm features separated by ~90 nm. The flexible composite molds were also used to pattern 100 nm lines onto curved surfaces [215].

Even though these newly-developed mold materials represent exciting alternatives to traditional siloxane-based elastomers, the acrylate and PMMS based molds still require fluorine functionalization for nondestructive release. Additionally, the acrylate-based molds cannot be used to pattern acrylate-based photoresists, and require a cumbersome mold fabrication procedure .

As already mentioned, in replica molding is quite common to functionalize the surface of the master mold to lower the surface energy and to allow the release of the mold without feature desruption [216].

PFPE-based elastomers are a unique class of fluorinated polymers whose structure is formed by linear chains based on multiple strong carbon-fluorine bonds, which entail high stiffness and temperature resistance. Prior curing, fluoropolymers are viscous liquids at room temperature and are characterized by very low surface energy. This facilitates the filling of nanoscale cavities and guarantees an anti-adhesive behavior [216].

PFPEs are inert and exhibit high durability and toughness, high gas permeability, and low toxicity [217], with additional features of chemical and thermal stability. These characteristics minimize degradation under use and provide good lubricity, which reduces the contact surface wear. PFPE-based elastomers are, therefore, promising for NIL but only very rarely used to this end. In particular, the De Simone laboratory pioneered the use of PFPE materials as an alternative to PDMS for microfluidic and soft lithography applications [211], [218].

Moreover, in recent literature it was found that PFPE replica was exploited as intermediate mold as spun film on a silicon substrate. The authors found that PFPE molds could successfully transfer the grating pattern and also replicate the roughness present along the 100 nm-width ridges. For this reason, they speculated that PFPE could in principle be suitable for features with dimension far beyond 100 nm.

Here, it was illustrated and characterized the two-step process based on the use of a free-standing patterned film of PFPE employed as intermediate mold. Moreover, we compared standard molds made of PDMS with PFPE elastomeric molds, which demonstrate better resolution and fidelity of the replica process. Lastly, test PFPE molds were tested for transferring isolated grooves and ridges with sub-100-nm lateral dimension on **COC** [219].

4.1.1 *PFPE intermediate mold: fabrication protocol.*

The initial mold fabrication step starts mixing PFPE resin and a photo-initiator, then pouring the mixture on top of the mold. Following UV-light crosslinking, the PFPE intermediate molds are obtained in less than three minutes (**Figure 4.1**).

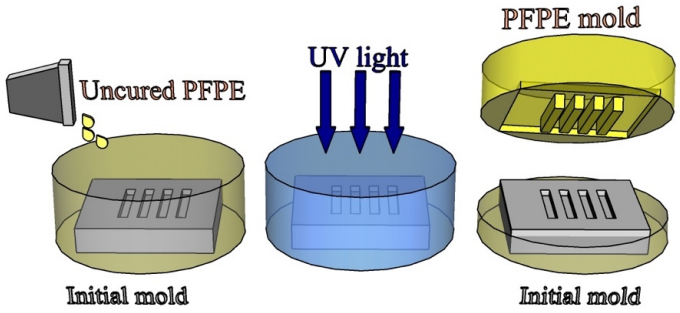

Figure 4.1 **Schematic illustration of PFPE intermediate mold fabrication.**

Our fabrication protocol provides PFPE elastomeric replicas of ≈ 3 mm thickness with a Young's modulus of about 10 MPa [220]. This value made it suitable for standard imprinting protocols (pressures of tens of bars) and did not lead to cracking issues during mold-replica detachment. If necessary, the final thickness of PFPE is customizable by varying the volume of the mixture poured on top of the mold.

Moreover, PFPE wettability was evaluated by performing water contact angle measurements. The contact angle was 93 ± 5°, which was in line with what was reported by other authors for PFPE substrates [221].

4.1.2 *PDMS and PFPE as Intermediate Mold: a performance comparison.*

As already stated, PDMS is often used as an elastic stamp to transfer micro-patterns or nano-patterns using NIL or soft lithography techniques. It is well known that features of several hundreds of nm in close proximity and with high spatial density are challenging to be replicated over large areas in elastomeric materials. For this reason, this kind of pattern was chosen to compare PDMS and PFPE performances. **Figures 4.2 a–c** report representative scanning electron microscope (**SEM**) images of the initial mold and of PDMS and PFPE replicas, respectively.

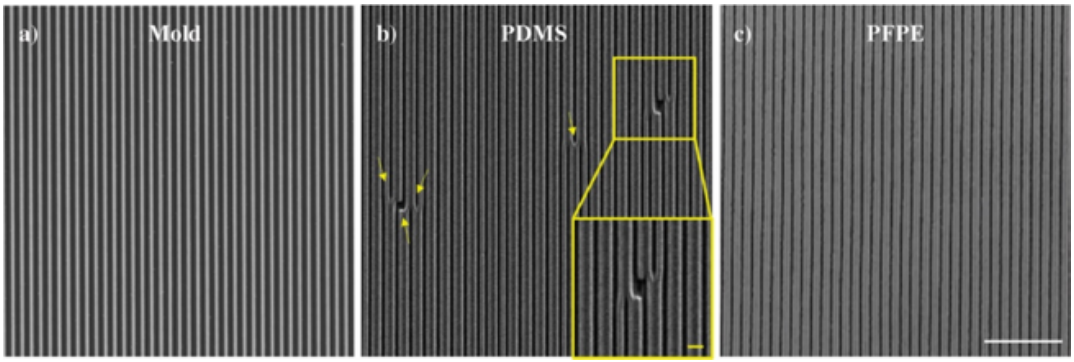

Figure 4.2 **Scanning electron microscope representative images of the 600 nm-periodic nano-grating pattern:** a) initial mold, b) the PDMS replica, and c) the PFPE replica. Scale bar: 5 μm. Yellow arrows highlight the presence of defects in the PDMS replica. Inset of b) zoomed image of a representative area with defects, scale bar = 1 μm.

As highlighted in **Figure 4.2 b**, the nanograting could not be successfully reproduced in PDMS. More specifically, it was noticed a widespread collapse of subsequent ridges and the presence of many hole-cracks along the grating lines (ridge width = groove width = groove depth = 300 nm, yellow arrows and inset in **Figure 4.2 b**).

Expected failure in replicating patterns with PDMS can be caused by its rather low Young's modulus (≈ 1.5 MPa) [222], which can lead to lateral collapse by merging and buckling dense imprinted structures when the features have lateral dimensions that are generally smaller than ≈ 500 nm and have a high aspect ratio (greater than ≈ 1) [56]. These issues can be avoided with PFPE, which has a higher Young's modulus (≈ 10 MPa) [220]. As depicted in Figure 4.2 c, the PFPE replica shows nanograting profiles over the whole cm^2 area without the imperfections or damages that were found in those made of PDMS. Typically, two forces exerted during the

detachment of the replica from the mold must also be minimized to enhance replication fidelity and extend mold lifetime: friction forces applied to the pattern side-walls and adhesion forces between the two surfaces [223]. Having PFPEs lower surface energy than PDMS (typical values are ≈12.7 mJ/m^2 [220] for PFPE and ≈25 mJ/m^2 for PDMS [224]), these materials can reduce the mentioned friction and adhesion forces, which proves overall better performance with respect to PDMS.

Given the results presented in this study and due to its rigidity and low surface energy, PFPE was selected as the material of choice for intermediate molds for thermal NIL.

4.1.3 *COC Thermal Nanoimprinting via PFPE Intermediate Molds.*

With the final aim to perform thermal NIL, PFPE intermediate molds were employed (instead of the initial ones) to transfer the pattern to COC foils.

COC thermoplastic material is frequently exploited as an optical support for high-resolution microscopy and cell culturing. This polymer is widely used for its high transparency, chemical stability and compatibility with thermal NIL (T_g=134 °C) [216]. COC is flexible, resistant and gas permeable, therefore suitable to be the sealing layer of closed culture environments, where gas exchange has to be preserved (*e.g.* bioreactors or leak-proof culture dishes).

As already mentioned, the use of an intermediate mold can significantly enhance the throughput of the replica process without damaging the initial mold. In order to characterize the fidelity of the complete two-step transfer process, it was used a pattern specifically designed to test the process with extreme geometries.

Two new molds were produced, which are both composed by arrays from isolated ridges and grooves defined by electron beam lithography (**EBL**) on a PMMA film deposited on a silicon substrate.

The first mold, named **Mold100**, has lines with nominal width of 100 nm. The process was further tested by the fabrication of the second mold, named **Mold50**, with a nominal linewidth of 50 nm, with sub-100-nm features.

In both cases, the lines were 1-mm-long, separated by 1 μm, and the line aspect ratio (height/depth over width) was 2 and 1 for **Mold100** and **Mold50**, respectively. As already mentioned, isolated grooves and ridges were chosen to test

the process on topographies that can represent basic building blocks for more complex layouts.

After having fabricated the PFPE intermediate molds as previously described, thermal NIL was performed to transfer the nanostructures on COC foils. The process parameters were previously optimized for this copolymer as follows: $T_{imprint}$ =150 °C, t = 300 s, P = 50 bar, $T_{cool\text{-}down}$ = 80 °C), as depicted in **Figure 4.3**. The characteristic of low surface energy of PFPE also helped in this case, thus facilitating the final detachment of the imprinted plastics.

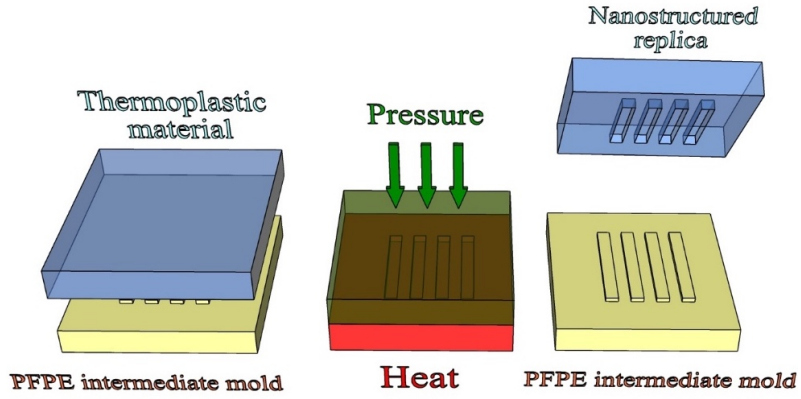

Figure 4.3 **Schematic representation of thermal NIL process made by using the PFPE intermediate mold to reproduce nanometric features on top of a thermoplastic material.** The features used in this study are ridge and grooves fabricated on **Mold100** and **Mold50**; the thermoplastic material in this case is COC.

The process was quality-checked by Atomic Force Microscopy (**AFM**) and by acquiring 3D images of the initial mold, PFPE intermediate mold and the COC replica.

Starting from 5 × 5 μm^2 AFM images, linear profiles were extracted across ridges and grooves to measure their lateral dimension. In particular, the Full Width Half Maximum (**FWHM**) was used as a parameter to quantitatively compare the original nanostructures present on the mold and the ones on the PFPE intermediate and, more importantly, the ones on the COC final replica.

In case of **Mold100**, mold ridges (**M-R**) and mold grooves (**M-G**) had FWHM values of 122 ± 4 nm and 124 ± 2 nm, respectively. COC Ridges (**C-R**) and Grooves (**C-G**) showed equivalent width values (124 ± 2 nm for C-R, 122 ± 3 nm for C-G) (Figure 3a), which demonstrates that the process can successfully transfer isolated

features with a lateral dimension of the order of 100 nm and aspect ratio = 2, as shown in **Figure 4.4**.

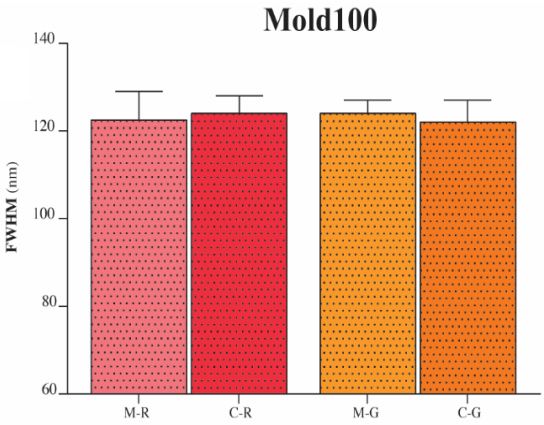

Figure 4.4 **Full Width Half Maximum measurements of Mold100 ridges (M-R) and grooves (M-G), and respective COC replica ridges (C-R) and grooves (C-G).** The replica process was demonstrated to be successful, replicating COC ridges and grooves with equivalent FWHM values. Data are mean ± SD.

3D AFM reconstructions in **Figure 4.5** show a larger view of the topographies, which confirms the satisfactory compliance of each transfer step to the previous and highlights the consistent profiles of the original mold and COC replica. Owing to the possibility to fabricate more copies of the same initial mold and to the fact that a single PFPE intermediate mold can sustain tents of thermal imprint cycles without cracking or affecting the final feature resolution, the entire process yield is considerably increased.

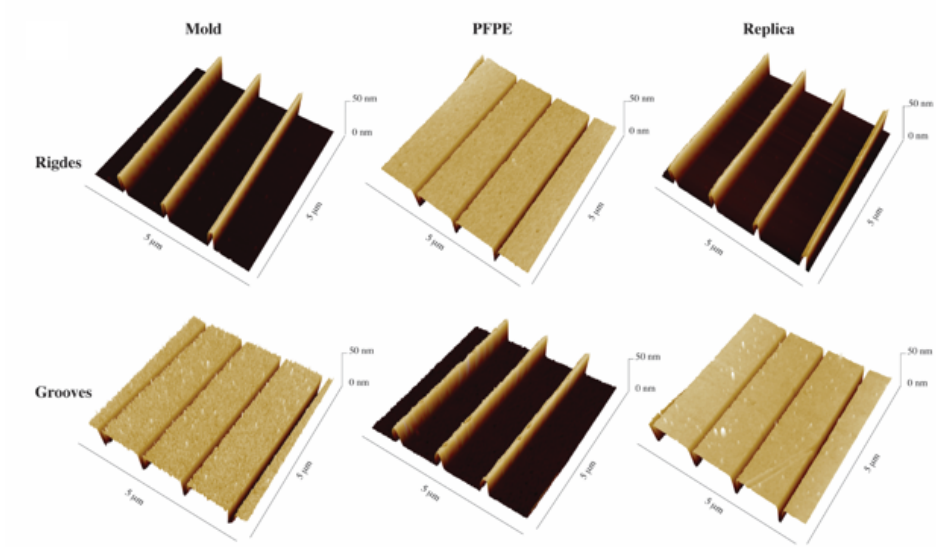

Figure 4.5 **Representative 3D AFM images for ridges and grooves of the Mold100, PFPE intermediate mold and COC final replica.** The yield of total transfer process is enhanced, without affecting the final resolution of the single feature, because a single PFPE intermediate mold can sustain tents of imprint cycles without cracking.

Mold50 was then tested in order to find the process resolution limit. In this case, it was measured a FWHM of 52 ± 1 nm for M-R and 48 ± 4 nm for M-G, while an enlargement was measured for the COC replica. More specifically, the FWHM was 80 ± 2 nm for C-R and 63 ± 3 nm for C-G (**Figure 4.6**). Sub-100 nm topographies were, therefore, transferred to COC. This experiment also suggests that lines of lateral dimension of ≈ 80 nm (for ridges) and ≈ 60 nm (for grooves) and with an aspect ratio = 1 can be considered as the minimum feature size allowed by our two-step replica process.

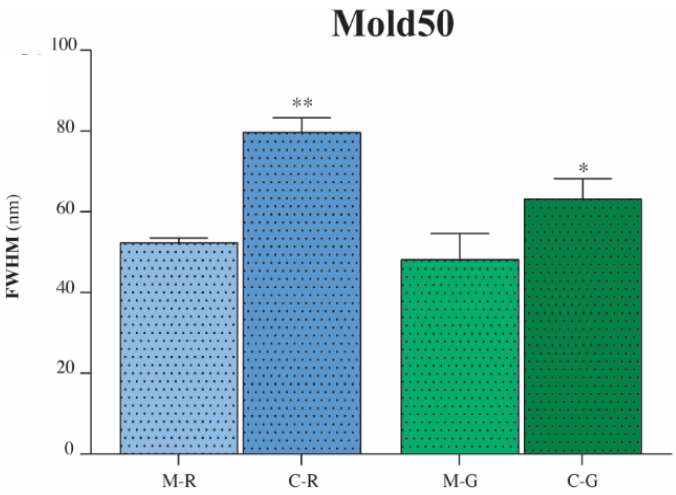

Figure 4.6 **FWHM of Mold50 ridges (M-R) and grooves (M-G), and respective COC replica ridges (C-R) and grooves (C-G)**. The two-step replica process here developed doesn't allow pattern transfer of lines of lateral dimension of 50nm from the **Mold50** to the COC. In fact, ridges of lateral dimension of ≈ 80 nm and grooves of ≈ 60 nm with an aspect ratio = 1 can be considered as the minimum feature size allowed by the use of PFPE interm. Data are mean ±SD, */**P<0.05/0.01, unpaired t-test.

4.1.4 *Conclusions.*

In this chapter I have introduced and characterized an innovative two-step thermal NIL process, based on the use of intermediate molds made of PFPE to replicate sub-100 nm features from a silicon mold to a final thermoplastic material (COC).

After a careful evaluation, I found that isolated lines of lateral dimension of ≈ 80 nm (in case of ridges) and ≈ 60 nm (in case of grooves), and with aspect ratio = 1, can be considered at the moment as the minimum feature size that can be replicated from an initial mold to the thermoplastics by the use of the new method to employ PFPE in thermal NIL.

Given the results and the possibility to increase the rigidity of PFPEs by adding chemical groups or tailoring the PFPE/crosslinker mix, I believe that it would be possible to obtain sub-50 nm resolution and beyond.

4.2 Materials and methods.

Mold fabrication.

Mold100 and Mold50 were obtained in PMMA by EBL starting from commercial p-doped silicon wafers (SYLTRONIX, France). Briefly, each mold was initially processed by EBL to generate arrays of ridges and grooves of 100 mm^2 area into a 50-nm-thick PMMA film. PMMA was spun over a 5 nm-thick titanium layer previously deposited on the silicon wafer by thermal evaporation. After cleaning with nitrogen flow, the molds were systematically characterized by optical microscopy and atomic-force microscopy.

The 600-nm-period grating mold was fabricated by laser interference lithography (LIL). SPR220 (Microposit (Shipley European Limited, UK) was spun onto a silicon wafer with a spin speed of 4000 rpm for 30 s. The sample was exposed to a 50 mW helium cadmium (HeCd) laser, emitting a TEM_{00} single mode at a 325 nm light source with a beam incidence angle of 165.7° and an exposure dose of 77 mJ/cm. Resist developing was performed by immersing the sample in a MF319/Milli-Q water (10:1) solution for 15 s [225].

PDMS intermediate mold fabrication.

The precursor PDMS polymer (SYLGARD 184, USA) was mixed with its curing agent at a ratio of 10:1 and poured onto the nanostructured mold. The uncured replica was then left resting for 10 min to reduce surface inhomogeneities, then it was baked in an oven for 2 hours at 80 °C. After thermal curing, the replica was gently removed from the master using scalpel and tweezers.

PFPE intermediate mold fabrication.

In order to fabricate the intermediate molds, PFPE resin (FLUOROLINK® MD 700, Solvay Specialty Polymers, Bollate, Italy) was mixed with 3% w/w photoinitiator Darocure 1173 ($C_{10}H_{12}O_2$, 405655 Sigma Aldrich), poured on top of the PMMA surfaces, and crosslinked by UV-light (365 nm, 25 $mW \cdot cm^{-2}$). The exposure was performed in two steps: briefly, the samples were kept for 180 s in nitrogen atmosphere, then for 60 s in air. After curing, the PFPE films were easily peeled off and cleaned with nitrogen flow.

COC nanoimprinting.

COC foils (thickness 140 μm, Microfluidic ChipShop GmbH, Jena, Germany) were imprinted using an Obducat Nanoimprint 24 system (Obducat, Lund, Sweden) with the PFPE intermediate molds. After cleaning with 2-propanol, the COC substrates were placed on top of the molds and softened by raising the temperature up to 150 °C. A pressure of 50 bar was then applied for 300 s before cooling down to 70 °C, i.e. below the glass transition temperature of the copolymer (T_g = 134 °C). Finally, the pressure was released and the mold was detached from the imprinted COC with a scalpel.

PET replicas.

PET foils (thickness: 250 μm, Coexpan, Montonate, Italy) were thermally imprinted in two steps: after 2-propanol cleaning, flat PET foils were placed on top of COC replicas, then warmed up at 75 °C. A pressure of 20 bar was then applied for 300 s, then the system was brought below the PET glass transition temperature (T_g = 75 °C), down to 50 °C and the pressure was finally released. A nitrogen flow was applied between the PET replica and the correspondent COC mold to easily detach one from the other.

Scanning Electron Microscopy.

Molds, intermediate molds and final replicas were analyzed with a LEO 1525 field emission scanning electron microscope. In order to enhance the topography of substrate surfaces, image acquisition was carried out by using an Everheart-Thornley detector.

Contact Angle Measurements.

Substrate wettability was evaluated by contact angle measurements acquired with a CAM 200 instrument (KSV Instruments, Helsinki, Finland). A deionized water drop was deposited on top of each substrate through a micro-syringe. All these measurements were performed in air at room temperature. Data are reported as mean ± SD.

Atomic Force Microscopy.

Sample topographies were characterized by an atomic force microscope (Veeco Innova Scanning Probe Microscope, Veeco Instruments Inc., Santa Barbara, CA, USA), operating in tapping mode. The scan frequency was set at 0.977 Hz, the scanning areas were 5 ×5 μm^2. At least 3 areas were analyzed per sample (512 point/line each). At least three PFPE intermediate mold and COC replicas were imaged for each topography type. A silicon nitride tip with a nominal spring constant in the range of 0.2-0.8 N/m and a resonant frequency of 45–95 kHz was used. All the measurements were performed in air at room temperature and raw scan data were leveled by surface subtraction to remove possible sample tilts. Data were analyzed by the Gwiddion software (Gwiddion 2.47 version, "*Profile*" tool), and reported as mean ± SD. Full Width Half Maximum values were measured from the AFM profiles by the "Analysis: Peaks and Baseline: Multiple Peak Fit- Gaussian fit" tool of the software Origin (https://www.originlab.com, version 9.0).

Statistical analysis.

Data are reported as average values ± the standard deviation (mean ± SD). Data were statistically analyzed by the GraphPad PRISM 6.1 program (GraphPad Software, San Diego, CA, USA). Student' *t*-test (unpaired) analysis was used to compare distributions; the mean values obtained in each repeated experiment were assumed to be normally distributed about the true mean. Statistical significance refers to results where $P < 0.05$.

5 Interaction between cells and nanotopographies.

Artificial scaffolds with controlled micro/nano-topographies have proved to be extremely effective to the study of the cell response mechanisms to external stimuli, with obvious advantages for tissue engineering and regeneration applications. Notably, in the field of neuroscience it has been demonstrated that nanostructured surfaces can modulate neuronal and glial cell differentiation, polarity migration, neurite orientation and even stem cell fate.

*In this chapter I will introduce the use of perfluoropolyether (**PFPE**) intermediate molds to replicate a new type of anisotropic nanostructures, named nanoripples* [226]. *Moreover, I will show their effects on Schwann Cells (**SCs**), in view of their possible use for nerve-repair applications.*

*In the case of PC12, I will demonstrate that loss of neurite guidance occurs in nanogratings (**NG**) with periodicity below 400nm, correlating with a loss of FA lateral constriction and spatial organization. I found that YAP/TAZ intracellular localization is modulated by the presence of **NGs**, but it is not sensitive to their periodicity.*

5.1 Multi-scaled Structured Germanium Nanoripples as Templates for Bioactive Surfaces.

Ion beam bombardment at a few tens of keV energy can lead to the spontaneous formation of periodic ripples or dot nanopatterns on the surface of semiconductors, metals and insulators [227]. As a single-step method to fabricate regular patterns over large surface areas, it can potentially overcome the limits of conventional lithographic methods, mainly related to size reduction and high-throughput production capability [228]; hence, the nano-pattern formation has been investigated for different applications, such as electronic-[229] and bio-devices [230].

The possibility of a multiscale structuring of a germanium (**Ge**) surface by ion implantation, aimed at merging into a single step self-organized ripple patterns of a few hundred nanometer periods, and sponge-like structures of about ten nanometer size that lie especially on the ripple crests, is new and envisages its importance in various applications of advanced functional surfaces. In this work,

this kind of multi-scale topology was obtained by bombarding a Ge surface with Au^+ ions.

In order to further help the rational engineering of scaffolds for, but not limited to, the regeneration of the nervous system, smaller spatial scales of ECM topography interaction is one of the possibilities to be investigated.

To this aim, the self-organized periodic ripple nanopatterns with the superimposed nanowired structure obtained by ion implantation have been used in a new two-step pattern-transfer process, producing a final replica onto a COC substrate. This result allows the investigation of the mechanotransduction from artificial regular geometries characterized by a periodicity of about 300 nm after a subsequent thermal NIL cycle, after transferring nanoripples to PET foils.

5.1.1 *Germanium sample characterization.*

The effects on the topography of the increase of the irradiating ion dose, with constant energy and incidence angle of 60°, are shown in **Figure 5.1**, where the surfaces of the sample irradiated with the lowest ion dose (Ripple Low-Dose $\mathbf{R}_{LD}$, 1 x 10^{17} ions/cm^2) and of that irradiated with the highest dose (Ripple High-Dose $\mathbf{R}_{HD}$, 4 x 10^{17} ions/cm^2) are shown.

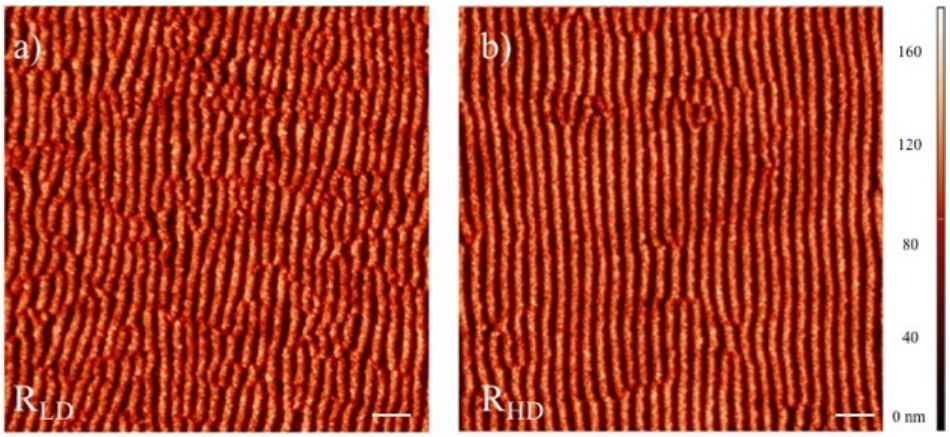

Figure 5.1 **AFM 2D topographic images obtained from nanoripple samples** a) $\mathbf{R}_{LD}$, sample irradiated with the lowest ion dose and b) $\mathbf{R}_{HD}$, the one irradiated with the highest dose of Au^+ ions bombarding Ge surface. Scale bar: 1 μm.

Moreover, the corresponding one-dimensional height-height autocorrelation functions (**ACFs**) indicate that the long-range regularity sensibly increases with the ion dose. For $\mathbf{R}_{HD}$, the fundamental ripple spacing (wavelength λ), given by the first

peak position of the ACF of is λ=291.0 nm 95% c.i. [289.0, 292.0]. Consistently, for $\mathbf{R}_{LD}$, the fundamental ripple spacing is λ= 331.0 nm 95% c.i. [330.0,333.0] nm, higher than the value measured for $\mathbf{R}_{HD}$.

To estimate the ripple amplitude, described as the mean peak-to-valley excursion, the mean roughness depth R_z was calculated. For sample $\mathbf{R}_{HD}$, the result is 87.0 nm ± 13.0 nm, comparable to $\mathbf{R}_{LD}$ excursion, whose value is 89.0 nm ± 15.0.

The long-range correlation of the rippled pattern is confirmed by the SEM image taken at the lowest magnification (**Figure 5.2**). A high-magnification image of the patterns is reported in **Figure 5.2 b-inset**, which shows the presence of the multiscale structure: the ripples are not compact, rather they show a nanowired structure along the ridges. The same multi-scale structure was also visible for the $\mathbf{R}_{LD}$ sample (**Figure 5.2 a-inset**) [226].

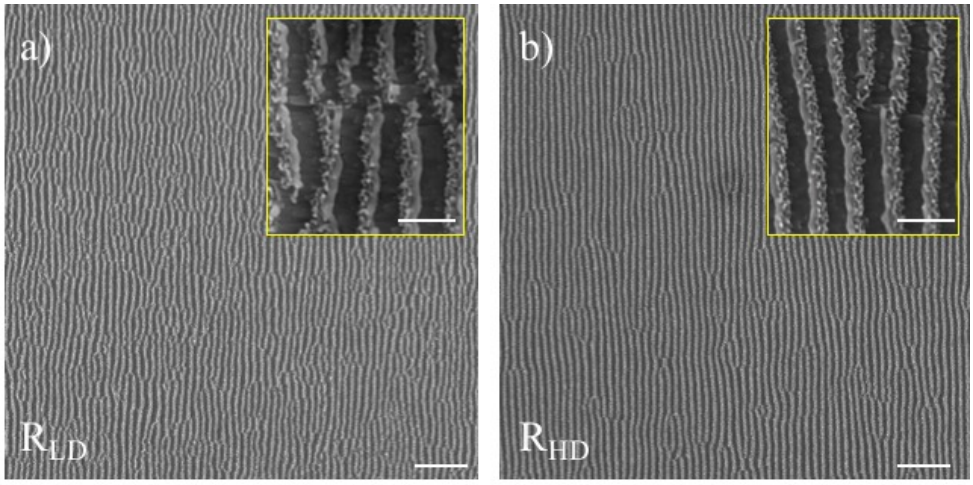

Figure 5.2 **SEM topographic images obtained from nanoripple Ge molds** a) $\mathbf{R}_{LD}$ and b) $\mathbf{R}_{HD}$ (Scale bar: 2 μm) and relative insets (scale bar: 500 nm). The multiscale structure is clearly visible, for both the different type of nanoripples.

5.1.2 *Fabrication and characterization of PET rippled surfaces*

Rippled multiscale topographies were fabricated by an innovative three steps fabrication process onto PET surfaces (**Figure 5.3**) starting from the two Ge molds, $\mathbf{R}_{LD}$ and $\mathbf{R}_{HD}$. In fact, PET is a thermoplastic polymer, very stable in water [231], [232], well suitable for high-resolution hot-embossing [233]. It is currently used in many biological applications thanks to its properties such as biocompatibility, high light

transmittance, low coefficient of thermal expansion, stable mechanical properties, good chemical resistance and durability [234]. Owing to its mechanical strength, easy manipulation and bio-stability, PET is also widely used for cell culture substrates (as Thermanox® or Mylar®), surgical suture material, vascular grafts (*e.g.* Dacron®) and ligament prosthesis [235].

A mixture of PFPE resin and a photo-initiator was poured on Ge top of the molds and, following UV-light crosslinking, two PFPE intermediate molds were obtained, one for each type of nano-rippled mold (**Figure 5.3 a**). After PFPE substrates fabrication, we decided to produce a second intermediate mold to be used for the final PET embossing.

To this end, the PFPE surfaces were thermally embossed onto COC foils, obtaining a second set of intermediate molds (**Figure 5.3 b**). As already stated, since the glass transition temperature of COC (T_g=134 °C) is much higher than that of PET (T_g= 75 °C), the PET replicas were produced by the use of these substrates as molds (**Figure 5.3 c**) by exploiting the low-temperature hot-embossing process specifically developed for PET.

The final PET R_{LD} and R_{HD} surfaces displayed a high degree of conformity upon the three fabrication steps, as shown by the AFM characterization reported in **Figure 5.3**. The uniformity of the patterns was preserved for the whole 1 cm^2 area, with a ripple periodicity of 270 ± 40 and 290 ± 30 nm for the R_{LD} and R_{HD} structures, respectively.

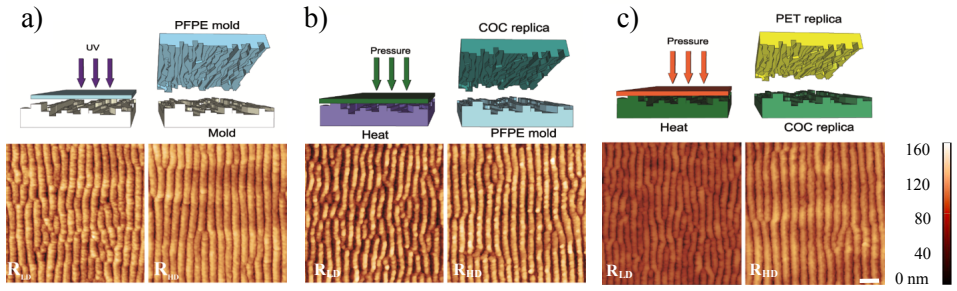

Figure 5.3 **Schematic description of the fabrication process and the correspondent AFM images**. a) PFPE intermediate molds obtained by UV-Crosslink process for both R_{LD} and R_{HD} periodic nano-rippled features; b) Thermal NIL process with PFPE intermediate mold to obtain COC replicas; c) PET nano-rippled replicas obtained by thermal NIL. Scale bar: 1 μm.

Furthermore, the directionality of the nano-rippled PET surfaces was evaluated by an FFT analysis of 2×2 μm^2 AFM images (see Materials and Methods for details).

Indeed, the dispersion (**σ**) parameter for these substrates decreased to $\sigma R_{LD} = 7.8 \pm 2.4°$ and $\sigma R_{HD} = 4.9 \pm 2.7°$, while $\sigma Flat = 32.9 \pm 9.1°$. Particularly, σR_{HD} was significantly reduced with respect to σR_{LD}: this difference shows that R_{HD} is more directional than R_{LD} (**Figure 5.4**, */**** P<0.05/<0.001, One-Way ANOVA Kruskal-Wallis test, #P<0.05, Mann-Whitney test).

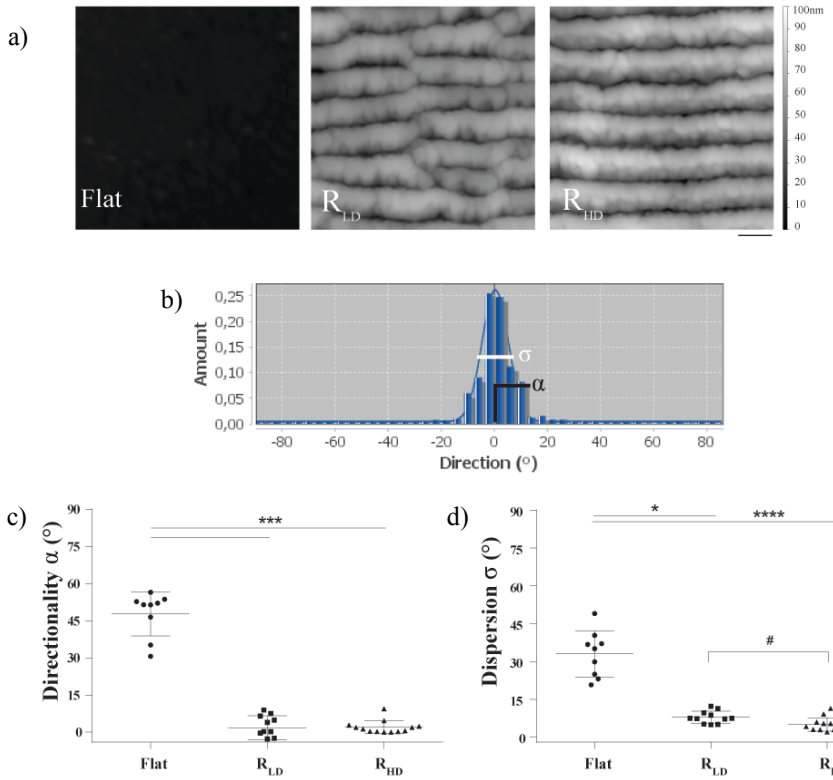

Figure 5.4 **Nano-ripples directionality analysis**. a) AFM images of Flat, R_{LD} and R_{HD} periodic nano-rippled PET surfaces; scale bar = 300 nm. b) Representative image of fast Fourier transform (FFT) of R_{HD} topography. c) Directionality (α) and d) dispersion (σ) parameters calculated for the different substrates: */***/**** *P*<0.05/0.001/0.0001, One-Way ANOVA Kruskal-Wallis test; # *P*<0.05 R_{LD} vs. R_{HD}, Mann-Whitney test. Data= mean ± SD.

The surface roughness was then evaluated by measuring the average roughness (**Ra**), the maximum vertical distance (**Rmax**) and the Surface Area Difference (**SAD**) parameters (see Materials and Methods for parameter definition) along different directions (starting from 0° with incremental intervals of 22.5° with respect to the main pattern orientation, as shown in **Figure 5.5-inset**) on 3×3 μm^2 AFM images.

Nano-rippled PET surfaces resulted rougher than the Flat control: the presence of nano-ripples induced an increase of Ra (average Ra values: Flat= 1.0

nm, R_{LD} =7.2 nm and R_{HD} =14.1 nm) ($P < 0.0001$, Tukey's test; **Figure 5.5 b**), SAD (average values: Flat= 0.4%, RLD= 6% and RHD=7%) ($P < 0.01$ / 0.001, Tukey's test; **Figure 5.5 c**) and Rmax (average Rmax values: Flat= 8.5 nm, R_{LD}= 36 nm, R_{HD}= 63 nm; §§§§$P < 0.0001$, Tukey's test; **Figure 5.5 d**) for both R_{LD} and R_{HD}. It is worth noting that R_{HD} was significantly rougher than R_{LD}.

The positive effect of surface roughness on neural cell attachment and growth has been previously investigated in literature, though not on hierarchical nano-ripples.

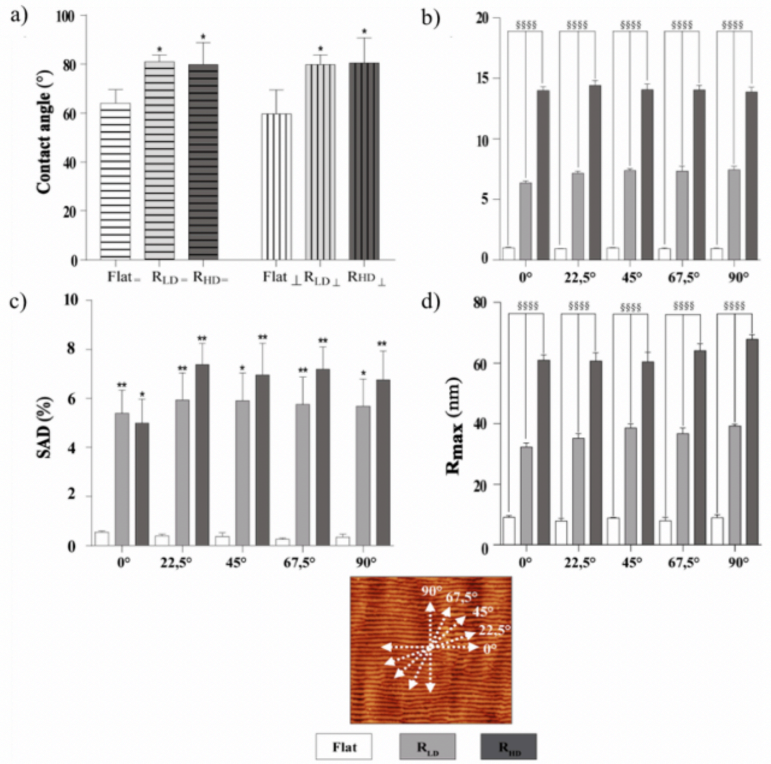

Figure 5.5 **Surface characterization of the R_{LD} and R_{HD} PET periodic nano-rippled substrates.** a) Contact angle measurement, along the parallel (=) and perpendicular (⊥) direction with respect to the main direction of the pattern; * $P < 0.05$, One-way ANOVA, Dunnett's test *vs.* Flat. b) Average roughness Ra (nm); c) Surface Area Difference (SAD) (%); d) Rmax roughness. The roughness parameters (b-d) were calculated from three 3×3 μm^2 different areas for each nano-rippled and Flat replicas along five different directions, starting from 0° to 90° with respect to the main direction of the pattern. Data= mean ± SD; c) */** $P < 0.05$ / 0.01, One-way ANOVA, Dunnett's test *vs.* Flat; b-d) §§§§ $P < 0.0001$, One-way ANOVA, Tukey's multiple comparisons test.

The roughness values of R_{LD} and R_{HD} (around 10-20 nm) falls in the *optimum* roughness range, as shown in **Figure 5.5 b**. This so-called *moderate roughness* regime [236], characterized by Ra roughness values within the nanometric scale 10-45 nm, has influenced also Schwann cells (**SC**) behavior, enhancing their adhesion and growth. For the sake of example, a surface average roughness of 23 nm enhanced the SC growth and spreading on collagen-type-IV-containing Matrigel electrospinned fibers [237]. Not surprisingly these roughness values, similar to that obtained for the R_{HD} (Ra= 14 nm), mimic the features of the *lamina densa* pits (20 nm in depth) of mouse sciatic nerve [238].

In the case of our substrates, the sponge-like structure present on nano-ripples [60] is partly responsible for the overall surface roughness, possibly contributing to the observed enhancement of cell adhesion. Therefore, those data found support in the literature, where roughness in the nanoscale range is considered as one of the main factors that influences neural cells, and in particular SC adhesion and proliferation.

Since wettability importantly affects cell adhesion, in order to further characterize these surfaces, water contact angle measurements were performed (**Figure 5.5 a**) along both the parallel and perpendicular direction with respect to the main rippled pattern orientation. Both the R_{LD} and R_{HD} resulted more hydrophobic than the Flat control (* $P < 0.05$, Dunnett's test), for both directions. This result finds confirmation in the Wenzel model, which states that roughness affects the contact angle hysteresis and that, if the surface is chemically hydrophobic, it will become even more hydrophobic when surface roughness is added [239].

In general, hydrophilic surfaces display better affinity for cells but lower adsorption for proteins than the hydrophobic ones [240]. In fact, hydrophilic materials promote a weak and reversible adsorption of proteins, whereas hydrophobic ones induce an irreversible adsorption of high-weight proteins [241]. However, this last behavior can also lead to the opposite effect on cell adhesion. According to this scenario, the measured SC enhanced adhesion might also have been favored by the nano-ripple increased hydrophobicity.

Overall, it was developed a novel three-step thermal embossing process to produce biocompatible and transparent thermoplastic substrates having directional, periodic nano-rippled structures on their surfaces. These PET nano-

ripples have a typical spatial period of 270 ± 40 nm for R_{LD} and 290 ± 30 nm for R_{HD}, respectively and both topographies exhibited an increased hydrophobicity and roughness with respect to Flat controls.

5.1.3 *Cell spreading and viability tests.*

Given the moderate wettability of R_{LD} and R_{HD}, the PET substrates were coated with poly-D-lysine and laminin (100 and 50 $\mu g \times mL^{-1}$, respectively) to allow good SCs adhesion and proliferation.

In order to study how SCs attach and spread on these substrates, cell adhesion was quantified after three hours from seeding. To this end, bright field microscopy images were acquired and the percentage of cells that underwent full adhesion and spreading (**Figure 5.6 a**, *first row*) was measured.

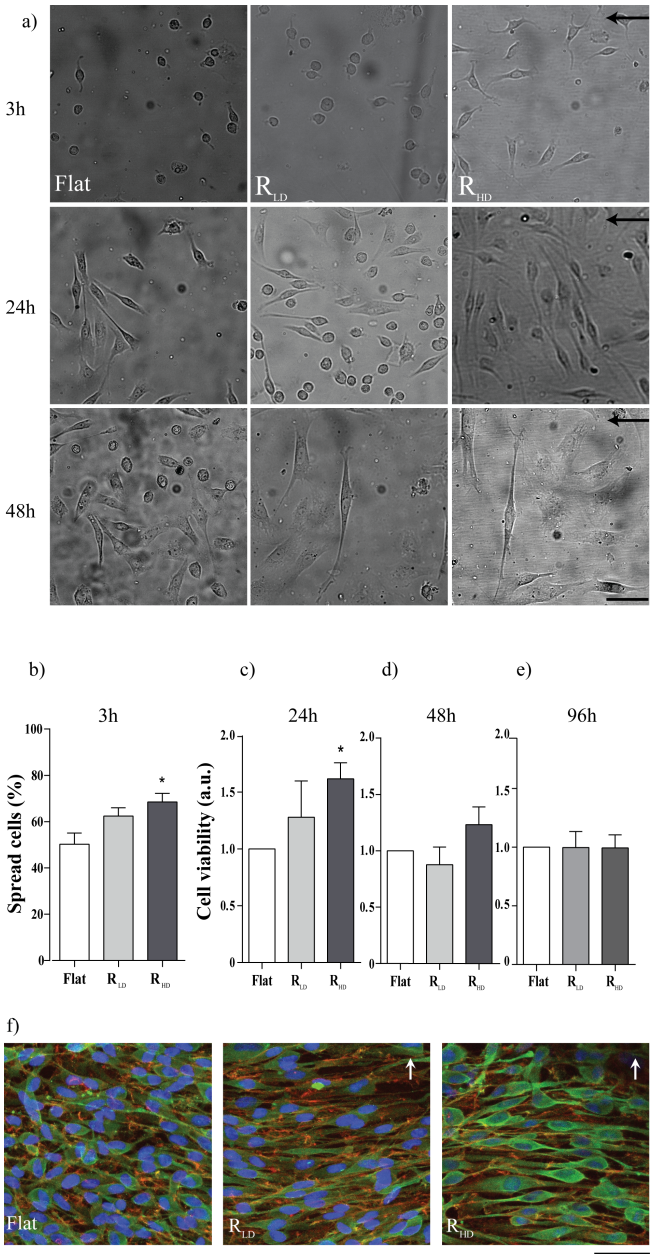

Figure 5.6 **Schwann cells spreading and viability tests.** a) Bright field images of Schwann cells cultured on Flat, R_{LD} and R_{HD} periodic nano-rippled PET replicas after 3h, 24h, and 48h from seeding. Scale bar: 50μm. Arrows indicate the nano-ripple direction b) Percentage of spread cells at 3h. c-e) SC cell viability at 24h,48h and 96h after seeding. Data= mean ± SEM, $n \geq 3$; * $P < 0.05$, One-way ANOVA, Dunnett's test vs. Flat. f) Representative confocal images of SCs cultured for 7 days on Flat, R_{LD}, and R_{HD}, and immuno-stained for S100 (green), actin (red) and nuclei (blue). SCs proliferated and reached confluence on nano-ripples and flat surfaces. Scale bar: 50 μm; white arrows: ripple direction.

The qualitative analysis of these images confirms the cytocompatibility of PET surfaces, being the cells well adhered and showing their natural spindle-like shape on all the substrates. Remarkably, cell spreading was promoted on nano-ripples, and this effect was particularly pronounced on R_{HD} ($P < 0.05$ *vs.* Flat, Dunnett's test; **Figure 5.6 b**).

With the aim to test how SCs grow on the substrates, SCs were incubated up to 96 h and their amount was measured by a cell proliferation test. As shown by the microscopy images reported in **Figure 5.6 a**, SCs were viable and proliferated, showing their typical morphology. After 24 h, the amount of SCs was increased on the rippled patterns, in particular on R_{HD} ($P < 0.05$, R_{HD} *vs.* Flat, Dunnett's test; **Figure 5.6 c**). After 48 hours, SC proliferation was similar among all the substrates (**Figure 5.6 d**); after 96 hours, SCs reached high-density and their viability remained similar among all the substrates (**Figure 5.6 e**). Finally, SCs were cultured up to one week on all the different substrates, showing to maintain their typical spindle-shape, healthy morphology, and to reach complete confluence (**Figure 5.6 f**).

All together these data demonstrate that nano-rippled PET substrates are suitable for SCs, determining an increased short-term cell adhesion (3 h) and viability (24 h), in particular on R_{HD}; at longer term (48 and 96 h and 1 week), SC proliferation rate and viability were comparable to that of the control flat condition.

5.1.4 *Cell morphological analysis.*

In order to quantitatively investigate how the SC morphology was affected by the nano-ripples, after 48 h of culture the cells were immunostained for **S100** (SCs marker) and **DAPI** (nuclear marker) and a set of cellular morphological parameters (area, elongation and orientation; see Materials and Methods of this chapter for definitions) was evaluated from fluorescence microscopy images (**Figure 5.7 a**).

R_{LD} and R_{HD} did not determine a change in SC area with respect to those cultured on Flat surfaces (**Figure 5.7 b**). Cell elongation (reported as aspect ratio; **Figure 5.7 c**), instead, resulted markedly enhanced on R_{HD} compared to the flat condition ($P < 0.01$ vs. Flat, Dunnett's test). Conversely, SCs elongation on R_{LD} showed intermediate values, with not so pronounced SCspindle-shape.

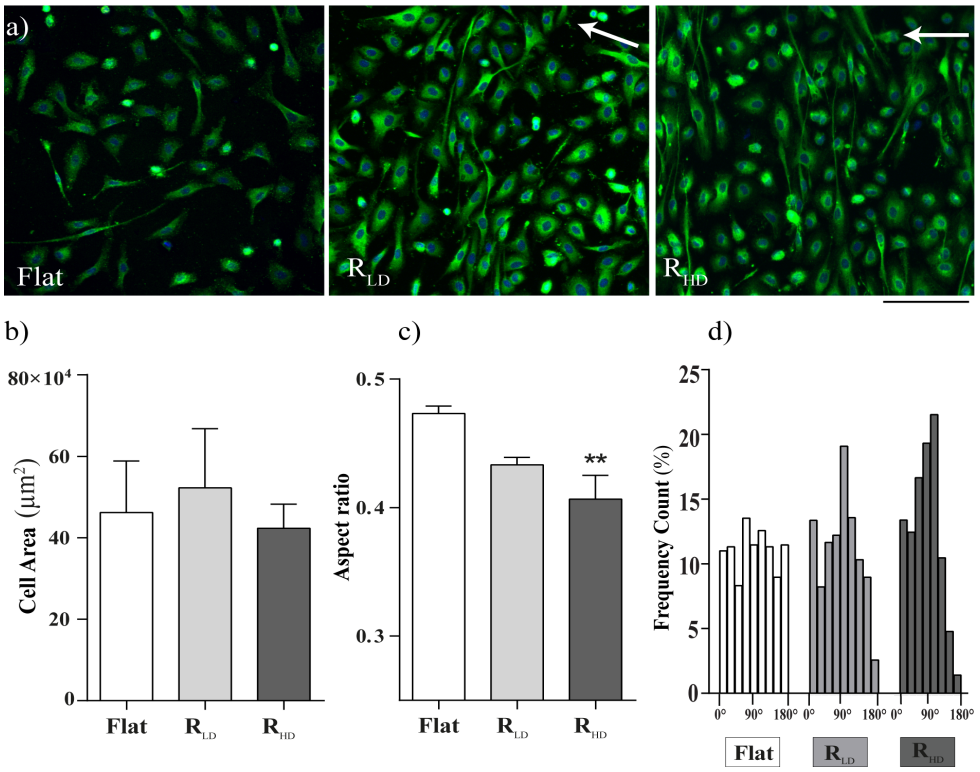

Figure 5.7 **Schwann cells morphological analysis.** a) Confocal microscopy images of Schwann cells on Flat, R_{LD} and R_{HD} nano-rippled PET stained for S100 (green) and nuclei (blue). Scale bar: 100μm. Arrows indicate the nano-ripple direction. b-c) SC morphological characterization: cell area (b) and aspect ratio (c) for the different substrates. d) Cell angular distribution (0° is the nano-ripple direction) for the different patterns. Data= mean ± SEM, n=3; fig. 4c: ** $P < 0.01$, One-way ANOVA, Dunnett's test vs. Flat.

It was noticed that SCs showed the tendency to arrange along the perpendicular direction with respect to the ripple pattern lines (**Figure 5.7 a**). In order to characterize this phenomenon, the percentage of SCs aligned along different angles (between 0 and 180°, in 10° steps) was quantified with respect to the pattern direction (= 0°).

This measure confirmed our visual observations: both rippled surfaces led to a clear asymmetry of the cellular angular distribution, with a pronounced peak at 90° (**Figure 5.7 d**). Notably, in the case of R_{HD}, more than the 50% of SCs disposed perpendicularly (*i.e.* with an alignment angle between 60° and 120°) to the pattern lines (marked with a white arrow in **Figure 5.7 a**). Perpendicular orientation was also observed after seven days of culture, as shown in **Figure 5.7 f**.

All together, these data demonstrate that SCs actively interact with nano-rippled topographies, and polarize in a perpendicular direction with respect to the pattern lines. This effect become more evident on R_{HD}, the rougher substrate.
Despite the vast majority of examples in literature, not all types of cells exhibited parallel alignment to directional topographies. In different experiments, SH-SY5Y human neuroblastoma cell line [242] and hippocampal neurons [243] grew mainly parallel to nano- and micro-grooved surfaces (with period between 0.5 and few μm, and sub-micrometer groove depth). Conversely, perpendicular alignment was shown for rat hippocampal neurites on shallow grooved substrates (1 μm wide grooves with depths ranging from 14 nm to 1.1 μm) [106] and for central nervous system (**CNS**) neuroblasts on quartz micro-grooves (1μm-groove-width, depths between 300 and 800 nm) [244].

To the best of our knowledge, no reports were made of PNS neurons perpendicularly aligned to directional topographies before our study with hierarchical nanoripples.

In order to better analyze the interaction mechanism between the nano-ripples and SCs, SC filopodia and lamellipodia by were imaged SEM (**Figure 5.8**).

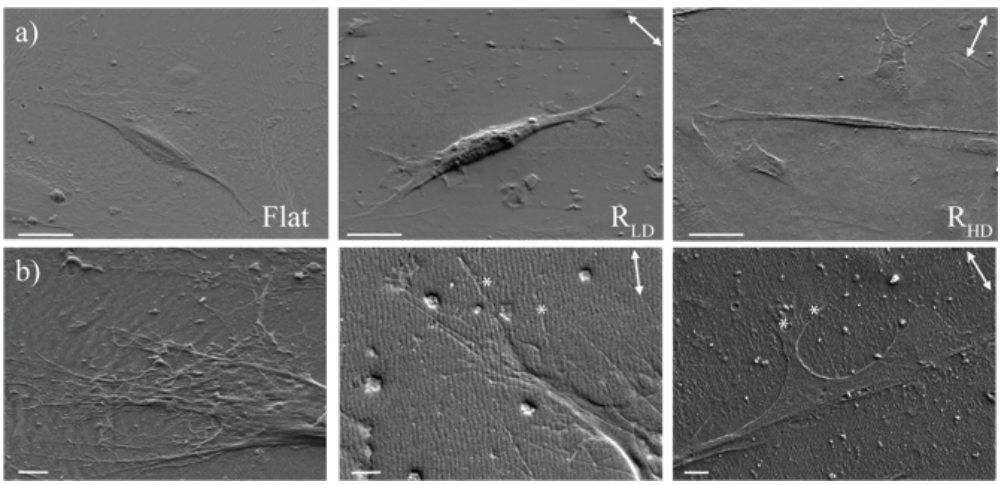

Figure 5.8 **Representative Scanning Electron Microscopy images of SCs on Flat, R_{LD} and R_{HD}** a) Low-magnification images showing whole cells. Scale bar: 10μm; b) High-magnification images showing Filopodia and lamellipodia orientation; white stars mark filopodia parallel to the ripples. Scale bar: 2μm.

Unexpectedly, in the case of SCs orientated perpendicularly to the pattern lines, filopodia followed the ripples on both R_{LD} and R_{HD}; in case of Flat surfaces, no

preferred spatial orientation was found for filopodia, which explored their surrounding at 360° with random orientation (**Figure 5.8 b**).

The only experiment studying filopodia alignment on nano-ripple substrates is that by Pedraz et al. [245], where neural stem cells were cultured on nano-rippled glass surfaces and emitted filopodia mainly in parallel direction, consistently with our observation.

No body alignment was instead reported. Authors explained that the contact area between filopodia and the substrate was in this way maximized, thus leading to optimal adhesion.

It is actually not straightforward to make a causative hypothesis between the orientation of filopodia and cell bodies, since chemical cues might also contribute to this contrasting behavior other than the physical characteristic of the substrate, as the Prof. Murphy's group demonstrated for epithelial cells and micro-grooved surfaces [246].

They indeed showed that perpendicular and aligned cell orientations, and filopodia sensing are determined by the cooperation of different chemical (*e.g.* culture medium) and physical (*e.g.* substrate topography) stimuli, and are cell-kind dependent.

While some studies, as the one just mentioned, searched for differential molecular cell signaling mechanisms to explain contact guidance, Albuschies's group recent work indicates that contact guidance might be a filopodia traction force-mediated peeling process. The cell is guided only in the direction where the geometrical constraints allow the filopodial contacts to mature by forming a maximal number of adhesive bonds [247].

Filopodia are excellent devices to sense the line substrate since they are rigid, rod-like structures that cannot bend and adhere to the grooves of the pattern, and have similar size features than our pattern periodicity (filopodia width = 200–500 nm [248]). They might thus discern if they are aligned or not on the pattern by evaluating the contact area between the filopodia and the pattern. Non-aligned filopodia stochastically scan the line substrate through a process that occurs on a timescale of a couple of minutes, and consists of cycles of protrusion–retraction events that are coupled with a back and forth lateral motion. This is repeated until a filopodium aligns on the pattern ridge which subsequently leads to the assembly

of a robust F-actin network and an extensive contact zone with the pattern.This then enables to switch off the dynamic unstable behavior observed in non-aligned filopodia, allowing to filopodium stabilization for hours, and ultimately leading to steady neurite outgrowth. The two distinct filopodial behaviors most likely depend on different levels of coupling between the substrate and the cytoskeleton as proposed in the *molecular clutch model* [249].

The picture is indeed very complicated, and a deep understanding of the molecular pathways determining the switching between the two behaviors is still very debated by the research community.

5.1.5 *Actin cytoskeleton organization analysis*

Furthermore, it was examined how the nanoripples can influence SC cytoskeleton organization by actin fiber staining and confocal fluorescence microscopy.
SCs displayed cortical actin and well-developed actin stress fibers (**Figure 5.9 a**). The actin high-resolution fluorescence images confirmed the high degree of perpendicular SC polarization induced by both the rippled topographies.

By comparing the actin content in cells with different alignment, it was found that the presence of the nanoripples might have induced actin enrichment in cells oriented perpendicularly with respect to those that showed parallel alignment. Since actin cooperates in determining cell contractility and adhesion maturation, this cytoskeleton configuration probably led to an angle-dependent cell selection with the depletion of the population of cells expressing less actin.

In order to understand if the actin cytoskeleton was involved in mediating perpendicular SC orientation, the average intensity of the fluorescent actin was quantified in whole-cell bodies and in the cell protrusion tips.
In particular, two categories of cells were selected: those with *perpendicular orientation* (*i.e.* with alignment angle $\geq 60°$ vs. pattern direction) and those with *parallel orientation* (*i.e.* with alignment angle $\leq 30°$ vs. pattern direction.

Figure 5.9 b shows that that the presence of the nanoripples might induce actin enrichment in cells aligned perpendicularly with respect to those that show parallel alignment.

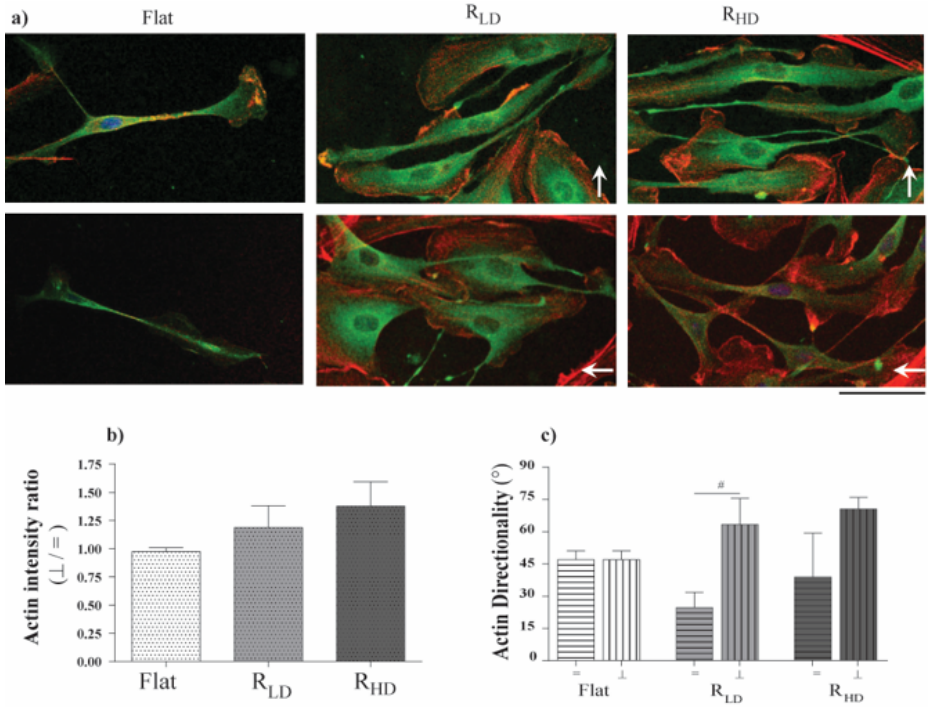

Figure 5.9 **Actin cytoskeleton organization analysis**. Representative confocal images of SCs on Flat, R_{LD} and R_{HD} and immuno-stained for S100 (green, specific SC marker), actin fibers (red) and nuclei (blue); images in the first row show the perpendicularly-oriented SCs, while in the second row the SCs with parallel orientation (white arrows mark ripple direction). Scale bar: 20μm. b) Intensity ratio between the actin signal of perpendicularly-oriented cells and that of cells with parallel alignment, for each topography. c) FFT actin directionality (°) for perpendicularly-oriented SCs (⊥; i.e. with alignment angle ≥ 60° vs. pattern direction) and SCs with parallel orientation (=; i.e. with alignment angle ≤ 30° vs. pattern direction). Actin fibers follow the orientation of the cell body, in particular for the SCs oriented in perpendicular direction with respect to the nano-rippled one. n ≥ 3. Data= mean ± SEM: #P < 0.05, Student *t*-test, unpaired.

In order to evaluate the actin organization, the actin signal was also analyzed by image FFT, which returns the actin fiber dispersion and directionality (see *Materials and Methods* of this chapter for further details).

The actin directionality (an indicator for the overall degree of actin orientation vs the nano-ripple main direction) was considerably affected by both R_{LD} and R_{HD} topographies.

In fact, actin stress fibers mostly followed the orientation of the cell bodies, with directionality of (63 ± 12)° and (71 ± 5)° for SCs perpendicularly oriented on R_{LD} and R_{HD}, respectively. The same holds for SCs with parallel alignment on R_{LD} [directionality = (24 ± 7)°, P=0.05 vs SC perpendicular], while on R_{HD} this behavior is significantly less pronounced [directionality = (39 ± 20)° (**Figure 5.9 c**)]. The actin

dispersion parameter (an indicator for the angular spread of the actin fluorescence signal) was instead almost the same on all the tested substrates, showing an average value of (13 ± 3)°.

The actin-rich filopodia/lamellipodia located at the tip of SC protrusions were analyzed in the same way, but their actin cytoskeleton was not evidently influenced by the presence of the nanoripples.

Overall, these data demonstrate that PET nano-ripples can effectively tune the spatial organization of SC actin cytoskeleton, and suggest that on these substrates the actin content can be increased in cells with perpendicular alignment with respect to those with parallel alignment.

5.1.6 *Conclusions.*

In this part of Chapter 5 I have illustrated the effects of multiscale periodic structures on SCs behavior by pure contact interaction.

I have developed a new three-step fabrication process, which employs the use of PFPE intermediate mold technique to replicate R_{LD} and R_{HD} hierarchical nano-rippled structures. The entire transfer process was finely tuned to replicate the nanoripples topographies from germanium substrates onto the final PET surfaces.

Overall, PET R_{HD} nano-ripples emerged as the most effective scaffold in regulating SCs adhesion and growth. Remarkably, SCs oriented perpendicularly with respect to the main direction of the nano-rippled patterns, probably thanks to an actin fiber mediated selection process.

Since topographical modification of the cell/substrate interface is an important regulator of cellular adhesion and function, these results provide information on the possible use of hierarchical nanometric elements for tissue engineering applications.

5.2 Neuronal contact guidance and YAP /TAZ signaling on ultra-small nanogratings.

Previous studies conducted by my group have demonstrated that plastic nanogratings (**NGs**, *i.e.* alternating lines of sub-micron grooves and ridges, in the range between 500 and 2000 nm in linewidth) can promote neurite alignment and bipolarity of PC12 neuronal cells upon administration of NGF, simply by the contact guidance mechanism [250], [251]. In these studies, adhesion on the ridges imposes a geometrical and directional constraint to FAs that results in neuronal polarization via the ROCK-mediated pathway [105], [252], [253], [254]. As already mentioned, after nerve injury the axons need to regrow back to their targets and regain functions; otherwise, axon degeneration would hamper nerve tissue regeneration. SCs, together with tissue macrophages and inflammatory cells, remodel the environment to make it more suitable for axonal regrowth [255]. Furthermore, myelinated SCs can secret various neurotrophins such as nerve growth factor (NGF) to induce neurite elongation and regeneration [255].

In this category, an active area of research involves the development of a biodegradable conduit which contains SCs for the promotion of axonal regeneration. Therefore, mass production of pure SCs within a short period of time is a prerequisite to achieve this aim. Nonetheless, isolation and purification of SCs is usually a complex process. This complexity is caused by fibroblast contamination which is due to the higher and faster proliferation rate of fibroblasts than SCs [256].

Hence, for *in vitro* nerve regeneration research, PC12 cells were widely used as the model cells due to their ability to be passaged and easily differentiated into neuron-like cells. Cell lines that are capable of continuous replication and that display differentiated properties have long been recognized as useful model systems for studies of differentiation and function.

The development of neuronal cell lines poses particular challenges. Since mature neurons are nondividing, a maximally useful neuronal model should be modulable between a state in which it can replicate and a state in which it is nondividing as well as neuronally differentiated [257]. Among the most striking properties of the PC12 line, there is its capacity to respond to the SCs-secreted NGF, a protein that profoundly influences the growth and development of sympathetic and certain sensory neurons [258]. Despite that the behavior of the PC12 cells can

been affected by culture conditions, horse serum, which may inhibit NGF responses, and by high plating density, which inhibits NGF responses [259], the overall effect of NGF on PC12 cells is to convert them from the population of the replicating chromaffin-like cells to a population of nonreplicating sympathetic-neuronlike cells [257].

The best results for PC12 neurite alignment and bipolarization were obtained with NGs having 1 μm periodicity (*i.e.* 500 nm linewidth) [105]. However, in literature there are only few studies about cellular behavior in response to NGs with lateral period smaller than 1 μm.

Recent studies have emphasized the involvement in mechano-sensing of Yes-associated protein (**YAP**) transcription factor [260], [261]coupled with its transcriptional coactivator (**TAZ**), with a crucial role in correlating external mechanical stimuli with changes in gene expression [94], [262], [263]. More specifically, changes in ECM stiffness can determine modifications in cytoskeleton organization and tension, shuttling the YAP/TAZ complex to the nucleus [99] and influencing the mechanotransduction process at FA level [264], in a feedback loop between cytoskeleton and nucleus. Nowadays, the influence of substrate stiffness on YAP localization is known [99], but the effect of nanotopography on the activation and intracellular localization of YAP has not been yet deeply explored.

This section of the Chapter 5 is dedicated to the elucidation on neuronal contact guidance on ultra-small NGs. Substrates with lateral period from 1000 nm (considered as a reference substrate owing to its known ability to exert excellent contact guidance) down to 200 nm were fabricated in COC by a two-step NIL process starting from molds produced by electron beam or laser interferometric lithography. The impact of ultra-small NGs on cell morphotype, neurite alignment, FA development and YAP/TAZ activation was investigated in NGF-differentiating PC12 cells by confocal and total internal reflection fluorescence (**TIRF**) microscopy, and at molecular level. It was also explored the use of blebbistatin and nocodazole, two pharmacological treatments targeting cell contractility, to tune and recover the guidance where less effective.

5.2.1 *Ultra-small thermoplastic Nanogratings.*

Ultra-small NG topographies (*i.e.* anisotropic patterns of alternating lines of ridges and grooves) were developed with the aim to study the interaction between cells and anisotropic features with controlled nanometric periodicity, towards the typical dimensions of ECM cues.

To this end, a complete set of NGs was fabricated with 50% duty cycle (*i.e.* ridge width / period = 0.5) and period 1 μm (named T1, groove depth = 350 nm), 600 nm (named T600, groove depth = 300 nm), 400 nm (named T400, groove depth = 200 nm) and 200 nm (named T200, groove depth = 100 nm). Given our previous results [40], the T1 geometry was here considered as the *gold standard* guidance topography for our neuronal cell model.

NG patterns were replicated from initial molds into biocompatible and transparent COC thermoplastic polymer foils by exploiting perfluoropolyether (**PFPE**) intermediate molds, as described in *Materials and Methods* and in [219]. Briefly, PFPE intermediate molds were obtained by pouring a PFPE dispersion on top of each initial mold, and then crosslinking with UV light (**Figure 5.10 a**). The final NG replicas were produced via the PFPE molds into COC films by NIL (**Figure 5.10 b**).

As shown in **Figure 5.10 c**, both ridges and grooves retained their width after the two replica processes. In particular, ridges were laterally squared and straight, thus maintaining the grating initial profile and dimensions. NGs did not present discontinuities as holes or cracks along the ridges, thanks to the correct calibration of NIL process in terms of working temperature and applied pressure. Moreover, the use of a soft mold instead avoided nano-feature disruption during NIL, ensuring the nanopattern continuity on the whole patterned area [219].

The nanopatterns were further characterized by AFM measurements (**Figure 5.10 d**), allowing to calculate their aspect ratio (defined as the ratio of ridge height over width). The following periodicities were then measured: 610 ± 20 nm for T600 (ridge width = 300 ± 30 nm, ridge height = 300 ± 20 nm, aspect ratio = 1.0± 0.1); 400 ± 10 nm for T400 (ridge width: 210 ± 20 nm, ridge height: 200 ± 20 nm, aspect ratio = 1.0± 0.2); 200 ± 10 nm for T200 (ridge width: 110 ± 20 nm, ridge height: 95 ± 15 nm, aspect ratio = 0.9± 0.2). As reference, T1 showed 1000 ± 30 nm periodicity (ridge width: 505 ± 25 nm, ridge height 350 ± 30 nm, calculated aspect ratio 0.7± 0.1;

(all dimensions are mean ± SD, calculated using at least ten profiles extracted from 3.5 μm × 3.5 μm AFM measured area for each NGs).

By a Fast Fourier Transform (**FFT**) analysis on the AFM profiles the directionality of the different NGs was estimated (***see Materials and Methods*** for details). Directionality amplitudes (normalized to the value measured for T1) were 0.52 ± 0.03 for T600 (peak centered at 1.67 ± 0.05 μm^{-1}), 0.19 ± 0.01 for T400 (peak centered at 2.43 ± 0.01 μm^{-1}), 0.14 ± 0.01 for T200 (peak centered at 5.14 ± 0.01 μm^{-1}) and 0.01 ± 0.01 for the flat substrate (peak centered at 0.34 ± 0.06 μm^{-1}). All NGs showed a higher directionality if compared to flat surfaces (P<0.001 T1-T600-T400-T200 *vs.* Flat, Tukey's test), as expected. Among the different NGs, it was found an increasing trend with the period (P < 0.001 T1 *vs.* T600, T1 *vs.* T400, T1 *vs.* T200; P < 0.001 T600 *vs.* T400, T600 *vs.* T200; P<0.05 T400 *vs.* T200, Tukey's test).

It is noteworthy that directional signal decreases in intensity with the decrease of the NG periodicity (**Fig. 5.1d**); therefore, PC12 perceived a different direction stimulus on the different NGs. This reduced substrate directionality signal may take part in the neurite alignment process when the periodicity is downscaled [265].

Given that a good surface hydrophilicity generally promotes cell adhesion and spreading, in order to further characterize the substrate surface properties, water wettability was evaluated by performing water contact angle measurements (**Figure 5.10 f**). As shown in **Figure 5.10 f**, T600, T400 and T200 were more hydrophilic than the T1 and Flat (P < 0.001, Tukey's test), showing contact angles of 82 ±1 °, 80 ± 2 ° and 78 ± 3 °, respectively.

In summary, biocompatible thermoplastic NGs were fabricated with lateral periodicity ranging from 1 μm down to 200 nm, with aspect ratio between 0.7 (T1) and 1 (T600, T400 and T200). These nanostructures were replicated by a thermal embossing process, using PFPE intermediate molds to preserve the original molds and enhance the fabrication process yield. For all ultra-small NGs, the topographies were preserved during the entire two-step replica process.

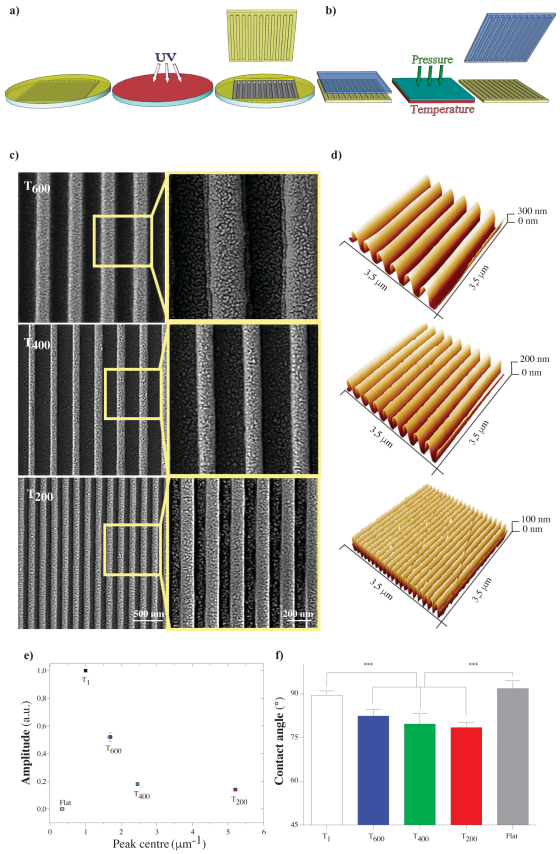

Figure 5.10 **Ultra-small nanograting fabrication scheme and surface characterization.** a) PFPE intermediate mold (in yellow) fabrication via UV-crosslink process and b) its use for the subsequent thermal NIL process to produce COC replicas (in light blue). c) Representative Scanning Electron Microscopy images (with high magnification insets) of the COC NGs T600, T400 and T200. d) AFM measurements of NG final COC replica, for 3.5×3.5 μm^2 areas. e) NG directionality signal amplitude by FFT analysis: the reported values were normalized to T1 value. *** $P < 0.001$ T1 vs. T600, T400, T200 and T600 vs. T400, T200; * $P<0.05$ T400 vs. T200; One-way ANOVA Tukey's test. f) Contact angle measurements of COC NGs. *** $P < 0.001$ T1 vs. T600, T400, T200 and Flat vs. T600, T400, T200 (One-way ANOVA, Tukey's test). All data are mean ± SD.

5.2.2 *Neurite contact guidance*

In order to address the neuronal guidance on NGs with very small periodicity, PC12 cells were seeded on the complete set of NGs (periods from 1 μm down to 200 nm), and neuronal differentiation was induced by NGF stimulation (100 ng/ml) (**Figure 5.11 a**). The emission of neuronal protrusions (neurites) was influenced by the local substrate nanotopography, and this effect was quantified by measuring two neurite morphological parameters – *neurite alignment* (the average angle between neurites and NG direction) and *length* – at t = 24 h by bright-field optical microscopy (**Figure**

5.11 a). As expected, neurites interacting with T1 extended along the pattern direction (neurite alignment = 6 ± 1°). Neurite alignment was maintained on T600 (8 ± 1°) and T400 (8 ± 2°) (P>0.05 *vs*. T1, P<0.001 *vs*. Flat; Tukey's test); instead it was observed a significant alignment loss by decreasing the period down to 200 nm (23 ± 2°) (P<0.001 T200 *vs*. T1/T600/T400; Tukey's test) (**Figure 5.11 b**).

However, T200 directionality could still be retrieved by PC12, inducing a partial neurite alignment if compared to the random neuritic distribution that was measured on Flat substrates (44 ± 2°; P<0.001 T200 vs. Flat; Tukey's test).These results indicate that NGF-induced differentiation is not inhibited by the NGs, and that neurite alignment is sensitive to ultra-small NGs and their directionality signal, despite neurite guidance is reduced on T200 substrates.

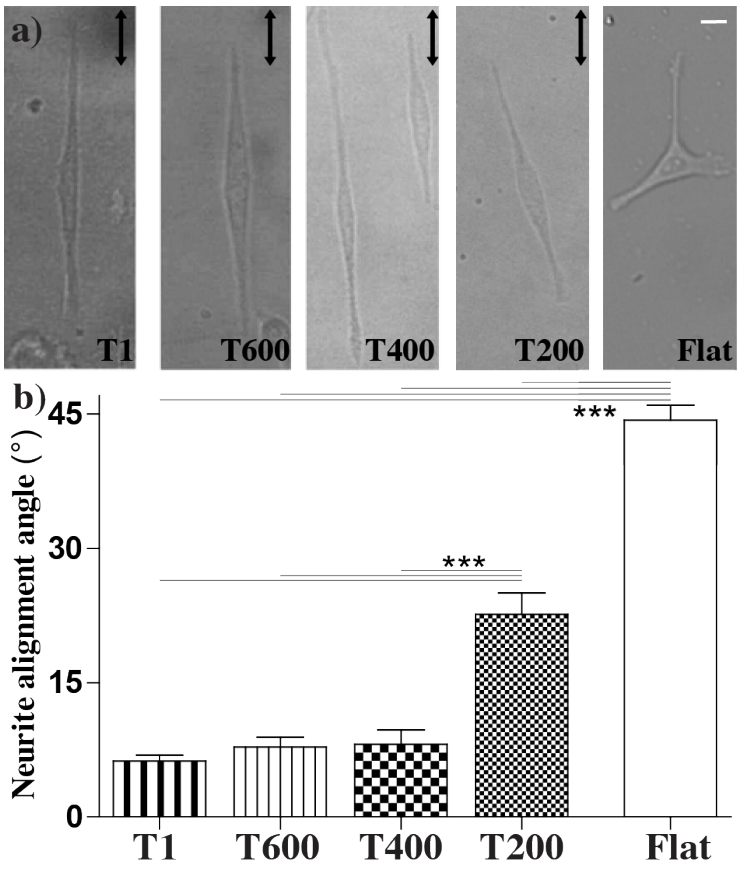

Figure 5.11 **Neurite alignment along NGs**. a) Bright-filed images of PC12 neuronal cells on T1, T600, T400, T200 and Flat, at 24 h; the arrows indicate the NG direction; scale bar = 10 μm. b) Neurite alignment on NGs. *** P< 0.001 (One-way ANOVA, Tukey's test); at least 300 cells - 450 neurites- were analyzed for each substrate (n ≥ 6).

5.2.3 *Focal adhesion maturation is modulated by ultra-small nanogratings.*

It was previously shown that in PC12 cells the induction and growth of neurites along 1-μm-period gratings were critically controlled by the establishment and maturation of FAs [105], [252], [253]: here, in fact, FAs were squeezed and grew directed along ridges. Ultra-small NGs were also expected to importantly affect FAs because their typical length-scale still is of the order of that of ECM protein clusters.

In order to validate this hypothesis, PC12 cells were transiently transfected with EGFP-Paxillin, a signal-transduction protein present in early and mature FAs [93], and differentiated by NGF on the ultra-small NGs. Paxillin was then selectively visualized at the cell basal-membrane by TIRF microscopy (**Figure 5.12 a**) and FAs were analyzed by measuring their alignment (°) with respect to the NG direction **(Figure 5.12 b**) and quantifying their number per cell (**Figure 5.12 c**). The progressive reduction of NG periodicity induced a decrease in the overall *percentage of FAs alignment*, reported here as the percentage of FAs with an alignment angle ≤ 15° vs. NG direction **(Figure 5.12 b**), as it was already found for neurite guidance (**Fig. 2b**). At first sight, FA alignment loss started on T400 (56 ± 1 %) and it further increased on T200 (42 ± 4 %). The percentage of FA alignment was indeed significantly lower if compared to that measured for T1 (70 ± 4%) and T600 (71 ± 4%) ($P<0.001$ T200 *vs*. T1 and T600, Tukey's test). However, T400 and even T200 could still partially polarize the FA development along NGs in comparison to isotropic Flat substrates (17 ± 2%) ($P<0.001$ T400 *vs*. Flat, $P<0.01$ T200 *vs*. Flat; Tukey's test; **Figure 5.12 b**).

The decrease of NG periodicity also induced a progressive increase in the number of FAs/cell (**Figure 5.12 c**). Interestingly, the number of FAs developed by each cell increased from 9 ± 1 on T1 and 13 ± 2 on T600 to 20 ± 1 on T400 and 23 ± 2 on T200, with values similar to those obtained for the Flat surface (26 ± 3) ($P<0.05$/$P<0.001$ T1 *vs*. T400, T200 and Flat; $P<0.05$/0.01 T600 *vs*. T200 and Flat; Tukey's test, **Figure 5.12 c**). Overall, FA spatial organization and number per cell were progressively affected by decreasing the period of ultra-small NGs, well correlating with neurite guidance. T400 behaved such as a "border land" substrate between FA alignment and misalignment regimes.

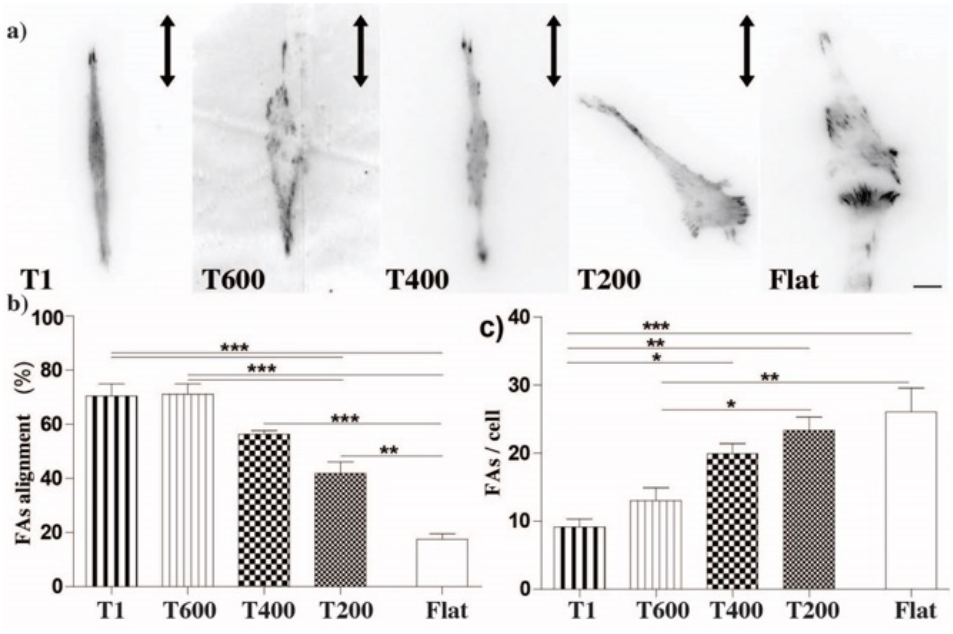

Figure 5.12 **Impact of reduced NG periodicity on FA assembly and spatial distribution.** a) EGFP-Paxillin rich adhesions on NGs imaged by TIRF microscopy; scale bar = 10 μm. b) FA alignment on different NGs, reported as the % of FAs with alignment ≤ 15°. **/*** P< 0.01/0.001 (One-way ANOVA, Tukey's test). c) Number of FAs per cell on different substrates. * P<0.05, ** P<0.01 and *** P<0.001 (One-Way ANOVA, Tukey's test); at least 30 cells or 400 FAs were analyzed for each sample (n ≥ 4).

FA maturation was then analyzed on the different substrates (**Figure 5.13**). FAs were classified as *aligned* (in case of alignment angle ≤ 15°) or *misaligned* (in case of alignment angle > 15°). Even if the overall average FA size did not show major changes by reducing the NG periodicity, the maturation of the aligned FA was progressively impaired by the reduction of NG periodicity (**Figure 5.13 a**), progressively becoming indistinguishable from the misaligned ones. The size of aligned FAs was larger on T1 (*i.e.* the substrate with the best neurite guidance behavior, 1.7 ± 0.1 μm^2) with respect to those developing on substrates with less neurite-guidance abilities, in particular on T400 (1.2 ± 0.1 μm^2) and Flat (1.3 ± 0.1 μm^2) (for Aligned FAs: P<0.05 T1 *vs*. T400 and Flat, Tukey's test; **Figure 5.13 a-*left panel***). Moreover, aligned FAs were larger than the misaligned ones (**Figure 5.13 a-*right panel***) for cells on T1 (1.7 ± 0.1 μm^2 and 1.0 ± 0.1 μm^2, respectively) (P<0.001, Size FA Aligned *vs*. Misaligned on T1, Student's t-test), T600 (1.5 ± 0.1 μm^2 and 1.1

± 0.1 μm²) (P<0.01, Student's t-test) and on T400 (1.2 ± 0.1 μm² and 1.0 ± 0.1 μm²) (P=0.05, Student's t-test).

Considering misaligned FAs, a general trend could not be identified although T200 and Flat showed the tendency to allow more effective maturation (**Figure 5.13 a-*right panel***). In summary, these experiments demonstrated that the reduction of NG periodicity modulated FA maturation. T1 and T600 patterns could favor the maturation of aligned FAs while reducing misaligned-FA development. T400 represented the limit geometry where aligned FAs could develop larger in size than the misaligned ones, while on T200 they did not.

These findings lead as to the concept of the minimal critical size of FAs in cells. Some studies in literature sustain the idea that proteins within FAs assemble into higher order structures on the ~100 nm length scale [266]. Because of pure physical patterns in the ~ 100 nm range dimension are difficult to fabricate, most of the studies on FA size reported in literature have been performed on biochemical or nanopillar patterns. Human endothelial cells (HUVEC) showed compromised and no pattern-specific adhesion on fibronectin nanodots smaller than 100 nm [267]. Arnold *et al.* produced adhesive patches of RGD peptides with side lengths ranging from 100 to 3000 nm and showed that rat embryo fibroblasts (REF) adhered on patterns below 500 nm bridging multiple adjacent ligand domains *via* individual actin fibers [268]. In the case of MDCK epithelial cells cultured on polymeric NOA-61 nanopillars [269] (diameters ranging from 200 nm to 700 nm), the size of the FAs was confined by the size of the nanopillars. As in the present case, the number of FAs increased and the total FA area decreased as the size of nanopillars decreased. However, the FAs formed on the 200-nm nanopillars were larger than those formed on the 400-nm nanopillars.

Although the spatial limitations of the nanopillars prevented the maturation of focal complexes to focal adhesions, cells exerted considerable force on the 200-nm nanopillars, leading to bending of the nanopillars to form larger focal adhesions from adjacent focal complexes. Similarly NIH 3T3 fibroblasts cultured on PMMA nanopillars with diameter of 70 nm formed very small adhesions, which led to a higher cells motility [270].

In order to better highlight this effect, all FAs were sorted in three categories (**Figure 5.13 b-c**): small (FA area ≤ 1 μm^2), intermediate (1 μm^2 < area ≤ 2 μm^2), and

large (> 2 μm^2), corresponding to different maturation stages [252]. For aligned FAs, lowering NG periodicity led to an increase of the small-FA population (from ~ 33% on T1 to a maximum of 57% on T400; P<0.01 T1 *vs.* T400 and P<0.05 T1 *vs.* T200, Dunnett's test), and reduction of large FAs (from ~ 30% to 14%; P<0.01 T1 *vs.* T400 and T200, P<0.05 T1 *vs.* Flat, Dunnett's test; **Fig. 4b**). Interestingly, the number of large FAs developing aligned on T1, T600 and T400 was much greater than that of large misaligned FAs (# Aligned FAs (%)- Large *vs.* Misaligned FAs (%)-Large: P< 0.01 for T1, P< 0.05 for T600 and T400, Student's t-test; **Figure 5.13 b-c, *darker columns***). No evident trends were instead identified for misaligned FAs (**Figure 5.13 c**). These data demonstrate that differentiating PC12 cells actively respond to the reduction of NG periodicity through the variation of FA development and spatial maturation. Overall T400 represents a limit substrate to control the directional development of FAs and the subsequent neurite guidance.

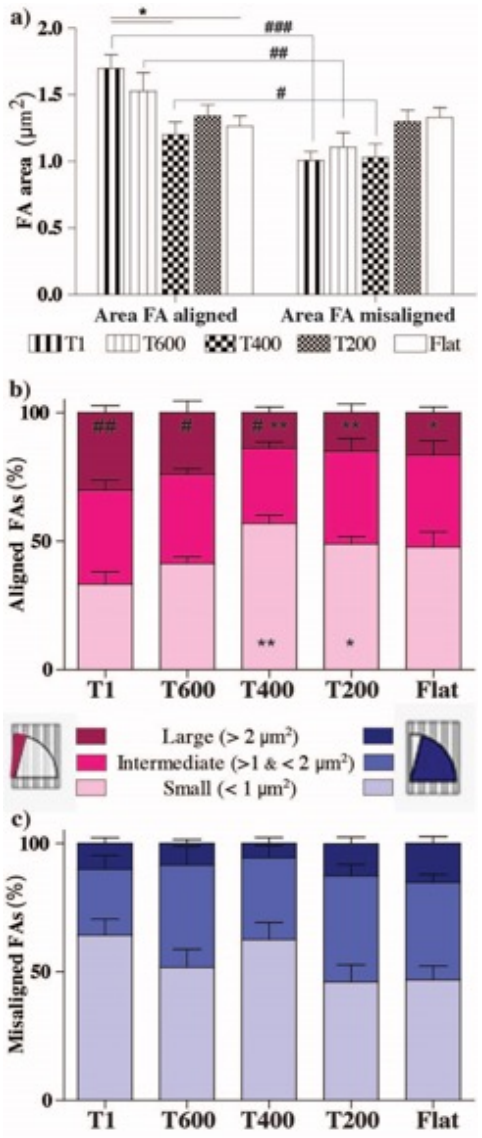

Figure 5.13 **Impact of reduced substrate dimensionality on FA maturation**. a) Average FA area (μm^2) is reported for *aligned* FAs (i.e. with alignment ≤ 15°; *left panel*) and for *misaligned* FAs (i.e. with alignment between 15° and 90°; *right panel*), on the different substrates. Aligned FA area *vs.* misaligned FA area: ### P<0.001, ## P<0.0, # P=0.05 (Student's t-test). Aligned FA area: * P<0.05 T1 *vs.* T400 and Flat (One-Way ANOVA, Tukey's test). **b**) Distribution of FA size NGs. Size distribution of aligned (0 - 15°) FAs, as function of the substrate. The % of small (area ≤ 1 μm^2), intermediate (1 μm^2< area ≤ 2μm^2) and large (area > 2 μm^2) FAs is reported in *light*, *normal* and *dark* pink color, respectively. Small FAs: */** P<0.05/0.01 *vs.* T1; Large FAs: */** P<0.05/0.01 *vs.* T1; (One-Way ANOVA, Tukey's test). **c**) Size distribution of misaligned (15 - 90°) FAs as function of the substrate. The % of small (area ≤ 1μm^2), intermediate (1 < area ≤ 2μm^2) and large (area > 2μm^2) FAs is reported in *light, normal* and *dark* blue color, respectively. Large-Aligned FAs (%) *(darker pink columns*-in **b**) *vs.* Large-Misaligned FAs (%) *(darker blue columns*- in **c**): ## P< 0.01 for T1, # P< 0.05 for T600 and T400, Student's t-test. At least 30 cells or 400 FAs were analyzed for each sample (n ≥ 4).

Because of FAs mediate neurite outgrowth and the integration of topographical information into cytoskeletal signaling [265], the effects of ultra-small NGs on the FA pathway were investigated at molecular level, focusing on the activation of FA kinase (FAK), and on the levels of a set of FA scaffold proteins: Talin, Vinculin and Zyxin (**Figure 5.14**). In particular Zyxin is one of the focal adhesion components that are absent from focal complexes [271] and are recruited to adhesion sites after application of mechanical stress [272], [273], when FAs enlarge and mature. The activation of FAK was not affected by the NGs, as well as the levels of Talin and Vinculin ($P>0.05$). The total levels of Zyxin, which is present only in mature FAs, showed instead a decreasing trend by lowering the NG dimensionality, and it was significantly reduced on T200 ($P< 0.05$ T1 *vs.* T200, Dunnett's test) (**Figure 5.14 d**).

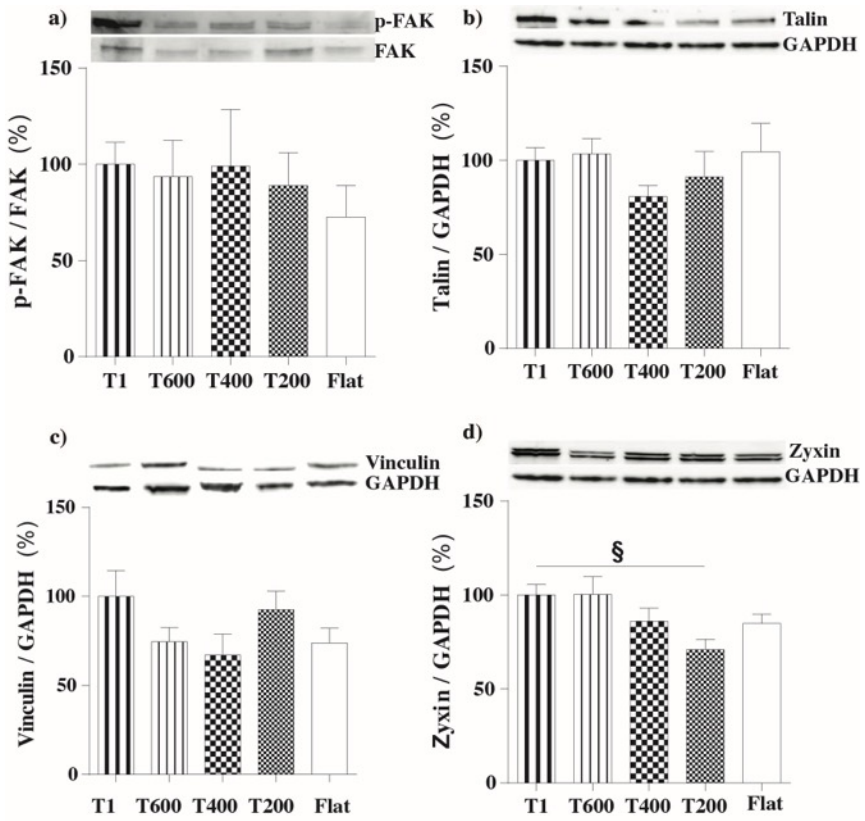

Figure 5.14 **Activation of the FA pathway in PC12 cells growing on ultra-small NGs.** Representative Western-blot panels and blot analysis of phospho-FAK/ FAK (a), talin (b), vinculin (c), and zyxin (d) levels. Results (normalized to GAPDH levels) were reported in % in respect to T1 levels. d) * $P < 0.05$ T1 vs. T200 (One-Way ANOVA, Dunnett's test); $n \geq 4$.

5.2.4 *Pharmacological tuning.*

It was previously demonstrated that PC12 contact guidance on NGs requires myosin-II / Rho-mediated contractility, and that the tolerance to topographical noise can be tuned by pharmacologically interfering with this signaling pathway [265].

Therefore PC12 cells grown on ultra-small NGs were exposed to nocodazole (**Noco**), a microtubule depolymerizing agent that can activate the RhoA-mediated cell contractility [274] and improve neurite contact guidance on noisy NGs [265], and to blebbistatin (**Bleb**), a myosin-II-contractility inhibiting drug, that was shown to impair neurite contact guidance [252], [265] (**Figure 5.15**).

In line with the previous results, Bleb treatment impaired neurite guidance along T1 ($P<0.05$ T1-Ctrl *vs*. T1-Bleb, Student's t-test), with a similar trend on T600 and T400. We then measured neurite alignment in presence of nocodazole: Noco had not detectable effect on the "well-guiding" NGs T1, T600 and T400. However, Noco induced a light improvement in the neurite alignment along T200: there was in fact a reduction of the average neurite alignment angle (*i.e.* better guidance) on T200+Noco (**Figure 5.15**), from 23 ± 2° on T200 Ctrl to 16 ± 3° on T200+Noco, although this difference was not statistically significant (T200 Ctrl *vs*. T200+Noco, $P=0.08$). Neurite growth and length were not affected by both drugs' treatments. These results confirm the key role of the cell-contractility machinery in topographical guidance also on ultra-small NGs.

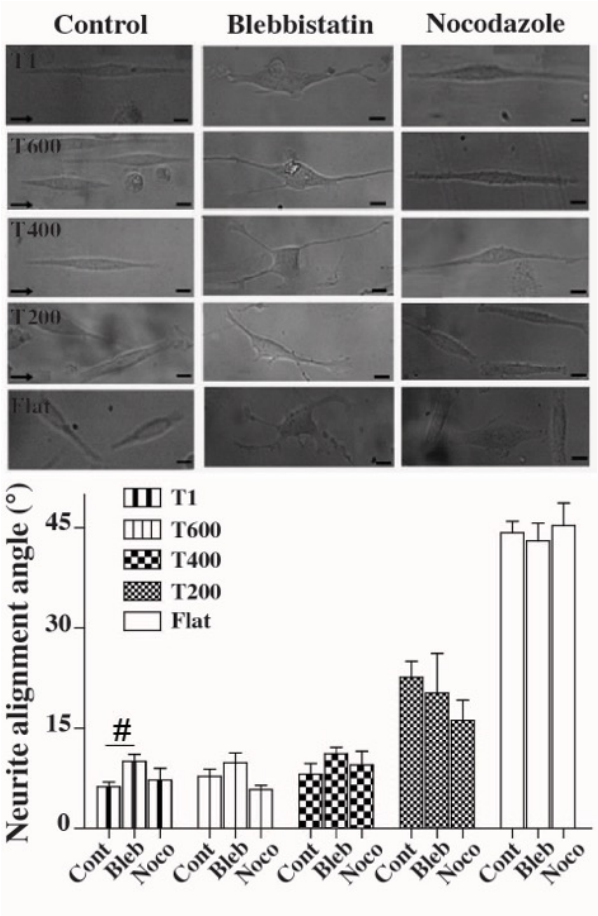

Figure 5.15 **Neurite alignment along ultra-small NGs: role of cell contractility.** Bright-filed images (Top panel) of PC12 neuronal cells on different NGs, in control conditions and in presence of blebbistatin 25 μm (Bleb) and nocodazole 10 nM (Noco); the arrows indicate the NG direction; scale bars = 10 μm. Neurite alignment on NGs: # P< 0.05 T1-Cont vs. T1-Bleb, Student's t-test. Data are reported as mean ± SEM (At least 300 cells - 450 neurites- were analyzed for each substrate in control conditions (n ≥ 6), and 110 cells - 180 neurites- for each substrate with drugs' treatments (n ≥ 3).

5.2.5 *YAP/TAZ signaling.*

It was finally investigated the involvement of YAP/TAZ signaling in neurite contact guidance on ultra-small NGs. As first, it was measured the YAP level, which resulted unaffected by the presence of the nanotopography (**Figure 5.16 a**). Once activated, YAP concentrates into the nucleus. It was thus performed immunostaining for YAP to investigate its intracellular localization (**Figure 5.16 b**), with the aim of testing if the different guidance performance could be linked to different activation of the YAP/TAZ pathway. The nuclear/cytoplasm localization

ratio was similar on the different NGs (**Figure 5.16 c**). Nevertheless, YAP was more activated and localized in the nucleus of cells cultured on NGs (1.80 ± 0.04) with respect to those on Flat (1.5 ± 0.1, P<0.01 NGs *vs*. Flat, Student's t-test; **Figure 5.16 d**). The expression of YAP was not influenced by substrate nanotopographies, whereas its localization (and therefore likely its activation) was.

The nuclear localization of YAP/TAZ complex has been attributed to different factors, including low cell density [275], mechanical stretching and substrate stiffness [99]. Here, the cell density (low) was the same on all our NGs, as well as their substrate stiffness (2.5 ± 0.2 GPa [105]), therefore it was envisioned that the YAP nuclear localization is induced in PC12 cells by the NG topography itself, likely *via* cytoskeleton remodeling and mechanical stretching. It is, in fact, well known that NGs activate cell polarization and cytoskeleton via the Rho-mediated pathway [105], [253], [265].

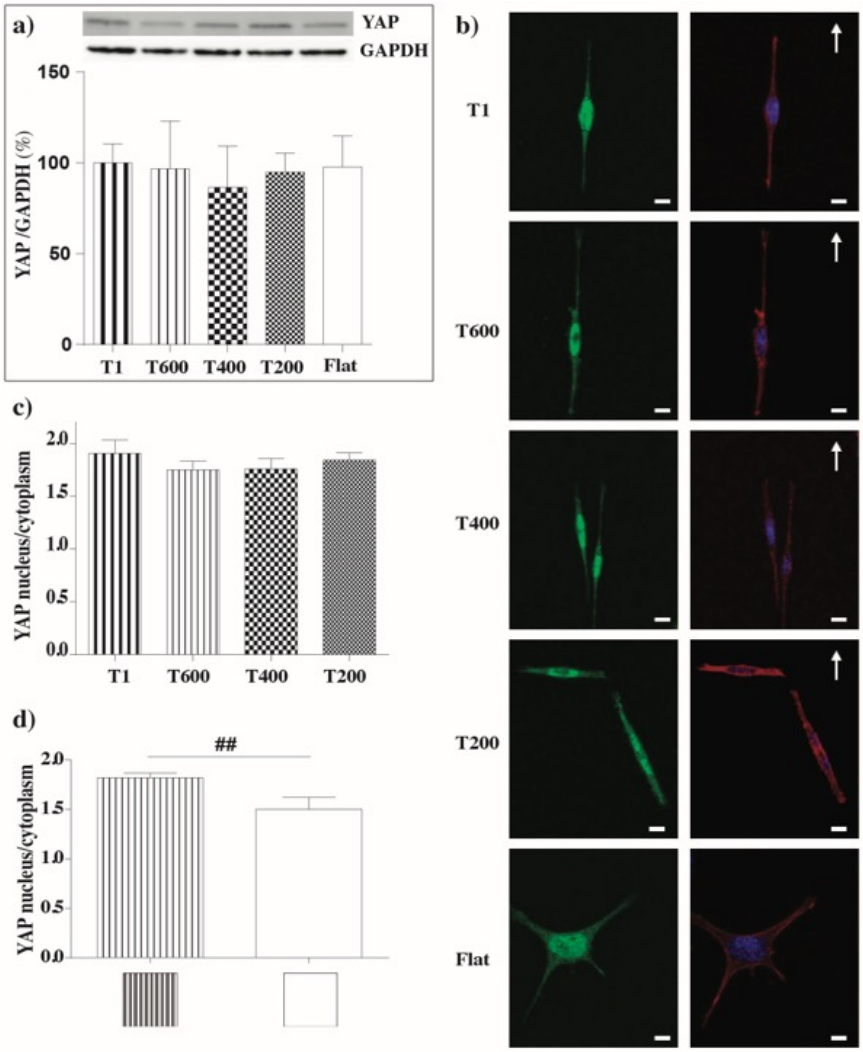

Figure 5.16 **Activation of the YAP/TAZ pathway in PC12 cells differentiating on ultra-small NGs.** a) Representative Western-blot panels and blot analysis of YAP 1 expression levels. Results (normalized to GAPDH levels) were reported in % in respect to T1 levels; n ≥ 3. b) Confocal representative images of Yap1 (green, first column) and actin fibers (red) with nuclear (blue) staining in PC12 cells on different substrates; scale bars =10 μm. c) YAP/TAZ intracellular localization: YAP activation is reported as YAP/TAZ nuclear/cytoplasmic ratio on different; at least 25 cells were analyzed for each sample (n ≥ 3). d) YAP/TAZ nuclear/cytoplasmic ratio on NGs and Flat surfaces: #P<0.01 NGs vs. Flat (Student's t-test).

It was finally tested the effect of drugs acting on cell cytoskeleton, Noco and Bleb, on YAP/TAZ intracellular localization, taking into account that blebbistatin has been reported to block YAP/TAZ activation [99]. Three different substrates were chosen for these experiments: T600 as good-guidance substrate, T200 as impaired-guidance substrate, and Flat as control substrate. PC12 cells were differentiated in

the presence of Noco or Bleb and we measured YAP intracellular localization by immunostaining (**Figure 5.17 a**). Overall the YAP nuclear/cytoplasm ratio was not changed by either Noco or Bleb treatments on both T600 and T200 (**Figure 5.17 b**). On the Flat a slight increase was instead visible on the treated samples.

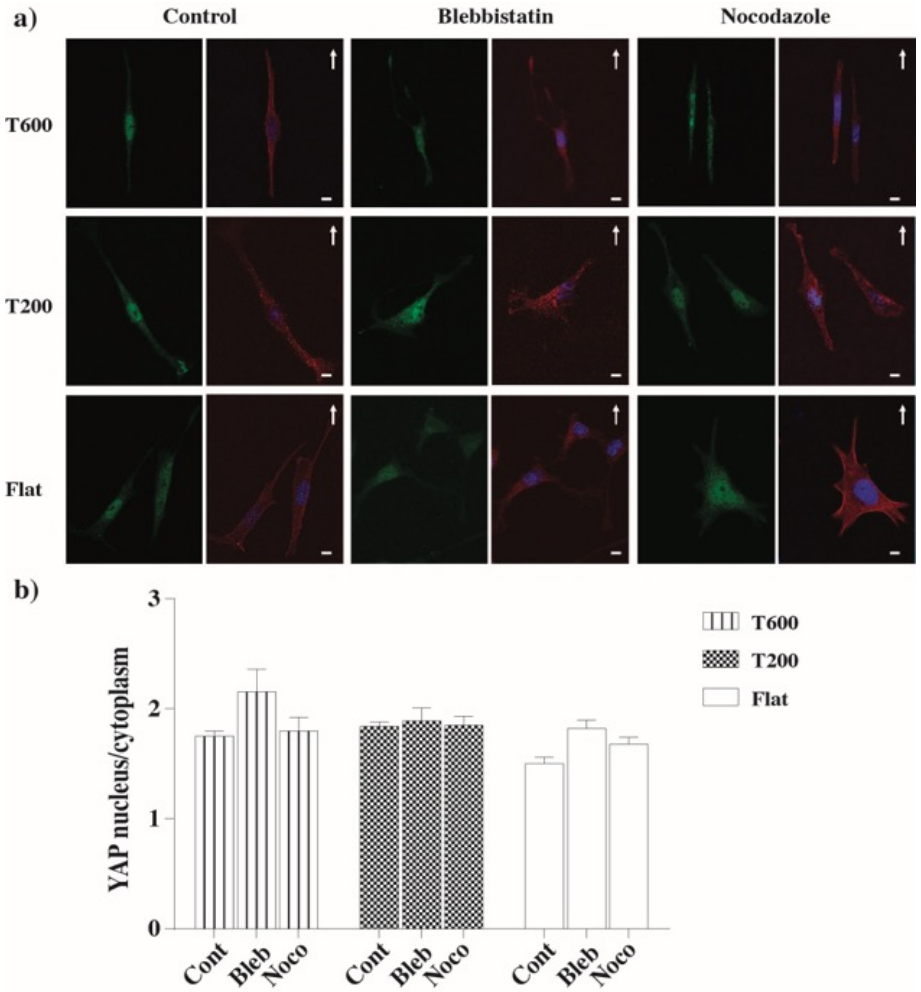

Figure 5.17 **Effect of contractility targeting drugs on the activation of the YAP/TAZ pathway.** a) Confocal representative images of YAP1 (green, first column) and actin fibers (red) with nuclear (blue) staining in PC12 cells on T600, T200 and Flat substrates in control conditions and after treatment with Blebbistatin (25 μM) and Nocodazole (10 nM); scale bars =10 μm. b) YAP/TAZ intracellular localization after drug treatments: YAP activation is reported as YAP/TAZ nuclear/ cytoplasmic ratio on T600, T200 and Flat; at least 25 cells were analyzed for each sample ($n \geq 3$), for both control and treated conditions.

It is known that the substrate stiffness tightly controls the subcellular localization of YAP/TAZ [99], in fact if cells grow on hard substrates, YAP/TAZ complex translocate to the nucleus. Moreover, the activation of YAP/TAZ in hMSCs cultured on soft PEG hydrogels was dependent on the previous culture time on stiff tissue culture polystyrene (~ 3 GPa) [276]. The COC substrates, both ultra-small NGs and Flat, have a stiffness over 2 GPa [105], which was above the stiffness value able to activate YAP/TAZ in other cell types, and it may result in a "basal" YAP/TAZ nuclear translocation in our experimental model which may partially mask drugs'action, in particular on NGs.

Taken together, these data demonstrate that PC12 cells have an increased YAP nuclear localization (and hence YAP/TAZ activation) is cultured on NG topographies. However, pharmacological tuning by nocodazole or blebbistatin had no major effects on YAP nuclear localization.

5.2.6 *Conclusions.*

In this part of Chapter 5 I have shown the neurite *contact guidance* performances of PC12 cells on ultra-small NGs, with the aim to investigate the lower limit in dimensionality for proper neuronal contact guidance, and the molecular mechanism mediating this process, at the level of FA and YAP/TAZ pathways.

I fabricated ultra-small NGs by a new two-step fabrication process, to replicate NG with periodicities below few hundreds of nanometers with high fidelity and yield. Overall, the T200 NG emerged as the NG where neurite contact guidance was compromised, in terms of neurite alignment, FAs spatial distribution and maturation level. Finally, it was demonstrated that nocodazole can improve neurite contact guidance when it is not optimal.

I found that YAP/TAZ sub-cellular localization significantly shifted towards nucleus on all NG patterns with respect to Flat surfaces, suggesting that nanotopographical guidance response in cells can activate YAP/TAZ.

5.3 Materials and Methods.

Fabrication processes.

Germanium mold preparation.

Two specimens of 1×1 cm^2 area, obtained from a commercially available bulk Ge <100> wafer, were irradiated at room temperature with Au^+ ions at 26 keV energy and at an angle of incidence of 60° with respect to the surface normal. Two ion fluences were used, namely 1×10^{17} ions·cm^{-2} for samples named Ripple Low-Dose (R_{LD}), and 4.3×10^{17} ions·cm^{-2} for samples named Ripple High-Dose (R_{HD}).

Ultra-small nanogratings molds fabrication.

Ultra-small NGs topographies (*i.e.* anisotropic patterns of alternating lines of ridges and grooves) were fabricated from initial molds by nanoimprint lithography with the following characteristics: T1 (period 1 μm, depth 350 nm), T600 (period 600 nm, depth 300 nm), T400 (period 400 nm, depth 200 nm), T200 (period 200 nm, depth 100 nm); period = ridge width + groove width.

T1 silicon mold was obtained by means of EBL and reactive ion etching (RIE) starting from commercial p-doped silicon wafer (SYLTRONIX, France), as previously reported [250].

T600 and T400 polymeric molds were fabricated by Laser interference lithography (LIL). A SPR220-1.2: PGMEA solution (2:3) was spun onto a silicon wafer with a spin speed of 4000 rpm for 30 s; SPR220-1.2 photoresist was purchased from Microposit (Shipley European Limited, UK), while PGMEA (propylene glycol monomethyl ether acetate) from MicroChem Corp (Newton, MA, USA). The sample was exposed to a 50 mW helium cadmium (HeCd) laser, emitting a TEM_{00} single mode at a 325 nm light source, with a beam incidence angle of 166° for T600, and of 24° for T400, and an exposure dose of 77 mJ/cm^2. The resist developing step was performed by immersing the samples in a MF24A/Milli-Q water (10:1) solution for 20 s [225]. The exposure and process parameters (i.e. beam incidence angle, exposure, developing time) were chosen in order to obtain gratings with a period of 600 and 400nm, 50% duty cycle.

The silicon T200 mold was purchased from ThunderNIL Srl (Basovizza, Trieste, Italy). Finally, flat control molds were obtained by silanization of 2x2 cm^2 flat silicon wafer.

PFPE intermediate molds.

PFPE resin (FLUOROLINK® MD 700, Solvay Speciality Polymers, Bollate, Italy) was mixed with 3%-wt photoinitiator Darocure 1173 ($C_{10}H_{12}O_2$, 405655 Sigma Aldrich, Gallarate, Italy) and poured on top of the Ge rippled surfaces, then crosslinked by UV-light (365 nm, 25 $mW \cdot cm^{-2}$). The exposure was performed in two steps: first, the sample was kept 180 s in nitrogen atmosphere, then 60 s in air. After curing, the PFPE film was peeled off and cleaned with nitrogen flow [219].

COC replicas.

COC foils (thickness 140 μm, Microfluidic ChipShop GmbH, Jena, Germany) were imprinted using an Obducat Nanoimprint 24 system (Obducat, Lund, Sweden) using the PFPE molds. After cleaning with 2-propanol, the COC substrates were placed on top of the molds and softened by raising the temperature up to 150 °C. A pressure of 50 bar was then applied for 300 s before cooling down to 70 °C, i.e. below the glass transition temperature of the copolymer (T_g = 134°C). Finally, the pressure was released and the mold was detached from the imprinted COC with a scalpel.

PET replicas.

PET foils (thickness: 250 μm, Coexpan, Montonate, Italy) were thermally imprinted in two steps: after 2-propanol cleaning, flat PET foils were placed on top of COC replicas, then warmed up at 75 °C. A pressure of 20 bar was then applied for 300 s, then the system was brought below the PET glass transition temperature (T_g = 75 °C), down to 50 °C and the pressure was finally released. A nitrogen flow was applied between the PET replica and the correspondent COC mold to easily detach one from the other.

Surface characterizations.

SEM measurements.

COC replicas of ultra-small NGs were imaged by SEM after coating them with a 5-nm thick gold layer by thermal evaporation. The metal layer was shorted to the SEM sample holder to avoid electron charging during the imaging characterization. The substrates were then loaded into a LEO 1525 field emission SEM and image acquisition was carried out by secondary-electron detection with the Everheart-Thornley detector in order to enhance the topography of substrates.

AFM measurements.

Topography and roughness were evaluated by AFM (Veeco Innova Scanning Probe Microscope, Veeco Instruments Inc., Santa Barbara, CA, USA), operating in tapping mode. Set scan frequency: 0.977 Hz; scanning areas (at least 5 per nanoripple sample, 3 per ultra-small NGs) of 5×5 μm^2 and 10×10 μm^2 (1024 samples/line each) in nanoripples case, 3,5 ×3,5 μm^2 and 10×10 μm^2 (512 samples/line each) for ultra-small NGs. At least three PET and COC replicas were imaged for each topography.

A silicon nitride tip with a nominal spring constant in the range of 0.2-0.8 N/m and a resonant frequency of 45–95 kHz was used. All the measurements were performed in air at room temperature and raw scan data were leveled by surface subtraction to remove possible sample tilts.

In the nanoripples case, roughness values were evaluated along different directions (0°, 22.5°, 45°, 67.5° and 90° with respect to the main direction of the pattern) by measuring the average roughness (Ra), the maximum vertical distance (Rmax) and the surface area difference (SAD) parameters on 3×3 μm^2 AFM images. Ra is defined as the arithmetic average of the absolute values of the surface height deviations measured from the mean plane within the area, Rmax represents the maximum vertical distance between the highest and lowest data points in the image following the surface subtraction on the area, and the SAD parameter is defined as the difference between the image three-dimensional surface area and the two-dimensional projected surface area. These three parameters allow the discrimination of differences among surfaces with comparable Ra values.

The scanned images were elaborated with the Nanoscope Analysis (9.0 version) software tool. Height and periodicity values were instead quantified by the use of the Gwiddion software (Gwiddion 2.47 version, Profile tool). Data are reported as mean ± SD

Substrate directionality evaluation.

Nano-ripple substrate directionality was quantified by analyzing the AFM images with the "Directionality" tool of the software FIJI (http://fiji.sc/Fiji)
This plug-in returned a directionality histogram by exploiting image FFT algorithms: isotropic images generate a flat histogram, whereas oriented images give a peaked histogram. These histograms were finally fitted by Gaussian curves that returned two parameters, dispersion (σ) and directionality (α) (the standard deviation and the center of the Gaussian curve, respectively), the first (σ) representing the degree of orientation of the image, the second (α) the direction in which it is oriented. We analyzed at least 12 fields per sample; image dimensions were kept fixed to 2 × 2 μm^2. Data are reported as mean ± SD.

For ultra-small NGs substrates, directionality was quantified by analyzing the AFM profiles with the "Signal Processing: FFT" tool of the software Origin. We selected only the FFT main peak, correspondent to the peculiar NGs periodicity. We analyzed at least 12 profiles (length 10 μm) for each NG image (image dimensions were kept fixed at 10 × 10 μm^2). We used AFM images of COC replicas for T400 and T600 substrates to extract the NGs profile, while AFM images of the initial silicon mold for T200 substrates, to avoid noisy peaks in the T200 profile caused by electrostatic interactions between the COC foil and the AFM tip. For all conditions (Flat, T600, T400 and T200) FFT signal amplitude values were normalized to the T1 values. Data are reported as mean ± SD.

Contact angle measurements.

Substrate wettability was evaluated by contact angle measurements acquired with a CAM 200 instrument (KSV Instruments, Helsinki, Finland). A deionized water drop was deposited on top of each substrate through a micro syringe.
To evaluate the wettability in both parallel and perpendicular directions with respect to the pattern orientation, the samples were rotated by 90° and three

different measurements were acquired for each direction, for both R_{LD} and R_{HD} PET replicas.

In the case of ultra-small NGs, the direction of the pattern did not influence the contact angle values, therefore data were reported as single values, without specifying the direction of measurement acquisition. All these measurements were performed in air at room temperature. Data are reported as mean ± SD.

Cell cultures.

SC Culture.

Primary SC cultures were established from sciatic nerves of adult Wistar rats. SCs were cultured in the presence of glial growth factor (GGF 63 ng mL^{-1}; SRP3055, Sigma) and Forskolin (10×10^{-6} M; F3917, Sigma) in Dulbecco's modified eagle medium (DMEM) supplemented with 10% Fetal Bovine Serum (FBS), 4×10^{-3} M L-glutamine and antibiotics. Cells were routinely immunodepleted by anti-rat CD90 antibody (1:500, MCA04G; AbD Serotec) to reduce the presence of fibroblasts.

Control experiments to check the fibroblast contamination levels were also performed with the anti-CD90 antibody (1:250; AbD Serotec). Before cell culturing, PET samples were sterilized with absolute ethanol (for 15 min at least) and then rinsed with H_2O. The resulting PET nanostructured surfaces were first coated with poly-D-lysine (100 μg·mL^{-1}, at room temperature for 30 min; P4832, Sigma) and then with laminin (50 μg·mL^{-1}, at 37 °C for 30 min) for proper cell adhesion. SCs (within the tenth passage) were seeded on PET nano-rippled scaffold at density of 35×10^3 cells cm^{-2} and cultured up to 7 days.

PC12 Cell Culture.

PC12 cells (CRL-17210, ATCC) were grown in RPMI medium supplemented with 10% HS, 5% FBS, 2 mM glutamine, 10 U/ml penicillin and 10 mg/ml streptomycin (Thermo Fisher, Waltham Massachusetts, USA) and were maintained in standard conditions (37°C, 95% humidity, 5% CO_2).

Cells (within the 15th passage) were cultured until sub-confluence, then harvested for cell tests, pipetted to obtain a single cell suspension (through a 10 ml

syringe with G21 needle), and seeded onto the NGs at a final concentration of 104 cells/cm2. Before cell culturing, the imprinted dishes were sterilized by treatment with ethanol and then rinsed twice with H_2O_{mQ}.

For *in vitro* experiments, PC12 were seeded on substrates (50000 cells/ cm^2 or 100000 cells/ cm^2 – for western blot) and neuronal differentiation was induced by treatment with nerve NGF, 100 ng/ml. PC12 cells were allowed to adhere for 7-8 h before stimulation with NGF.

For contractility experiments during PC12 differentiation, PC12 were treated with nocodazole (Methyl-[5-(2-thienylcarbonyl)-1H-benzimidazol-2-yl]-carbamate, dissolved in DMSO, 10 nM; Noco) or blebbistatin (1-Phenyl-1,2,3,4-tetrahydro-4-hydroxpyrrolo[2,3-b]-7-methylquinolin-4-one, dissolved in DMSO, 25 μM; Bleb); DMSO concentration never exceeded 0.5% v/v and the corresponding solvent concentration was added to the untreated condition. Nocodazole, a microtubule destabilizer, was added after 6h from NGF treatment, while blebbistatin, an inhibitor of myosin II, was added 30 min before NGF stimulation.

Cell analysis and tests.

SCs spreading and viability.

SCs were cultured on different substrates placed on the bottom of WillCo-dishes (GWST-3512, WillCo Wells) for different times (3h-96h), under standard cell culture conditions. SCs spreading (3 h) was investigated by bright-field imaging. An inverted microscope Leica DMI 4000 B (Leica Microsystems, Wetzlar, Germany) with 20x objective was used to monitor the cells. We have considered cells as "spread" if they flattened onto the surfaces; spread cells were reported as percentage over the total number of cells per sample. At least 300 cells were analyzed per condition, in three independent experiments (n = 3).

SC cell viability (at 24, 48 and 96h) was measured by the 2-(2-methoxy-4-nitrophenyl)-3-(4-nitrophenyl)-5-(2,4-disulfophenyl)-2H-tetrazolium-monosodium salt (WST-8) assay, according to commercial instructions (Sigma, #96992). SCs were incubated in a 10% WST-8 solution (in medium) in a CO_2 incubator for 3 h. Afterwards, the supernatant was carefully aspirated, transferred to a new plate, and the absorbance of each well was observed by a plate reader at a wavelength of

450 nm. The absorbance of formazan produced was directly proportional to the number of living cells. Data are reported as mean ± SEM; at least three independent experiments ($n \geq 3$) were carried out for each substrate showing consistent results.

PC12 Neurite guidance imaging and analysis.

Living-cell imaging was performed after 24 h from seeding using a Leica CTR 4000 microscope (Leica, Microsystems, Wetzlar, Germany); at least 15 transmission images (40x) were acquired for each sample.

PC12 neurite response to NGs and Flat substrates was quantified by measuring neurite *alignment* along the NG direction, *length* (in μm) and *straightness* (ratio between the distance from the initial and end point of the neurite and its length), at 24 h, in untreated conditions and after drug treatments.
Morphometric data were collected using ImageJ (National Institute of Health, USA). The NG direction was measured as an angle by ImageJ angle tool; FLAT substrates were given a 0 grating angle.

Neurites were semi-automatically segmented (from the point of origin at the perimeter of the cell body to the tip of the neurite growth cone) using NeuronJ, a plugin of ImageJ designed for neurite tracking. The presence of neurites was evaluated and the alignment quantified by measuring the angle of each neurite with the direction of the NG (or with a randomly chosen direction for cells on flat substrate). Only protrusions originating from the cell body and longer than 10 μm (about one average cell body diameter) were counted as neurites. Only neurites which terminated in a free end or with growth cones cleanly abutting neighboring cells were considered. A file containing the tracks was exported and loaded in Matlab (MathWorks) where a custom program calculated the neurite *length* (the distance of the traced neurite path), *straightness* (ratio between the distance from the initial and end point of the neurite and its length) and *alignment* (measured by approximating the neurite as a straight line from the initial to end point and taking the angle of this line versus the NG orientation), for each time point.

It was analyzed at least 300 cells (450 neurites, $n \geq 6$) for each sample in control conditions, while at least 110 cells (180 neurites, $n \geq 3$) for each sample in drug-treated conditions.

PC12 FAs experiments and TIRF microscopy.

PC12 cells were transfected with EGFP-Paxillin construct (gift from Juergen Wehland, Helmholtz Centre for Infection Research, Braunschweig, Germany) by electroporation by Neon transfection system (Thermo Fisher, Waltham Massachusetts, USA). Neuronal differentiation was induced by treatment with NGF, and after 24h (and > 16 h from NGF administration), single PC12 cells adhering to the NGs substrates and to flat control substrates were imaged.

TIRF imaging was performed using an inverted Leica AF6000 microscope with an oil immersion 100x 1.46 NA TIRF objective. For each region, two bright-field (focused on the cell and on the nanostructure), an epifluorescence and a TIRF (depth 150 nm) images were acquired.

For FA analysis, TIRF images were loaded into ImageJ and inverted. FAs were manually drawn using the '*freehand selection*' tool. Then measurements of FA area (in μm^2) and alignment angle versus NG direction were then obtained using the '*measurement*' and '*angle*' tools of ImageJ, respectively. The angle of each FAs was measured with respect to the NG direction choosing the cell soma center as origin; a random reference direction (0°) was chosen for the flat surfaces. FAs were considered *aligned* if the angle is between 0 and 15° and *misaligned* if between 15 and 90°. The number of FAs per cell was also registered. We analyzed at least 30 cells or 400 FAs for each sample, with $n \geq 4$.

PC12 Western blot.

Western blot analysis on PC12 was performed to assess: the activation (phosphorylation) levels of effector proteins in FA pathway, such as focal adhesion kinase (FAK) and proto-oncogene tyrosine-protein kinase Src (SRC); the expression levels of FA proteins talin, zyxin and vinculin; the expression levels of YAP/TAZ, looking at YAP1 level.

PC12 were cultured and NGF-differentiated for 24h on different substrates and lysated on ice by RIPA buffer (Sigma-Aldrich, R0278) containing protease and phosphatase inhibitors cocktail (cOmplete and PhosSTOP, Roche Diagnostics, Basel, Switzerland). Cell lysates were centrifuged (15000 *g* for 15 minutes, 4°C) and then the supernatants were tested for protein concentration by a protein assay kit

(Micro BCA™, Thermo Scientific Pierce). The samples were mixed with Laemmli buffer containing β-mercapto-ethanol (5% final concentration), boiled for 5 minutes, and used for gel electrophoresis (or kept at -80°C).

HN lysates (10 μg/line) were processed by immunoblot. Briefly, samples were resolved by gel electrophoresis (SDS-PAGE) using Gel Criterion XT-Precasted polyacrylamide gel 4-12% Bis-Tris (Biorad), transferred to nitrocellulose membranes by Trans-Blot Turbo transfer system (Biorad) and probed overnight at 4°C with primary antibodies. We used the following antibodies against: FAK (1:1000; Abcam, Cambridge, UK; ab40794) and phospho(Tyr397)-FAK (1:1000; Abcam ab4803); SRC-(pan) (1:1000; Cell Signaling #2123); phospho(Tyr416)-SRC (1:1000; Cell Signaling #2101); talin-pan 1-2 (1:1000; Sigma clone 8D4); zyxin (1:1000; Abcam Ab71842); vinculin (1:1000; Abcam ab18058); YAP (1:1000, Abcam ab39361) and GAPDH (1:3000; Sigma G8795); the antibodies anti-phospho proteins were incubated in BSA 5% buffer, while the others in milk 2%. Membranes, after incubation with the appropriate peroxidase-linked secondary antibodies (goat anti-Rabbit/Mouse IgG-HRP Conjugate, Biorad; 1:2500), were developed by the SuperSignal West Femto (Thermo Scientific Pierce, #34095) or ClarityTM (Biorad, 170-5060) enhanced chemiluminescent (ECL) substrates. The chemiluminescent signal was acquired by ImageQUANT LAS400 scanner (GE Healthcare Life Sciences, Uppsala, Sweden). The density of immunoreactive bands was quantified by ImageJ; the results for pFAK and pSRC were normalized to the total FAK or SRC protein levels while for other proteins to the GAPDH content, and reported in % with respect to T1 levels.

Immunostaining.

SCs were grown for 2 or 7 days on Flat, R_{LD} and R_{HD} rippled PET replicas, then fixed for 15 min in 4% paraformaldehyde in phosphate buffered solution (PBS) at room temperature. SCs were stained with anti-S100 primary antibody (Sigma; 1:200, rabbit) and phalloidin-Alexa Fluor 647 (Lifetech A22287, 1:30; to stain actin fibers) in GDB buffer (0.2% BSA, 0.8 M NaCl, 0.5% Triton X-100, 30×10^{-3} M phosphate buffer, pH 7.4) overnight at 4 °C. Samples were then washed in PBS and incubated with the AlexaFluor 488-conjugated secondary antibody (Invitrogen; 1:150, anti-

rabbit) in GDB for 2 h at room temperature. After washing, samples were mounted using Vectashield mounting medium with DAPI to stain nuclei (Vector Laboratories).

PC12 cells were cultured, fixed for 15 min with 4% formaldehyde with 4% sucrose in PBS at room temperature. Here cells were incubated with primary anti-YAP antibody (1:500, ab36391) and phalloidin-Alexa fluor 647 (1:40, Thermo Fisher A22287) in GDB buffer (0.2% BSA, 0.8 M NaCl, 0.5% Triton X-100, 30 mM phosphate buffer, pH 7.4) overnight at 4 °C and then with appropriate secondary antibody conjugated to AlexaFluor 488; in the end samples were mounted using Fluorashield mounting medium with 4′,6-diamidin-2-fenilindolo (DAPI) to stain nuclei (Sigma, F6057).

Confocal Imaging and Cell Morphological Analysis.

Confocal images were acquired using a laser scanning confocal microscope TCS SP2 (Leica Microsystems, Germany) with a 40 or 63× oil objective by using UV (405 nm) argon (488 and 633 nm) and 375 nm lasers.

All samples were processed in parallel and the images acquired with the same microscope setting. Each reported confocal image was obtained from a *z*-series (stack depth was within 10 μm; steps = 1 μm). The resulting *z*-stack was processed with the ImageJ software (NIH, USA) into a single image using "*z-project*" and "*Max intensity*" options.

In the case of SCs, the confocal images of S100 (specific SC marker) were used to evaluate cellular morphology by ImageJ. Cell contours were drawn with the "*Freehand selection*" tool and processed with the "*Measurement*" tool (with the options "*Area*" and "*Feret's diameter*"). The orientation of the multiscale patterns was measured with the "*Feret Angle*" ImageJ; for Flat substrates, a random direction was chosen.

The measured parameters were: SCs area (μm^2); SC aspect ratio (the ratio between the length of the minor axis and the major axis for the best-fitted ellipse of the cell). SCs alignment angle (angles were calculated as the absolute value of the difference between the orientation angle of the nano-rippled pattern and the cell major axis).

The percentage of SC alignment angles between 0-180° (step: 10 degrees) was evaluated for each different pattern by the "*Frequency distribution*" analysis. At least 300 cells were analyzed per each substrate type, in three independent experiments (n = 3).

For PC12 studies, the confocal images of actin fibers and DAPI staining were used to evaluate *cellular* and *nuclear* YAP localization levels by ImageJ ("*polygon selection*" tool for cell contours, while "*make a binary*" and "*wand tool*" for nucleus contours).

The YAP signal was quantified as follows: the cell or nucleus *region of interest* (ROI) were applied to the correspondent YAP positive images and their intensity were measured by the ImageJ "*Measure*" tool (option "*mean grey value"*). The values were then reported as the nuclear/ cellular ratio; at least 25 cells per each substrate type, in at least three independent experiments (n = 3).

Actin cytoskeleton organization analysis.

SC actin fiber intensity and organization were quantified by analyzing the actin fluorescence signal on phalloidin-647 positive images acquired by confocal fluorescence microscopy.

SC actin content was quantified by measuring the average intensity of the fluorescent actin for each cell: SC area was first manually selected for each cell as a ROI on the S100-positive images; then the ROI was applied the correspondent actin-positive image and the signal intensity was measured by the ImageJ "Measure" tool (option *"mean grey value").* Data were reported as the ratio of the fluorescence intensity of the *perpendicular SCs* (alignment angle ≥ 60° vs. the ripple main direction) over that of the *aligned SC* (alignment angle ≤ 30° vs. the ripple main direction).

Actin intensity for SC protrusion tips was also analyzed, as for SC cells. *Actin* directionality was also analyzed for each SC by the *Directionality* tool of Fiji. This plugin returned a directionality histogram by exploiting image FFT algorithms: isotropic images generate a flat histogram, whereas oriented images give a peaked histogram. These histograms were finally fitted by Gaussian curves that returned two parameters, *dispersion* and *directionality* (the standard deviation and the center

of the Gaussian curve, respectively), the first representing the degree of orientation of the image, the second the direction in which it is oriented (here normalized to the pattern main direction).

At least 30 cells or tips were quantified for each substrate, in three independent experiments (n=3).

SEM Imaging.

SCs were cultured on PET substrates, fixed for 15 min in 4% paraformaldehyde in PBS at room temperature, and then samples were dehydrated with absolute ethanol at different concentrations: 50%, 70%, and 100%. The substrates were then coated with a 5-nm thick gold layer by thermal evaporation.

The metal layer was shorted to the SEM sample holder to allow proper electron discharge during imaging. The substrates were then loaded into a LEO 1525 field emission SEM and image acquisition was carried out by secondary-electron detection with the Everheart-Thornley detector in order to enhance the topography of cell-substrate interfaces.

Statistical analysis.

Data were reported as the average value ± standard error (mean ± SD) or average value ± the standard error of the mean (mean ± SEM), if not differently stated.

For parametric data (after Shapiro-Wilk normality test), Student' t-test (unpaired, two-tailed) or One-way ANOVA (Tukey's multiple comparison test or Dunnett's multiple comparison test) analysis was used to compare data. All the cell experiments were repeated at least three times independently.

Data were statistically analysed by using GraphPad Prism commercial software (GraphPad Prism, 6.05 version). Statistical significance refers to results where $P < 0.05$ was obtained.

6 Future perspectives.

In the previous chapter I have introduced micro- and nanotopographies for neural cells polarization, discussing the potential benefits of their use in the field of regenerative medicine. Although the anisotropic geometries are an important tool to obtain cell contact guidance, the regularity of their geometry can be affected by the biodegradation of the entire scaffold and, consequently, by a progressive loss of the directional signal provided to the cells. Since physiological systems are characterized by the coexistence of overall-ordered structures and local-disorder caused by stochastic alterations in tissue composition, the finest design of an implantable scaffold must also consider this gradual loss in directionality due to topographical deterioration.

*In this chapter, I will introduce a renewed approach to spatially modulate the intensity of the directional stimulus by the use of randomly-distributed nano-modifications (**NMs**) applied to nanogratings, with the final aim to study cell collective response to directionality gradients. I will describe in detail the design and development of this new kind of topographies, that spatially vary from ideal nanogratings to a flat surface. I will finally show some preliminary tests on two biological models: the **MDCK** epithelial cell line, and the human dermal Fibroblast (**HDF**) cell line. These last data were obtained thanks to the collaboration with Dr. Aldo Ferrari, during my visiting period at ETH (Zurich, Switzerland).*

6.1 Introduction.

It is well established that the cell behavior is influenced by geometrical patterns in the micrometric and sub-micrometric range. As enlightened in Chapter 5, the physical shape of anisotropic nanostructures induces alignment or directional growth of cells, the *contact guidance* phenomenon [277]. In all the aforementioned cases, the presence of nanotopography triggers the intensity of the set directional signal, thus leading to an on/off topographical activation. This bistable signal behavior hampers the possibility to explore the cell response to a partial anisotropy. Moreover, ordered micro-/nano-structures coexist, *in vivo*, with some degree of topographical noise due to cellular debris, protein aggregates or scar-tissue invasion.

The group of my PhD supervisor has previously assessed the role of topographical noise on neurite guidance of single PC12 cells [265],[278]. First, they have quantitatively defined the intensity of the directional signal delivered to the cells by the *directionality* parameter, as the average ratio between the signal due to the periodic component and the low-frequency noise. The relative weight of these two components can be easily visualized and quantitatively evaluated by means of the Image Fourier Transform (**FT**) of a given nanopattern, as explained in Meucci *et al.*, 2012 [278]. According to this definition, the *directionality* value is maximum for perfectly periodic nanograting and directionality loss stems from the addition of a random noise to the periodic nanostructure. As the percentage of randomly inserted NMs (the **p** value) increases, the NMs increasingly impact the overall nanogratings organization and reduce the intensity of the peaks in the FT domain meanwhile increasing the low-frequency signal, violating the nanograting perfect periodicity.

Concerning the *contact guidance* phenomenon, differentiating PC12 cells actively respond to the reduction of directionality through the modulation of focal adhesion (**FA**) development. In fact, FA average size decreases with the increase of **p**: this effect mainly inflicts aligned FAs, which progressively become indistinguishable from the misaligned ones. High noise levels inhibit FA spreading, reducing the average size also compared to the flat condition. As expected, neurite straightness is also affected by noise, as extensively discussed in Tonazzini *et al*., 2013 [265]. In general, neurites on nanogratings are straight. Increasing **p** value progressively reduce neurite straightness, down to a threshold behavior.

Overall, *contact guidance* is also a strong regulator of single and collective directional migration, which is established either thorough intrinsic cellular mechanisms or driven by external cues such as chemical gradients (*chemotaxis*) or gradients of substrate stiffness (*durotaxis*). The progressive behavioral response to a stimulus is well-established for both the aforementioned mechanisms, and in some cases a single cell can act differently from the collectivity, as in the case of collective durotaxis, which has recently emerged as a far more efficient mechanism than single-cell durotaxis [279].

In the following section it will be presented the design and fabrication of a new platform of randomly-distributed NMs to obtain spatial gradients of topographical directionality.

6.2 Rational design of noisy topographical gradients.

As suggested by the literature [278], micro- and NGs, alternating lines of grooves and ridges, were taken as reference anisotropic substrates, for which the directionality value is the maximum. Typically, a pattern with reduced directionality can be designed by randomly interfering with the original anisotropic layout. As reference, it was chosen period, duty cycle and depth values of 2 μm, 50% (*i.e.* ridge width = groove width = 1 μm) and 1 μm, respectively. This choice was based on previous studies, where 2 μm-gratings were successfully employed to induce HUVEC endothelialization of targeting substrates [280] and primary HDF migration [281]. The subsequent change in cell phenotype to a fully-polarized shape aligned to the grating lines demonstrated that these anisotropic topographies can determine a valid topographical stimulus for cells *in vitro*. Contrarily, flat surfaces as those present in standard tissue culture Petri dishes have no directionality and were taken as control isotropic substrates.

For a rational NMs design, it was taken advantage of previous studies concerning cell adhesion and FA maturation on nanogratings. It is well known that, in the case of perfect anisotropic substrates, the FA formation is limited to the top of the nanostructures, whereas FA development by ridge bridging (*i.e.* perpendicularly to the main grating orientation) is strongly inhibited [282] [277]. In order to affect the FA maturation dynamics imposed by the unmodified grating, it was chosen to fabricate on the master mold surface one of the two types of published NMs, named *positive* NMs, which is characterized by the presence of a gap-unit along the ridges. After the replica transfer process onto polydimethylsiloxane (PDMS) and COC surfaces, the positive NMs became *negative*, *i.e.* bridges between adjacent ridges .

Consequently, in order to create directionality gradients, it was necessary to define the perfect topography master with the highest directionality, and the so-called "topographical sub-units", as reported in [278]. After it was chosen the 2 μm-grating as master geometry, the grating in two kinds of sub-units was divided: ridge-units defined as 1×1×1 μm^3 blocks, and groove-units defined as empty spaces with the same size. The NMs can be inserted in the master geometry by changing a ridge-units into a groove-units or vice-versa. As previously stated, only one type of

modification was used in this these studies, named *positive nano-modification*, which is characterized by the presence of a ridge-unit along the grooves, resulting in a reduction of the total area available for cell-adhesion on the biocompatible replicas.

With the final aim to randomly distribute NMs in the starting grating geometry, the original algorithm implemented in Matlab by Meucci *et al*. [278] was modified as follows. More in detail, for each established sub-area value, a binary matrix was created, whose elements represented the sub-units of the grating: each matrix element corresponds to the 1×1 μm^2 block. The matrix-element value indicated if the corresponding unit area element was ridge-unit (in this case the value is 1) or groove-unit (in this case the value is 0), as an on/off switch for a directional signal element (**Figure 6.1**.**a**). Then, a subset of these unit elements was selected and a chosen fraction (p) of the sub-unit elements was randomly selected (ranging from 0 to 100%) and swapped. These modified elements represented the NMs. The density of randomly distributed nano-modifications in a master geometry modulated its directionality. Finally, a new complete matrix describing the noisy nanogratings was generated by incorporating the modified subset of unit elements to the starting matrix.

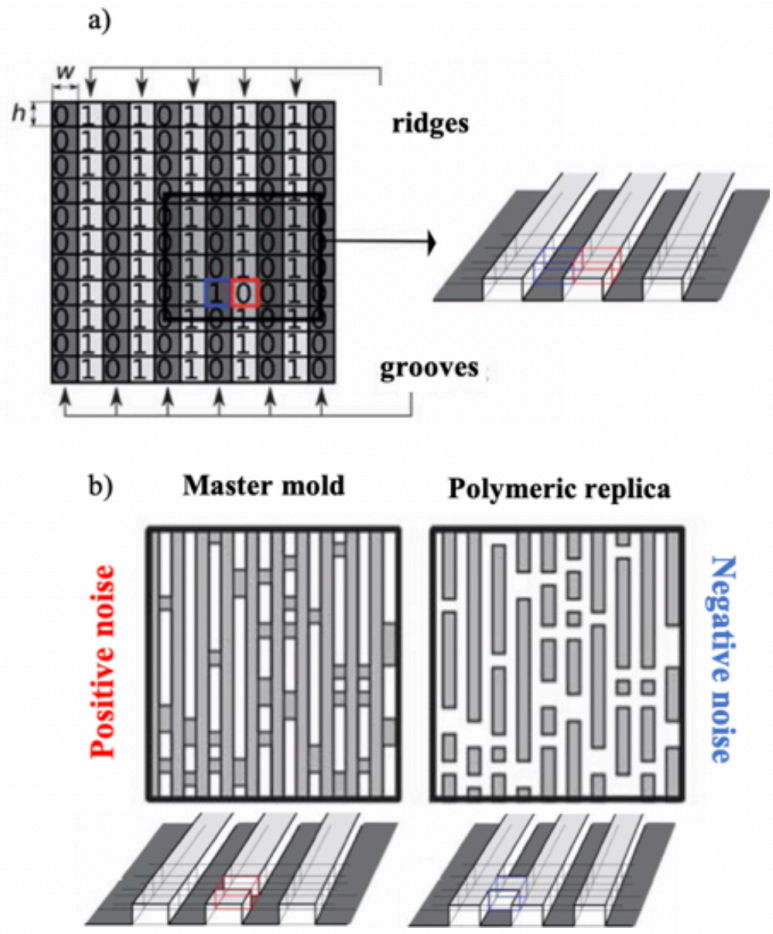

Figure 6.1 **Nanotopographical noise generation: NMs are applied to nanogratings.** a) Binary matrix representing the gratings during the pattern generation process. Each element of the matrix corresponds to a unit element ($w \times h$) of the nanograting. For the present study, I chose $w=h=1$ μm. The value of the matrix element determines the type of surface: 1 for ridges, 0 for grooves. The red and blue squares represent the NMs on the master mold: the change is from a ridge-type unit to a groove-type unit. b) After Matlab program translated the modified matrices into CAD files, it was possible to obtain a master mold with a fixed value of **p** for the positive noise. Finally, the complementary of this geometry is transferred onto the polymeric biocompatible materials (COC, PDMS) by means of replica processes. The figure is adapted from [278].

A DXF file (AutoCAD, Autodesk, USA) containing the final design of the noisy topography was produced by a custom-made Matlab script (MathWorks, USA) [265], [278]. Each pattern was described by the probability **p** of a modification-event (*i.e.* the insertion of a NMs). This process is very versatile, since the Matlab script works in a parametric way, allowing for an easy variation of the final geometry in

terms of patterned area, grating-periodicity, relative size of the ridge- and groove-units and, above all, the **p** value.

In order to test the single-cell response to a topographical gradient, two types of gradient geometries were fabricated, that were supposed to act on single cells, composed by smaller areas of 50 x 50 μm^2 and 30 x 30 μm^2, (comparable with typical fibroblast [281] and epithelial cell areas [283]), for a total gradient area of 50 x 550 μm^2 or 30 x 330 μm^2, respectively. The anisotropic signal was progressively lost in space by adding an increasing degree of nanotopographical noise. In particular, the single areas at constant p were manually arranged alongside following crescent p values by the use of KLayout CAD software, avoiding single-area superimposition. **Figure 6.2 a** shows a sketch of a single cell-directionality gradient, starting from a perfect grating of 2 μm in periodicity, with a **p** value of 0%, down to flat surface, with a **p** value of 100% and 10% of difference in **p** between two contiguous areas.

In the second type of patterned substrates, larger areas (1 cm x 454 μm) with a fixed degree of noise (p) were designed and arrange alongside with the final aim to create what it was called "*mirrored gradient topography*" for collective migration studies. In fact, the topographic gradient is extended along the two sides of the perfect anisotropic grating of 1 cm x 900 μm area, for a total patterned area of 1 cm^2.

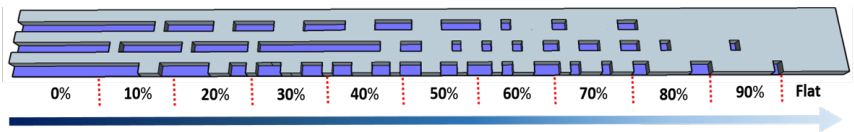

Figure 6.2 **Schematic representation of topographical-directionality gradient on silicon mold:** the single-cell gradient is composed by 11 different percentages of noise starting from a 2 μm-periodical NGs down to the Flat control topography.

6.3 Fabrication of the noisy topographical gradients on silicon wafers.

Two sets of silicon molds with p value varying from 0 to 100 % were fabricated according to the protocol described in the ***Materials and Methods*** section. In particular, the molds named "50-30" contain single-cell directionality gradients (20 areas of 50 x 550 μm^2, 17 areas of 30 x 330 μm^2), while the other set of molds contains 14 "1 cm^2" directionality gradients. After, the fabrication of a chromium mask on Soda-Lime patterned by laser writing technique, the gradient areas were exposed

on a thick layer of AZ 1500 positive photoresist by photolithography. Then, the topography was finally transferred on silicon by RIE etching technique. The processing was already optimized in order to obtain an etching depth of the order of 1 μm.

All the gradients were finally replicated both in PDMS and in COC, according to soft lithography techniques already described in Chapter 2. The replica processes were typically fast: in PDMS case for 1 h and 30 minutes at 100°C, in the case of COC 10 minutes at 160–180 °C and 50 bar before cooling down to 40°C for a full replica molding. In this work, PDMS and COC were chosen because of their biocompatibility and optical properties, which make them particularly suitable for long-term, fluorescence microscopy with living cells [187], [253]. A representative image of a silicon master mold after the RIE process is depicted in **Figure 6.3 a**; in **Figure 6.3 b** and **c** high-magnification SEM images show areas of the 0% (the perfect anisotropic grating) and the 30% positive noise area on the mirrored gradient topography. Despite the round-shape of the angles, the dimension of the NMs was maintained with respect to the ones set on the CAD files. To be sure that the samples could be easily detached from the master mold, the silicon was silanized before the replica processes.

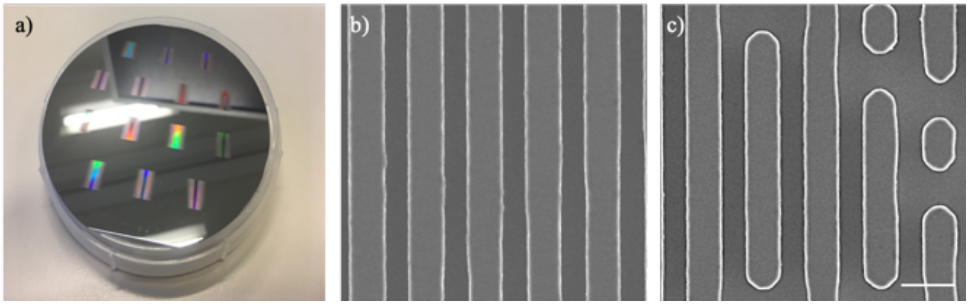

Figure 6.3 **Fabricated topographical-directionality gradient:** Image of a silicon wafer containing 14 "1 cm^2 mirrored gradient topography" a). Each of the cm^2 patterned area is composed by 11 different percentages of noise starting from a 2 μm-periodical NGs down to the Flat control topography, where the topographic gradient is extended along the two sides of the perfect anisotropic grating. b) and c): high-magnification SEM images of 0% and 30% noise areas. Scale bar: 1 μm.

By the use of soft lithography techniques, the noisy gradients were replicated on two different biocompatible materials (PDMS and COC), and tested them with primary HDF and epithelial Madin-Darby canine kidney MDCK cell line. In **Figure**

6.4 a the polymeric mirrored gradient topography is schematically represented, and **Figure 6.4 b** shows an optical image of PDMS replicas of a 70% noise area on the mirrored gradient topography. Notably, the uniformity of the patterns was preserved for the whole 1 cm^2 area.

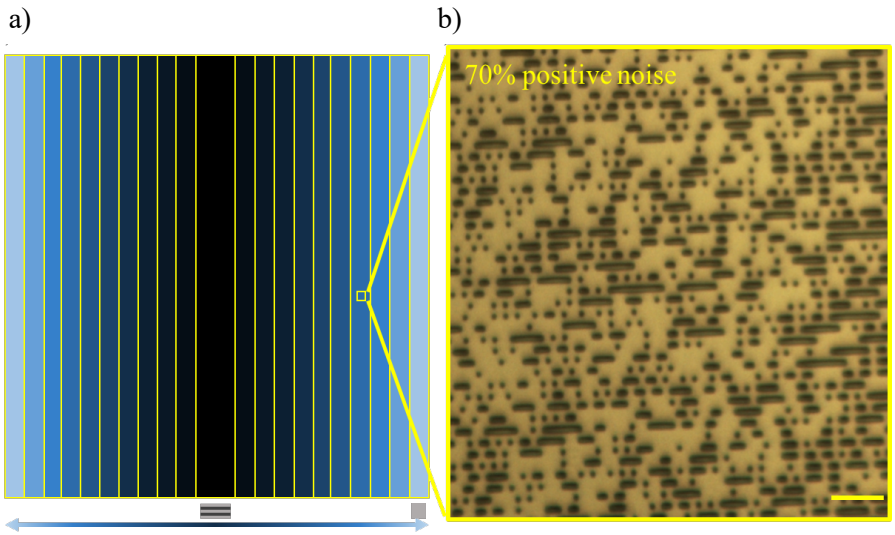

Figure 6.4 **Mirrored gradient topography.** Schematic representation of the mirrored gradient topography (a) and representative microscopy image of a PDMS replica detail where the noise is 70% (b). Scale bar: 10 µm.

6.4 Single-cell studies

Preliminary *in vitro* tests were made with two different cell lines seeded at low density ($5*10^3$ cells·cm^{-2}): MDCK (EGFP-nuclei stained) and HDF (far-red siRNA nuclei stained). Those cell lines are known to act using a different behavior: while MDCK single-cell motility is influenced by neighboring cells and the formation of the tight junctions, HDF cells behave more independently [281]. As well known in literature, HDF and MDCK have a critical contribution to skin wound healing, but normally the epithelial cells grow in confluent monolayers, while fibroblast do not form connected monolayers and migrate following individual migratory pathways [281], [283]*[281], [283].*

Since the replica processes of the directionality gradient were optimized for two different biocompatible materials, the cell behavior of both cell lines was evaluated on flat surfaces of PDMS and COC. Both cell lines were seeded on Flat COC and Flat PDMS replicas with the final goal of evaluating cell speed and track

straightness on both materials for 24 h, as shown in **Figure 6.4**. For the quantification of cell migration, time lapses were acquired and analyzed using the particle tracking algorithm of Imaris (Bitplane Scientific Software, Switzerland): the fluorescent channels corresponding to cell nuclei (the red channel for HDF, marked with silicon rhodamine fluorophore and the green channel for MDCK, marked with EGFP molecule). were contrast-enhanced and an autoregressive motion model was applied (average particle diameter 20 μm, maximal displacement between two consecutive frames 40 μm). Only detected tracks lasting for more than 360 min were considered for migration analysis.

By the use of the *Automatic Tracking* tool, it is possible to link consecutive time points, resulting in a colored *Track*, defined as the motion path of a single object over time. Values for cell speed (the instantaneous speed of the nuclei between two consecutive time points) and track straightness (defined as the ratio between the cell track displacement and cell track length) were obtained automatically using the Imaris measurement tool. Thanks to this analysis, it was confirmed that cell motility was not influenced by the material, for both cell lines, as in [280], [281], and their motion was not influenced by the different nuclei staining on the two different materials.

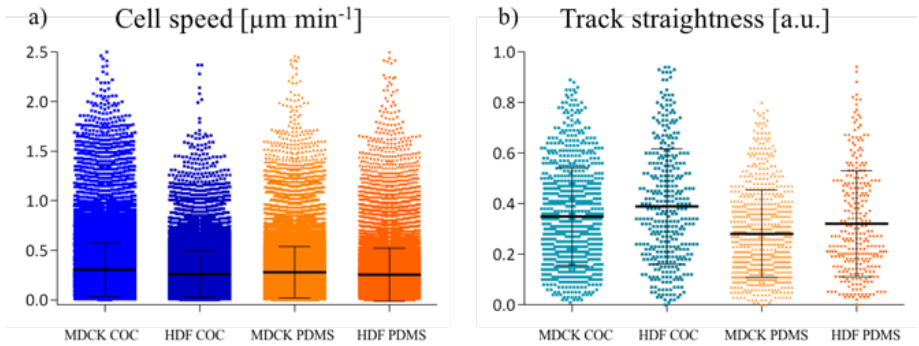

Figure 6.5 **Cell motility parameters**. a) Cell speed and b) track straightness values of MDCK and HDF seeded on Flat PDMS and COC replicas. Data sets are reported as mean ± SD.

Thanks to the comparison between the cell motility on these two different materials, we decided to choose PDMS instead of COC for the following experiment due to the easiness of the fabrication process.

After the fabrication and characterization of silicon molds and replicas, I have started to test the topographical-directionality gradients with time lapse

experiments lasting for 24 h, with the final aim to evaluate the motion of single cells in terms of direction, speed and straightness. At a glance, MDCKII and HDF seeded on top of perfect grating preserved the alignment angle during the whole acquisition time, while cells seeded on the higher percentage of noise seem to have a random walk, likewise a flat condition. Further studies will quantitatively clarify cell motility behavior on those topographical-directionality gradients, at single cell level and as collective motion, in order to compare contact guidance with durotaxis phenomenon.

6.5 Conclusions.

In conclusion, I designed, fabricated, characterized and started to validate two types of original topographical gradients of directionality made with nanotopographies. Starting from fully ordered nanogratings, substrate directionality was gradually reduced by adding a controlled density of nano-modifications, the *positive* type of noise, consisting in the introduction of gaps along the ridges of perfect 2 μm-period gratings.

I fabricated two types of single-cell gradient, composed by smaller areas comparable to that of a typical fibroblast or epithelial cell, so that the anisotropic signal is progressively lost in space by adding an increasing degree of nanotopographical noise.

With the final aim to create a topographical gradient for collective migration studies, I designed a total patterned area of 1 cm^2, the "*mirrored gradient topography*". The noisy gradients were then transferred to biocompatible polydimethylsiloxane (PDMS) and COC foils by photolithography process first and then by soft lithography techniques, and the positive NMs became *negative*, *i.e.* bridges between adjacent ridges. The silicon master molds were further characterized by SEM imaging, and the polymeric replica by optical microscopy.

Regarding the preliminary *in vitro* results, the cell behavior of both cell lines was evaluated on the flat surfaces of two different biocompatible materials, PDMS and COC. Values for cell speed (the speed of the nuclei between two time-points) and track straightness (defined as the ratio between the cell track displacement and cell track length) were obtained automatically using the Imaris measurement tool.

Thanks to this analysis, it was found that cell motility is not influenced by the material, for both cell lines.

Altogether, this Chapter presents a novel and promising approach for the design and realization of biocompatible textured substrates, which can be a model for the degree of topographical noise due to an *in vivo* scaffold degradation of a perfect nanograting. More in general, future results may provide a better understanding of *the* cell–environment interaction.

.

6.6 Materials and Methods.

Fabrication processes.

Silicon molds.

Noisy geometries were generated by a custom Matlab program (adapted from [278]), transferred first on a UV-litho Sodalime and cromium mask by laser-writing, then on silicon wafers by UV lithography and Reactive Ion Etching (RIE). Each wafer, after the adhesive HDMS coating, is spin-coated with AZ1505 resist (Microchemicals GmbH, Ulm, Germany) at 4000 rpm for 40 s, then backed at 110°C for 1 minute in order to create a thick film and processed by UV lithography to generate a noisy pattern.

The molds were finally silanized (Silanization solution: dimethyldichlorosilane in heptane, Fluka, Sigma-Aldrich, USA) in order to obtain low-energy surfaces. In detail, the samples are dipped in the silanization solution for 15 min, then rinsed in hexane (15 min), and finally in 1-octanole (15 min). This step favored master-replica separation after imprint and improved the fidelity and reproducibility of the process.

PDMS and COC replicas.

Topographical-directionality gradients were replicated on PDMS surfaces by mixing the prepolymer and the curing agent at a ratio of 10:1, pouring it into the microstructured mold, degassing to remove air bubbles, and baking at 100 °C for 1 h and 30 minutes. The replica was cut with a scalpel and removed from the master mold.

The topographical-directionality gradients were also imprinted on 180 μm-thick COC foils (Ibidi, Germany) using NIL: COC substrates were placed on top of the mold and softened by raising temperature up to 160–180 °C. A pressure of 50 bar was then applied for 10 minutes before cooling down to 40 °C. Finally, the pressure was released and the mold was detached from the substrate with a scalpel. Samples were then treated with oxygen plasma (100 W for 30 seconds) to increase the hydrophilicity of the surface and to promote cell adhesion.

Cell cultures.

All experiments with HDF and MDCK II cells were performed using cells and media as previously described [281], [283], [284].

Live-Cell Microscopy and Image analysis.

Cell migration movies were acquired using an inverted Nikon-Ti wide-field microscope (Nikon, Japan) equipped with an Orca R-2 CCD camera (Hamamatsu Photonics, Japan) and an incubation chamber (Life Imaging Services, Switzerland) to control temperature, CO2, and humidity. Images were collected using a 20×, 0.45 NA long-distance objective (Plan Fluor, Nikon).

For the quantification of cell migration, time lapses were analyzed using the particle tracking algorithm of Imaris (Bitplane Scientific Software, Switzerland). The fluorescent channels corresponding to the cell nuclei were contrast-enhanced and an autoregressive motion model was applied (average particle diameter 20 μm, maximal displacement between two consecutive frames4 μm). Only detected tracks lasting for more than 24 h where considered for migration analysis. Values for cell speed, track straightness were obtained using the Imaris measurement tool, as explained in [285].

7 Concluding remarks.

In this thesis I presented results on nanofabrication techniques and materials for mechanotransduction studies and tissue engineering applications. My work was focused on the development and subsequent use of innovative biomaterials and nanoimprint lithography processes for biomedical applications. This chapter contains a summary of my results and my conclusions.

I have extensively described the importance of engineered polymers for regenerative medicine applications, by detailing fabrication techniques, mechanotransduction processes, peripheral nerve regeneration process and neural scaffolds technologies, focusing on nanostructured scaffolds (**Chapter 2**).

The first topic I focused on was the use of novel materials for biomedical applications (**Chapter 3)**. The first example was microfluidic phantoms, which have demonstrated to meet the requirements for photoacoustic imaging applications by modelling the vascularized structure of tissues. By simply adding titanium dioxide and black India ink to the PDMS mixture, those phantoms were tuned in order to resemble more closely the biological tissues. In addition, the multi-responsive hydrogels fabricated by iCVD here proposed performed their dynamic swelling response to aqueous environments and in response to UV light. I have tested the hydrogel biocompatibility, ensuring that the reversible stimuli responsiveness of the material is not cytotoxic and can definitely be used for biotechnology, light-controlled cell growth, or light-controlled drug delivery.

As second topic, I presented the use of high-resolution *intermediate molds* for nanoimprint lithography (NIL) (**Chapter 4**). First, I showed the optimization and use an innovative nanoimprint lithography process based on the use of a perfluoropolyether (PFPE) intermediate mold for NIL. In particular, I demonstrated that PFPE intermediate molds enhance resolution and fidelity of the replica process.

An insight over the applicability of PFPE intermediate mold process is contained in **Chapter 5**, where I described the response mechanisms of neuronal cells to nanotopographies. I detailed the fabrication of transparent and biocompatible Cyclic Olefin Copolymer (COC) and polyethylene terephthalate (PET) scaffolds patterned with two new types of nanostructures: nanoripples and ultra-small nanogratings.

First, I have tested PET nanoripples with Schwann cells, to investigate their successful application as neural scaffolds. In this case I used COC as mold to transfer hierarchical nanoripples on PET foils. Then, I have fabricated COC gratings with sub-100 nm periodicity and tested them with NGF-differentiating PC12 cells, as neuronal model.

I believe that such devices, known in literature for polarizing cell bodies and migration, could lead to interesting applications for tissue regeneration applications.

Preliminary results on topographical gradients of directionality were presented in **Chapter 6**. In particular, I here have included also experiments performed at ETH, Zurich, as visiting PhD student. I have designed and fabricated micropatterned structures where the anisotropic signal of the grating was progressively lost in space by adding a controlled increasing degree of noise. Then, I have studied human dermal fibroblast (HDF) and epithelial cell (MDCK) motility on poly(dimethyl siloxane) (PDMS) replicas of the topographical gradients. Further experiments are ongoing on these substrates to understand tissue repair mechanisms, as well as gather information about cell migration during development or cancer invasion.

In conclusion, during my Ph. D. I designed, fabricated and tested micro- and nanostructured scaffolds for biomedical applications. I worked in collaboration with researchers with disparate expertise (*i.e.* physicists, biologists, clinicians), trying to achieve an efficient technology translation from research towards the final clinical use.

Concerning the intermediate mold technique, this fabrication method can be further employed not only for thermal NIL but also for solvent casting and other soft lithography techniques, choosing the appropriate material in function of the feature size to be replicated (< 500 nm in PDMS, > 500 nm in PFPE).

Overall, the micro- and nanofabrication techniques skills I have acquired during my Ph.D. research activity will be likely exploited for the fabrication of novel large-area silicon molds having anisotropic nanostructures on surfaces, with minimum and maximal lateral size in the range 100-1000 nm, and up to 10 μm.

One of the future challenges will be the choice of geometries, to compare the well-established grating layout and a novel zig-zag-ridge pattern. In the latter case, several angles (between 0° and 45°) and segment lengths will be tested. This novel design may allow the re-growing nerve fibers to be more resistant to the mechanical stress stemming from limb movements.

Another critical issue to be addressed will be the transfer of micro- and nanostructures onto new FDA-approved biodegradable materials, such as chitosan, PLA, PCL and the PLA/PCL blend. Indeed, all of those polymeric materials bear optimal mechanical properties to support nerve regeneration.

It was recently demonstrated that chitosan nerve guides supplied with a longitudinal chitosan film successfully reconstructed 15 mm sciatic nerve defects in adult healthy and diabetic rats.

After a thorough characterization of mechanical strength, degradation time and residue product release *in vitro* of the produced scaffolds, a pivotal step forward will be their *in vivo* assays.

I do believe that these devices have the potential to achieve clinical translation in a medium time, contributing to the improvement of biomedical technologies.

8 List of publications.

- Ilaria Tonazzini*, **Cecilia Masciullo***, Eleonora Savi, Agnese Sonato, Filippo Romanato, Marco Cecchini *Neuronal contact guidance and YAP/TAZ signaling on ultra-small nanogratings*, **2019** (submitted);
- Ilaria Tonazzini, Geeske M. Van Woerden, **Cecilia Masciullo**, Edwin Mientjes, Ype Elgersma, Marco Cecchini *Ubiquitin ligase E3a role in polarized contact guidance: rescue strategies in (Ube3a)-deficient hippocampal neurons*, **2019** (submitted);
- **Cecilia Masciullo**, Agnese Sonato, Filippo Romanato, Marco Cecchini *Perfluoropolyether (PFPE) intermediate molds for thermal nanoimprint lithography* Nanomaterials 08/**2018**, 8(8), 609, DOI: 10.3390/nano8080609;
- **Cecilia Masciullo***, Rossana Dell'Anna*, Ilaria Tonazzini, Roman Böttger, Giancarlo Pepponi, Marco Cecchini *Hierarchical thermoplastic rippled nanostructures regulate Schwann Cell adhesion, morphology and spatial organization.* Nanoscale; 09/**2017**; 9(39) 14861-14874, DOI: 10.1039/C7NR02822A;
- Rossana Dell'Anna*, **Cecilia Masciullo***, Erica Iacob, Mario Barozzi, Damiano Giubertoni, Roman Bottger, Marco Cecchini, Giancarlo Pepponi *Multiscale Structured Germanium Nanoripples as Templates for Bioactive Surfaces.* RSC Advances 01/**2017**; 7(15):2094., DOI:10.1039/c6ra28531g;
- Katrin Unger, Paul Salzmann, **Cecilia Masciullo**, Marco Cecchini, Georg Koller, Anna Maria Coclite *Novel light-responsive biocompatible hydrogels produced by initiated Chemical Vapor Deposition.* ACS Applied Materials & Interfaces 05/**2017**, DOI:10.1021/acsami.7b01527
- Cinzia Avigo, Paolo Armanetti, **Cecilia Masciullo**, Nicole Di Lascio, Lucia Cavigli, Fulvio Ratto, Roberto Pini, Marco Cecchini, Claudia Kusmic, Francesco Faita, Luca *Menichetti Novel organosilicon phantoms as testing material for photoacoustic imaging* 03/**2016** Design and Quality for Biomedical Technologies IX 9700, 97000I;
- Cinzia Avigo, Nicole Di Lascio, Paolo Armanetti, Claudia Kusmic, Lucia Cavigli, Fulvio Ratto, Sandro Meucci, **Cecilia Masciullo**, Marco Cecchini, Roberto Pini, Francesco Faita, Luca Menichetti *Organosilicon phantom for photoacoustic imaging*. Journal of Biomedical Optics 04/**2015**; 20(4):46008., DOI:10.1117/1.JBO.20.4.046008.

9 List of acronyms.

10 Bibliography.

[1] X. M. Zhao, "Soft lithographic methods for nano-fabrication," *J. Mater. Chem.*, vol. 7, no. 7, pp. 1069–1074, 1997.

[2] F. Cerrina and C. Marrian, "A Path to Nanolithography," *MRS Bull.*, 1996.

[3] C. Acikgoz, M. A. Hempenius, J. Huskens, and G. J. Vancso, "Polymers in conventional and alternative lithography for the fabrication of nanostructures," *Eur. Polym. J.*, vol. 47, no. 11, pp. 2033–2052, 2011.

[4] A. Biswas, I. S. Bayer, A. S. Biris, T. Wang, E. Dervishi, and F. Faupel, "Advances in top-down and bottom-up surface nanofabrication: Techniques, applications & future prospects," *Adv. Colloid Interface Sci.*, vol. 170, no. 1–2, pp. 2–27, 2012.

[5] B. D. Gates, Q. Xu, M. Stewart, D. Ryan, C. G. Willson, and G. M. Whitesides, "New approaches to nanofabrication: Molding, printing, and other techniques," *Chemical Reviews*. 2005.

[6] B. Kwon and J. H. Kim, "Importance of Molds for Nanoimprint Lithography: Hard, Soft, and Hybrid Molds," *J. Nanosci.*, 2016.

[7] Y. Xia and G. M. Whitesides, "Soft Lithography," *Annu. Rev. Mater. Sci.*, vol. 28, no. 1, pp. 153–184, 1998.

[8] J. A. Rogers and R. G. Nuzzo, "Recent progress in soft lithography," *Mater. Today*, vol. 8, no. 2, pp. 50–56, 2005.

[9] A. Kumar and G. M. Whitesides, "Features of gold having micrometer to centimeter dimensions can be formed through a combination of stamping with an elastomeric stamp and an alkanethiol 'ink' followed by chemical etching," *Appl. Phys. Lett.*, vol. 63, no. 14, pp. 2002–2004, 1993.

[10] X. Younan *et al.*, "Replica molding using polymeric materials: A practical step toward nanomanufacturing," *Adv. Mater.*, vol. 9, no. 2, pp. 147–149, 2004.

[11] D. Qin, Y. Xia, and G. M. Whitesides, "Soft lithography for micro- and nanoscale patterning," *Nat. Protoc.*, vol. 5, no. 3, pp. 491–502, 2010.

[12] R. Paolesse *et al.*, "Encyclopedia of Nanoscience and Nanotechnology," *J. Am. Chem. Soc.*, 2010.

[13] Y. Xia, E. Kim, X.-M. Zhao, J. A. Rogers, M. Prentiss, and G. M. Whitesides, "Complex Optical Surfaces Formed by Replica Molding Against Elastomeric Masters," *Science (80-.).*, vol. 273, no. 5273, p. 347 LP-349, Jul. 1996.

[14] A. Tourovskaia, X. Figueroa-Masot, and A. Folch, "Long-term microfluidic cultures of myotube microarrays for high-throughput focal stimulation," *Nat. Protoc.*, vol. 1, p. 1092, Aug. 2006.

[15] J. W. Park, B. Vahidi, A. M. Taylor, S. W. Rhee, and N. L. Jeon, "Microfluidic culture platform for neuroscience research," *Nat. Protoc.*, vol. 1, p. 2128, Dec. 2006.

[16] A. L. Paguirigan and D. J. Beebe, "Protocol for the fabrication of enzymatically crosslinked gelatin microchannels for microfluidic cell culture," *Nat. Protoc.*, 2007.

[17] A. Bietsch and B. Michel, "Conformal contact and pattern stability of stamps used for soft lithography," *J. Appl. Phys.*, 2000.

[18] C. Y. Hui, A. Jagota, Y. Y. Lin, and E. J. Kramer, "Constraints on microcontact printing imposed by stamp deformation," *Langmuir*, 2002.

[19] D. Emmanuel, S. Heinz, M. Bruno, and B. Hans, "Stability of molded polydimethylsiloxane microstructures," *Adv. Mater.*, vol. 9, no. 9, pp. 741–746, 2004.

[20] Y. Xia, E. Kim, and G. M. Whitesides, "Micromolding of Polymers in Capillaries: Applications in Microfabrication," *Chem. Mater.*, vol. 8, no. 7, pp. 1558–1567, Jan. 1996.

[21] Y. Xia and G. M. Whitesides, "Soft Lithography," *Angew. Chemie Int. Ed.*, 1998.

[22] D. C. Duffy, J. C. McDonald, O. J. A. Schueller, and G. M. Whitesides, "Rapid Prototyping of Microfluidic Systems in Poly(dimethylsiloxane)," *Anal. Chem.*, vol. 70, no. 23, pp. 4974–4984, Dec. 1998.

[23] C. N. Lafratta, "(12) United States Patent (45) Date of Patent :," vol. 2, no. 12, 2014.

[24] J. J. Dumond and H. Yee Low, "Recent developments and design challenges in continuous roller micro- and nanoimprinting," *J. Vac. Sci. Technol. B*, vol. 30, no. 1, p. 10801, Dec. 2011.

[25] L. Peng, Y. Deng, P. Yi, and X. Lai, "Micro hot embossing of thermoplastic polymers: A review," *J. Micromechanics Microengineering*, vol. 24, no. 1, 2014.

[26] M. Worgull, J.-F. Hétu, K. K. Kabanemi, and M. Heckele, "Hot embossing of microstructures: characterization of friction during demolding," *Microsyst. Technol.*, vol. 14, no. 6, pp. 767–773, 2008.

[27] M. Worgull, A. Kolew, M. Heilig, M. Schneider, H. Dinglreiter, and B. Rapp, "Hot Embossing of High Performance Polymers," *Microsyst. Technol.*, vol.

17, no. 4, pp. 585–592, Apr. 2011.

[28] S. Lan *et al.*, "Experimental and numerical study on the viscoelastic property of polycarbonate near glass transition temperature for micro thermal imprint process," *Mater. Des.*, vol. 30, no. 9, pp. 3879–3884, 2009.

[29] L. J. Guo, "Recent progress in nanoimprint technology and its applications," *J. Phys. D. Appl. Phys.*, vol. 37, no. 11, pp. 123–141, 2004.

[30] M. Rubinstein and R. H. Colby, "Polymer physics," *Polymer International*. 2003.

[31] M. Benhamou, "Polymer Viscoelasticity – Basics, Molecular Theories, Experiments and Simulations, 2nd edn, by Yn-Hwang Lin," *Contemp. Phys.*, vol. 53, no. 6, p. 524, 2012.

[32] "Jenoptik Mikrotechnik GmbH," *https://www.jenoptik.com*. [Online]. Available: https://www.jenoptik.com.

[33] "Wickert Press," *http://www.wickert-presstech.de*. [Online]. Available: http://www.wickert-presstech.de.

[34] "EVGroup," *https://www.evgroup.com/en*. [Online]. Available: https://www.evgroup.com/en.

[35] "SUSS MicroTec," *https://www.suss.com/en*. [Online]. Available: https://www.suss.com/en.

[36] "Karlsruhe Institute of Technology (KIT)," *https://www.kit.edu/english/*. [Online]. Available: https://www.kit.edu/english/.

[37] "Obducat AB," *http://www.obducat.com*. [Online]. Available: http://www.obducat.com.

[38] F. Lazzarino, C. Gourgon, P. Schiavone, and C. Perret, "Mold deformation in nanoimprint lithography," *J. Vac. Sci. Technol. B Microelectron. Nanom. Struct. Process. Meas. Phenom.*, vol. 22, no. 6, pp. 3318–3322, 2004.

[39] B. Heidari, I. Maximov, and L. Montelius, "Nanoimprint lithography at the 6 in. wafer scale," *J. Vac. Sci. Technol. B Microelectron. Nanom. Struct. Process. Meas. Phenom.*, vol. 18, no. 6, pp. 3557–3560, 2000.

[40] M. E. Dirckx and D. E. Hardt, "Analysis and characterization of demolding of hot embossed polymer microstructures," *J. Micromechanics Microengineering*, vol. 21, no. 8, p. 085024, Aug. 2011.

[41] H. Taylor, D. Boning, and C. Iliescu, "A razor-blade test of the demolding energy in a thermoplastic embossing process," *J. Micromechanics Microengineering*, 2011.

[42] P. Nagarajan and D. Yao, “Rubber-assisted micro forming of polymer thin films,” *Microsyst. Technol.*, 2009.

[43] P. Nagarajan and D. Yao, “Uniform shell patterning using rubber-assisted hot embossing process. II. Process analysis,” *Polym. Eng. Sci.*, 2011.

[44] H. Mekaru, O. Nakamura, O. Maruyama, R. Maeda, and T. Hattori, “Development of precision transfer technology of atmospheric hot embossing by ultrasonic vibration,” *Microsyst. Technol.*, 2007.

[45] W. K. Schomburg, K. Burlage, and C. Gerhardy, “Ultrasonic hot embossing,” *Micromachines*, 2011.

[46] H. Hocheng, T. T. Wen, and S. Y. Yang, “Replication of microlens arrays by gas-assisted hot embossing,” *Mater. Manuf. Process.*, 2008.

[47] J. T. Wu, S. Y. Yang, W. C. Deng, and W. Y. Chang, “A novel fabrication of polymer film with tapered sub-wavelength structures for anti-reflection,” *Microelectron. Eng.*, 2010.

[48] H.-D. Kim, G.-W. Yoon, J. Yeon, J.-H. Lee, and J.-B. Yoon, “Fabrication of a uniform microlens array over a large area using self-aligned diffuser lithography (SADL),” *J. Micromechanics Microengineering*, vol. 22, no. 4, p. 045002, Apr. 2012.

[49] J. J. Dumond and H. Yee Low, “Recent developments and design challenges in continuous roller micro- and nanoimprinting,” *J. Vac. Sci. Technol. B, Nanotechnol. Microelectron. Mater. Process. Meas. Phenom.*, vol. 30, no. 1, p. 010801, Jan. 2012.

[50] A. S. Hyun and G. L. Jay, “High-Speed Roll-to-Roll Nanoimprint Lithography on Flexible Plastic Substrates,” *Adv. Mater.*, vol. 20, no. 11, pp. 2044–2049.

[51] D. Yun *et al.*, “Development of roll-to-roll hot embossing system with induction heater for micro fabrication,” *Review of Scientific Instruments*. 2012.

[52] D. Yun, J. Kim, M. Kim, D. Kim, and J. Kwon, “Impact Print-Type Hot Embossing Process Technology,” vol. 1800386, pp. 1–5, 2018.

[53] S. Y. Chou, P. R. Krauss, and P. J. Renstrom, “Imprint Lithography with 25-Nanometer Resolution,” *Science (80-.).*, vol. 272, no. 5258, p. 85 LP-87, Apr. 1996.

[54] Y. Chen, “Applications of nanoimprint lithography/hot embossing: a review,” *Appl. Phys. A Mater. Sci. Process.*, vol. 121, no. 2, pp. 451–465, 2015.

[55] M. Schvartzman and S. J. Wind, “Robust pattern transfer of nanoimprinted features for sub-5-nm fabrication,” *Nano Lett.*, vol. 9, no. 10, pp. 3629–3634,

2009.

[56] L. J. Guo, "Nanoimprint lithography: Methods and material requirements," *Adv. Mater.*, 2007.

[57] T. A. L., S. M. A., G. M. R., and R. R. S., "Bond–Detach Lithography: A Method for Micro/Nanolithography by Precision PDMS Patterning," *Small*, vol. 3, no. 1, pp. 132–138, 2006.

[58] D. R. Barbero *et al.*, "High resolution nanoimprinting with a robust and reusable polymer mold," *Adv. Funct. Mater.*, vol. 17, no. 14, pp. 2419–2425, 2018.

[59] D. N. Weiss, S. T. Meyers, and D. A. Keszler, "All-inorganic thermal nanoimprint process," *J. Vac. Sci. Technol. B, Nanotechnol. Microelectron. Mater. Process. Meas. Phenom.*, 2010.

[60] R. Dell'Anna *et al.*, "Multiscale structured germanium nanoripples as templates for bioactive surfaces," *RSC Adv.*, vol. 7, no. 15, pp. 9024–9030, 2017.

[61] C. Masciullo, R. Dell'Anna, I. Tonazzini, R. Böettger, G. Pepponi, and M. Cecchini, "Hierarchical thermoplastic rippled nanostructures regulate Schwann cell adhesion, morphology and spatial organization," *Nanoscale*, vol. 9, no. 39, pp. 14861–14874, 2017.

[62] H. Schift, S. Saxer, S. Park, C. Padeste, U. Pieles, and J. Gobrecht, "Controlled co-evaporation of silanes for nanoimprint stamps," in *Nanotechnology*, 2005.

[63] M. D. Austin *et al.*, "Fabrication of 5 nm linewidth and 14 nm pitch features by nanoimprint lithography," *Appl. Phys. Lett.*, 2004.

[64] M. Bender, M. Otto, B. Hadam, B. Vratzov, B. Spangenberg, and H. Kurz, "Fabrication of nanostructures using a UV-based imprint technique," *Microelectron. Eng.*, 2000.

[65] J. Thomas, P. Gangopadhyay, E. Araci, R. A. Norwood, and N. Peyghambarian, "Nanoimprinting by melt processing: An easy technique to fabricate versatile nanostructures," *Adv. Mater.*, vol. 23, no. 41, pp. 4782–4787, 2011.

[66] A. del Campo and E. Arzt, "Fabrication approaches for generating complex micro- and nanopatterns on polymeric surfaces," *Chemical Reviews*. 2008.

[67] A. F. Materials and U. M. Institut, "Materials and anti-adhesive issues in UV-NIL Achille Francone To cite this version :," 2012.

[68] M. B. Chan-Park, Y. C. Lam, P. Laulia, and S. C. Joshi, "Simulation and

investigation of factors affecting high aspect ratio UV embossing.," *Langmuir*, vol. 21, no. 5, pp. 2000–2007, 2005.

[69] M. Colburn, T. C. Bailey, B. J. B. Choi, J. G. Ekerdt, S. V. Sreenivasan, and C. G. G. Willson, "Development and advantages of step-and-flash lithography," *Solid State Technol.*, 2001.

[70] V. N. Truskett and M. P. C. Watts, "Trends in imprint lithography for biological applications," *Trends Biotechnol.*, vol. 24, no. 7, pp. 312–317, 2006.

[71] S. Takei, T. Ogawa, R. Deschner, and C. G. Willson, "Reduction of pattern peeling in step-and-flash imprint lithography," *Microelectron. Eng.*, vol. 116, pp. 44–50, 2014.

[72] L.-R. Bao, X. Cheng, X. D. Huang, L. J. Guo, S. W. Pang, and A. F. Yee, "Nanoimprinting over topography and multilayer three-dimensional printing," *J. Vac. Sci. Technol. B Microelectron. Nanom. Struct.*, 2002.

[73] A. M. Coclite *et al.*, "CVD Polymers: A New Paradigm for Surface Modifi cation and Device Fabrication," *Adv. Mater.*, 2013.

[74] K. K. Gleason, *CVD Polymers: Fabrication of Organic Surfaces and Devices*. 2015.

[75] K. L. Choy, "Chemical vapour deposition of coatings," *Prog. Mater. Sci.*, vol. 48, no. 2, pp. 57–170, 2003.

[76] S. Fan, M. G. Chapline, N. R. Franklin, T. W. Tombler, A. M. Cassell, and H. Dai, "Self-Oriented Regular Arrays of Carbon Nanotubes and Their Field Emission Properties," *Science (80-.).*, vol. 283, no. 5401, pp. 512–514, 1999.

[77] A. Reina *et al.*, "Large Area, Few-Layer Graphene Films on Arbitrary Substrates by Chemical Vapor Deposition," *Nano Lett.*, vol. 9, no. 1, pp. 30–35, 2009.

[78] R. Yang, E. Goktekin, M. Wang, and K. K. Gleason, "Molecular fouling resistance of zwitterionic and amphiphilic initiated chemically vapor-deposited (iCVD) thin films," *J. Biomater. Sci. Polym. Ed.*, vol. 25, no. 14–15, pp. 1687–1702, 2014.

[79] K. Chan and K. K. Gleason, "Initiated Chemical Vapor Deposition of Linear and Cross-linked Poly(2-hydroxyethyl methacrylate) for Use as Thin-Film Hydrogels," *Langmuir*, vol. 21, no. 19, pp. 8930–8939, 2005.

[80] N. D. Boscher, M. Wang, A. Perrotta, K. Heinze, M. Creatore, and K. K. Gleason, "Metal–Organic Covalent Network Chemical Vapor Deposition for Gas Separation," *Adv. Mater.*, 2016.

[81] M. Wang *et al.*, "CVD Polymers for Devices and Device Fabrication,"

Advanced Materials. 2017.

[82] K. Unger, P. Salzmann, C. Masciullo, M. Cecchini, G. Koller, and A. M. Coclite, "Novel Light-Responsive Biocompatible Hydrogels Produced by Initiated Chemical Vapor Deposition," *ACS Appl. Mater. Interfaces*, vol. 9, no. 20, pp. 17408–17416, 2017.

[83] L. Montero, G. Gabriel, A. Guimerà, R. Villa, K. K. Gleason, and S. Borrós, "Increasing biosensor response through hydrogel thin film deposition: Influence of hydrogel thickness," *Vacuum*, 2012.

[84] M. J. Webber, E. A. Appel, E. W. Meijer, and R. Langer, "Supramolecular biomaterials," *Nature Materials*. 2015.

[85] F. Berthiaume, T. J. Maguire, and M. L. Yarmush, "Tissue Engineering and Regenerative Medicine: History, Progress, and Challenges," *Annu. Rev. Chem. Biomol. Eng.*, vol. 2, no. 1, pp. 403–430, 2011.

[86] R. Katari, A. Peloso, and G. Orlando, "Tissue Engineering and Regenerative Medicine: Semantic Considerations for an Evolving Paradigm," *Front. Bioeng. Biotechnol.*, vol. 2, p. 57, 2015.

[87] D. E. Heath and S. L. Cooper, "The development of polymeric biomaterials inspired by the extracellular matrix," *J. Biomater. Sci. Polym. Ed.*, vol. 28, no. 10–12, pp. 1051–1069, 2017.

[88] H. Peng, X. Liu, R. Wang, F. Jia, L. Dong, and Q. Wang, "Emerging nanostructured materials for musculoskeletal tissue engineering," *Journal of Materials Chemistry B*. 2014.

[89] B. D. Ratner and S. J. Bryant, "Biomaterials: Where We Have Been and Where We Are Going," *Annu. Rev. Biomed. Eng.*, 2004.

[90] R. O. Hynes, "Extracellular matrix: not just prety fibrils," *Science (80-.).*, vol. 326, no. 5957, pp. 1216–1219, 2009.

[91] S. Na *et al.*, "Rapid signal transduction in living cells is a unique feature of mechanotransduction," *Proc. Natl. Acad. Sci.*, 2008.

[92] L. Ramage, "Integrins and extracellular matrix in mechanotransduction," *Cell Health and Cytoskeleton*. 2012.

[93] B. Geiger, J. P. Spatz, and A. D. Bershadsky, "Environmental sensing through focal adhesions," *Nat. Rev. Mol. Cell Biol.*, vol. 10, no. 1, pp. 21–33, 2009.

[94] N. Wang, J. D. Tytell, and D. E. Ingber, "Mechanotransduction at a distance: Mechanically coupling the extracellular matrix with the nucleus," *Nature Reviews Molecular Cell Biology*. 2009.

[95] T. Luo, K. Mohan, P. A. Iglesias, and D. N. Robinson, "Molecular mechanisms of cellular mechanosensing," *Nat. Mater.*, 2013.

[96] G. Baneyx, L. Baugh, and V. Vogel, "Fibronectin extension and unfolding within cell matrix fibrils controlled by cytoskeletal tension.," *Proc. Natl. Acad. Sci. U. S. A.*, 2002.

[97] C. G. Galbraith, K. M. Yamada, and M. P. Sheetz, "The relationship between force and focal complex development," *J. Cell Biol.*, 2002.

[98] K.-I. Wada, K. Itoga, T. Okano, S. Yonemura, and H. Sasaki, "Hippo pathway regulation by cell morphology and stress fibers.," *Development*, 2011.

[99] S. Dupont *et al.*, "Role of YAP/TAZ in mechanotransduction," *Nature*, vol. 474, no. 7350, pp. 179–184, 2011.

[100] K. Baranes, M. Shevach, O. Shefi, and T. Dvir, "Gold Nanoparticle-Decorated Scaffolds Promote Neuronal Differentiation and Maturation," *Nano Lett.*, 2016.

[101] A. Raspa *et al.*, "A biocompatibility study of new nanofibrous scaffolds for nervous system regeneration," *Nanoscale*, 2016.

[102] B. C. J., L. Robert, and B. J. T., "Engineering Substrate Topography at the Micro- and Nanoscale to Control Cell Function," *Angew. Chemie Int. Ed.*, vol. 48, no. 30, pp. 5406–5415.

[103] R. G. Harrison, "The cultivation of tissues in extraneous media as a method of morpho-genetic study," *Anat. Rec.*, 1912.

[104] P. Weiss, "The Problem of Specificity in Growth and Development ," *Yale J. Biol. Med.*, vol. 19, no. 3, pp. 235–278, Jan. 1947.

[105] A. Ferrari *et al.*, "Nanotopographic Control of Neuronal Polarity," 2011.

[106] A. M. Rajnicek, S. Britland, and C. D. McCaig, "Contact guidance of CNS neurites on grooved quartz: influence of groove dimensions, neuronal age and cell type.," *J. Cell Sci.*, 1997.

[107] P. Zorlutuna, N. Hasirci, and V. Hasirci, "Nanopatterned collagen tubes for vascular tissue engineering," *J. Tissue Eng. Regen. Med.*, 2008.

[108] S. A. Biela, Y. Su, J. P. Spatz, and R. Kemkemer, "Different sensitivity of human endothelial cells, smooth muscle cells and fibroblasts to topography in the nano-micro range," *Acta Biomater.*, 2009.

[109] M. J. Dalby, N. Gadegaard, and R. O. C. Oreffo, "Harnessing nanotopography and integrin-matrix interactions to influence stem cell

fate," *Nat. Mater.*, 2014.

[110] S. Tawfick *et al.*, "Engineering of micro- and nanostructured surfaces with anisotropic geometries and properties," *Advanced Materials*. 2012.

[111] D. Hoffman-Kim, J. A. Mitchel, and R. V. Bellamkonda, "Topography, Cell Response, and Nerve Regeneration," *Annu. Rev. Biomed. Eng.*, 2010.

[112] A. T. Nguyen, S. R. Sathe, and E. K. F. Yim, "From nano to micro: Topographical scale and its impact on cell adhesion, morphology and contact guidance," *J. Phys. Condens. Matter*, vol. 28, no. 18, 2016.

[113] M. D. Guillemette *et al.*, "Surface topography induces 3D self-orientation of cells and extracellular matrix resulting in improved tissue function," *Integr. Biol.*, 2009.

[114] M. F. A. Cutiongco, S. H. Goh, R. Aid-Launais, C. Le Visage, H. Y. Low, and E. K. F. Yim, "Planar and tubular patterning of micro and nano-topographies on poly(vinyl alcohol) hydrogel for improved endothelial cell responses," *Biomaterials*, 2016.

[115] A. A. Kulkarni and P. S. Rao, "2 - Synthesis of polymeric nanomaterials for biomedical applications," in *Nanomaterials in Tissue Engineering*, A. K. Gaharwar, S. Sant, M. J. Hancock, and S. A. Hacking, Eds. Woodhead Publishing, 2013, pp. 27–63.

[116] Y. Laroche, V. Storme, J. De Meutter, J. Messens, and M. Lauwereys, "© 199 4 Nature Publishing Group http://www.nature.com/naturebiotechnology," *Nat. Biotechnol.*, vol. 12, pp. 1119–1124, 1994.

[117] F. J. O'Brien, B. A. Harley, I. V Yannas, and L. J. Gibson, "The effect of pore size on cell adhesion in collagen-GAG scaffolds," *Biomaterials*, vol. 26, no. 4, pp. 433–441, 2005.

[118] B. P. Chan and K. W. Leong, "Scaffolding in tissue engineering: General approaches and tissue-specific considerations," *Eur. Spine J.*, vol. 17, no. SUPPL. 4, 2008.

[119] I. Armentano, M. Dottori, E. Fortunati, S. Mattioli, and J. M. Kenny, "Biodegradable polymer matrix nanocomposites for tissue engineering: A review," *Polym. Degrad. Stab.*, vol. 95, no. 11, pp. 2126–2146, 2010.

[120] Y. Tokiwa, B. P. Calabia, C. U. Ugwu, and S. Aiba, "Biodegradability of plastics," *Int. J. Mol. Sci.*, vol. 10, no. 9, pp. 3722–3742, 2009.

[121] M. A. Bokhari, G. Akay, S. Zhang, and M. A. Birch, "The enhancement of osteoblast growth and differentiation in vitro on a peptide hydrogel - PolyHIPE polymer hybrid material," *Biomaterials*, 2005.

[122] J. B. Leach, K. A. Bivens, C. W. Patrick, and C. E. Schmidt, "Photocrosslinked hyaluronic acid hydrogels: Natural, biodegradable tissue engineering scaffolds," *Biotechnol. Bioeng.*, 2003.

[123] B. Chevallay and D. Herbage, "Collagen-based biomaterials as 3D scaffold for cell cultures: Applications for tissue engineering and gene therapy," in *Medical and Biological Engineering and Computing*, 2000.

[124] A. R. Boccaccini and J. J. Blaker, "Bioactive composite materials for tissue engineering scaffolds," *Expert Review of Medical Devices*. 2005.

[125] B. P. Chan *et al.*, "Photochemical Cross-Linking for Collagen-Based Scaffolds: A Study on Optical Properties, Mechanical Properties, Stability, and Hematocompatibility," *Tissue Eng.*, 2007.

[126] G. H. Borschel *et al.*, "Tissue Engineering of Recellularized Small-Diameter Vascular Grafts," *Tissue Eng.*, 2005.

[127] N. Mligiliche, K. Endo, K. Okamoto, E. Fujimoto, and C. Ide, "Extracellular matrix of human amnion manufactured into tubes as conduits for peripheral nerve regeneration," *J. Biomed. Mater. Res.*, 2002.

[128] C. Chai and K. W. Leong, "Biomaterials approach to expand and direct differentiation of stem cells," *Molecular Therapy*. 2007.

[129] M. H. Zheng, J. Chen, Y. Kirilak, C. Willers, J. Xu, and D. Wood, "Porcine small intestine submucosa (SIS) is not an acellular collagenous matrix and contains porcine DNA: Possible implications in human implantation," *J. Biomed. Mater. Res. - Part B Appl. Biomater.*, 2005.

[130] J. Yang *et al.*, "Reconstruction of functional tissues with cell sheet engineering," *Biomaterials*. 2007.

[131] T. Shimizu, "Polysurgery of cell sheet grafts overcomes diffusion limits to produce thick, vascularized myocardial tissues," *FASEB J.*, 2006.

[132] A. Batorsky, J. Liao, A. W. Lund, G. E. Plopper, and J. P. Stegemann, "Encapsulation of adult human mesenchymal stem cells within collagen-agarose microenvironments," *Biotechnol. Bioeng.*, 2005.

[133] B. a Zielinski and P. Aebischer, "Chitosan as a Matrix for Mammalian-Cell Encapsulation," *Biomaterials*, 1994.

[134] C. R. Nuttelman, M. C. Tripodi, and K. S. Anseth, "Synthetic hydrogel niches that promote hMSC viability," *Matrix Biol.*, 2005.

[135] H. Iwata, H. Amemiya, R. Hayashi, S. Fujii, and T. Akutsu, "The use of photocrosslinkable polyvinyl alcohol in the immunoisolation of pancreatic islets," *Transplant. Proc.*, vol. 22, no. 2, p. 797—799, Apr. 1990.

[136] R. P. Lanza, J. L. Hayes, and W. L. Chick, "Encapsulated cell technology," *Nat. Biotechnol.*, 1996.

[137] G. Orive *et al.*, "Cell encapsulation: Promise and progress," *Nature Medicine*. 2003.

[138] T. M. Chang, "Hybrid artificial cells: microencapsulation of living cells.," *ASAIO J.*, 1992.

[139] X. Gu, F. Ding, and D. F. Williams, "Neural tissue engineering options for peripheral nerve regeneration," *Biomaterials*, vol. 35, no. 24, pp. 6143–6156, 2014.

[140] D. CINTEZA, I. PERSINARU, B. M. MACIUCEANU ZARNESCU, D. IONESCU, and I. LASCAR, "Peripheral Nerve Regeneration – an Appraisal of the Current Treatment Options," *Mædica*, vol. 10, no. 1, pp. 65–68, Mar. 2015.

[141] D. P. Kuffler, "An assessment of current techniques for inducing axon regeneration and neurological recovery following peripheral nerve trauma," *Prog. Neurobiol.*, vol. 116, pp. 1–12, 2014.

[142] J. Du, H. Chen, L. Qing, X. Yang, and X. Jia, "Biomimetic neural scaffolds: A crucial step towards optimal peripheral nerve regeneration," *Biomater. Sci.*, vol. 6, no. 6, pp. 1299–1311, 2018.

[143] G. Koopmans, B. Hasse, and N. Sinis, "Chapter 19: The role of collagen in peripheral nerve repair," *Int Rev Neurobiol*, 2009.

[144] S. Geuna *et al.*, "Chapter 3 Histology of the Peripheral Nerve and Changes Occurring During Nerve Regeneration," vol. 87, Academic Press, 2009, pp. 27–46.

[145] E. Kijeńska, M. P. Prabhakaran, W. Swieszkowski, K. J. Kurzydlowski, and S. Ramakrishna, "Interaction of Schwann cells with laminin encapsulated PLCL core–shell nanofibers for nerve tissue engineering," *Eur. Polym. J.*, vol. 50, pp. 30–38, 2014.

[146] S. K. Lee and S. W. Wolfe, "[REVIEWED] Peripheral nerve injury and repair," *J. Am. Acad. Orthop. Surg.*, vol. 8, no. 4, pp. 243–252, 1999.

[147] Z.-L. Chen, W.-M. Yu, and S. Strickland, "Peripheral regeneration," *Annual Review of Neuroscience*, vol. 30. pp. 209–233, 2007.

[148] A. Faroni, S. A. Mobasseri, P. J. Kingham, and A. J. Reid, "Peripheral nerve regeneration: Experimental strategies and future perspectives," *Adv. Drug Deliv. Rev.*, vol. 82–83, pp. 160–167, 2015.

[149] G. R. Evans, "Peripheral nerve injury: a review and approach to tissue

engineered constructs.," *Anat. Rec.*, 2001.

[150] S. J. Archibald, J. Shefner, C. Krarup, and R. D. Madison, "Monkey median nerve repaired by nerve graft or collagen nerve guide tube," *J. Neurosci.*, vol. 15, no. 5, pp. 4109–4123, 1995.

[151] X. Jiang, S. H. Lim, H.-Q. Mao, and S. Y. Chew, "Current applications and future perspectives of artificial nerve conduits," *Exp. Neurol.*, vol. 223, no. 1, pp. 86–101, 2010.

[152] F. Stang, G. Keilhoff, and H. Fansa, "Biocompatibility of different nerve tubes," *Materials (Basel).*, vol. 2, no. 4, pp. 1480–1507, 2009.

[153] H. I. Secer, M. Daneyemez, E. Gonul, and Y. Izci, "Surgical repair of ulnar nerve lesions caused by gunshot and shrapnel: results in 407 lesions.," *J. Neurosurg.*, 2007.

[154] M. F. Meek and W. F. A. Den Dunnen, "Porosity of the wall of a Neurolac® nerve conduit hampers nerve regeneration," *Microsurgery*, 2009.

[155] G. C. De Ruiter *et al.*, "Accuracy of motor axon regeneration across autograft, single-lumen, and multichannel poly(lactic-co-glycolic acid) nerve tubes," *Neurosurgery*, 2008.

[156] S. Y. Chew, R. Mi, A. Hoke, and K. W. Leong, "Aligned protein-polymer composite fibers enhance nerve regeneration: A potential tissue-engineering platform," *Adv. Funct. Mater.*, 2007.

[157] X. Wang, W. Hu, Y. Cao, J. Yao, J. Wu, and X. Gu, "Dog sciatic nerve regeneration across a 30-mm defect bridged by a chitosan/PGA artificial nerve graft," *Brain*, vol. 128, no. 8, pp. 1897–1910, 2005.

[158] X. Gu, F. Ding, Y. Yang, and J. Liu, "Construction of tissue engineered nerve grafts and their application in peripheral nerve regeneration," *Prog. Neurobiol.*, vol. 93, no. 2, pp. 204–230, 2011.

[159] L. Jiang, S. Jones, and X. Jia, "Stem Cell Transplantation for Peripheral Nerve Regeneration: Current Options and Opportunities," *Int. J. Mol. Sci.*, vol. 18, no. 1, 2017.

[160] S. Jones, H. Eisenberg, and X. Jia, "Advances and Future Applications of Augmented Peripheral Nerve Regeneration," *Int. J. Mol. Sci.*, 2016.

[161] B. Paolo, R. Mara, G. Stan, and R. P. Gehron, "Bone Marrow Stromal Stem Cells: Nature, Biology, and Potential Applications," *Stem Cells*, vol. 19, no. 3, pp. 180–192.

[162] F. Ding *et al.*, "Use of Tissue-Engineered Nerve Grafts Consisting of a Chitosan/Poly(lactic-co-glycolic acid)-Based Scaffold Included with Bone

Marrow Mesenchymal Cells for Bridging 50-mm Dog Sciatic Nerve Gaps," *Tissue Eng. Part A*, vol. 16, no. 12, pp. 3779–3790, 2010.

[163] N. Hu *et al.*, "Long-term outcome of the repair of 50 mm long median nerve defects in rhesus monkeys with marrow mesenchymal stem cells-containing, chitosan-based tissue engineered nerve grafts," *Biomaterials*, vol. 34, no. 1, pp. 100–111, 2013.

[164] S. Chiung-Chyi, Y. Yi-Chin, and L. Bai-Shuan, "Peripheral nerve repair of transplanted undifferentiated adipose tissue-derived stem cells in a biodegradable reinforced nerve conduit," *J. Biomed. Mater. Res. Part A*, vol. 100A, no. 1, pp. 48–63.

[165] J. H. Gu, Y. H. Ji, E.-S. Dhong, D. H. Kim, and E.-S. Yoon, "Transplantation of adipose derived stem cells for peripheral nerve regeneration in sciatic nerve defects of the rat," *Curr. Stem Cell Res. Ther.*, vol. 7, no. 5, pp. 347–355, 2012.

[166] P. G. di Summa, D. F. Kalbermatten, E. Pralong, W. Raffoul, P. J. Kingham, and G. Terenghi, "Long-term in vivo regeneration of peripheral nerves through bioengineered nerve grafts," *Neuroscience*, vol. 181, pp. 278–291, 2011.

[167] J. Du, H. Chen, K. Zhou, and X. Jia, "Quantitative Multimodal Evaluation of Passaging Human Neural Crest Stem Cells for Peripheral Nerve Regeneration," *Stem Cell Rev.*, vol. 14, no. 1, pp. 92–100, Feb. 2018.

[168] A. R. Nectow, K. G. Marra, and D. L. Kaplan, "Biomaterials for the Development of Peripheral Nerve Guidance Conduits," *Tissue Eng. Part B Rev.*, vol. 18, no. 1, pp. 40–50, 2012.

[169] Y. Yang, W. Zhao, J. He, Y. Zhao, F. Ding, and X. Gu, "Nerve conduits based on immobilization of nerve growth factor onto modified chitosan by using genipin as a crosslinking agent," *Eur. J. Pharm. Biopharm.*, vol. 79, no. 3, pp. 519–525, 2011.

[170] W. Hongkui, Z. Qing, Z. Weijia, L. Qiong, G. Xiaosong, and Y. Yumin, "Repairing rat sciatic nerve injury by a nerve-growth-factor-loaded, chitosan-based nerve conduit," *Biotechnol. Appl. Biochem.*, vol. 59, no. 5, pp. 388–394, 2012.

[171] J. Du and K. J. Yarema, "Carbohydrate engineered cells for regenerative medicine," *Advanced Drug Delivery Reviews*. 2010.

[172] J. Du, P. L. Che, Z. Y. Wang, U. Aich, and K. J. Yarema, "Designing a binding interface for control of cancer cell adhesion via 3D topography and metabolic oligosaccharide engineering," *Biomaterials*, 2011.

[173] P. Villavicencio-Lorini, S. Laabs, K. Danker, W. Reutter, and R. Horstkorte,

"Biochemical engineering of the acyl side chain of sialic acids stimulates integrin-dependent adhesion of HL60 cells to fibronectin," *J. Mol. Med.*, 2002.

[174] H. Kayser, R. Zeitler, C. Kannicht, D. Grunow, R. Nuck, and W. Reutter, "Biosynthesis of a nonphysiological sialic acid in different rat organs, using N-propanoyl-D-hexosamines as precursors," *J. Biol. Chem.*, 1992.

[175] J. J. Pancrazio, F. Wang, and C. A. Kelley, "Enabling tools for tissue engineering," *Biosensors and Bioelectronics*. 2007.

[176] H. Cao, T. Liu, and S. Y. Chew, "The application of nanofibrous scaffolds in neural tissue engineering," *Advanced Drug Delivery Reviews*. 2009.

[177] E. C. Spivey, Z. Z. Khaing, J. B. Shear, and C. E. Schmidt, "The fundamental role of subcellular topography in peripheral nerve repair therapies," *Biomaterials*. 2012.

[178] S. K. Seidlits, J. Y. Lee, and C. E. Schmidt, "Nanostructured scaffolds for neural applications," *Nanomedicine*, vol. 3, no. 2, pp. 183–199, 2008.

[179] J. J. Norman and T. A. Desai, "Methods for fabrication of nanoscale topography for tissue engineering scaffolds," *Ann. Biomed. Eng.*, 2006.

[180] J. C. Rodríguez Hernández, M. S. Sánchez, J. M. Soria, J. L. Gómez Ribelles, and M. M. Pradas, "Substrate chemistry-dependent conformations of single laminin molecules on polymer surfaces are revealed by the phase signal of atomic force microscopy," *Biophys. J.*, 2007.

[181] F. Johansson, P. Carlberg, N. Danielsen, L. Montelius, and M. Kanje, "Axonal outgrowth on nano-imprinted patterns," *Biomaterials*, 2006.

[182] N. Gomez, Y. Lu, S. Chen, and C. E. Schmidt, "Immobilized nerve growth factor and microtopography have distinct effects on polarization versus axon elongation in hippocampal cells in culture," *Biomaterials*, 2007.

[183] E. K. F. Yim, S. W. Pang, and K. W. Leong, "Synthetic nanostructures inducing differentiation of human mesenchymal stem cells into neuronal lineage," *Exp. Cell Res.*, vol. 313, no. 9, pp. 1820–1829, 2007.

[184] J. Y. Lee, C. A. Bashur, A. S. Goldstein, and C. E. Schmidt, "Polypyrrole-coated electrospun PLGA nanofibers for neural tissue applications," *Biomaterials*, 2009.

[185] S. Stokols and M. H. Tuszynski, "The fabrication and characterization of linearly oriented nerve guidance scaffolds for spinal cord injury," *Biomaterials*, 2004.

[186] I. Tonazzini, M. Pellegrini, M. Pellegrino, and M. Cecchini, "Interaction of

leech neurons with topographical gratings : comparison with rodent and human neuronal lines and primary cells Interaction of leech neurons with topographical gratings : comparison with rodent and human neuronal lines and primary cells," 2014.

[187] E. Jacchetti, I. Tonazzini, S. Meucci, F. Beltram, and M. Cecchini, "Microstructured polydimethylsiloxane membranes for peripheral nerve regeneration," *Microelectron. Eng.*, vol. 124, no. July, pp. 26–29, 2014.

[188] I. Tonazzini, E. Jacchetti, S. Meucci, F. Beltram, and M. Cecchini, "Schwann Cell Contact Guidance versus Boundary -Interaction in Functional Wound Healing along Nano and Microstructured Membranes," *Adv. Healthc. Mater.*, vol. 4, no. 12, pp. 1849–1860, 2015.

[189] S. Y. Emelianov, P.-C. Li, and M. O'Donnell, "Photoacoustics for molecular imaging and therapy," *Phys Today*, vol. 62, no. 8, pp. 34–39, 2009.

[190] Y. Qiu and K. Park, "Environment-sensitive hydrogels for drug delivery," *Adv. Drug Deliv. Rev.*, vol. 64, no. SUPPL., pp. 49–60, 2012.

[191] E. Caló and V. V Khutoryanskiy, "Biomedical applications of hydrogels: A review of patents and commercial products," *Eur. Polym. J.*, vol. 65, pp. 252–267, 2015.

[192] M. Eghtedari, A. Oraevsky, J. A. Copland, N. A. Kotov, A. Conjusteau, and M. Motamedi, "High sensitivity of in vivo detection of gold nanorods using a laser optoacoustic imaging system," *Nano Lett.*, 2007.

[193] B. Kang, D. Yu, Y. Dai, S. Chang, D. Chen, and Y. Ding, "Cancer-cell targeting and photoacoustic therapy using carbon nanotubes as 'bomb' agents," *Small*, 2009.

[194] P. Beard, "Biomedical photoacoustic imaging," *Interface Focus*. 2011.

[195] M. A. Hahn, A. K. Singh, P. Sharma, S. C. Brown, and B. M. Moudgil, "Nanoparticles as contrast agents for in-vivo bioimaging: Current status and future perspectives," *Analytical and Bioanalytical Chemistry*. 2011.

[196] L. V. Wang, "Multiscale photoacoustic microscopy and computed tomography," *Nat. Photonics*, 2009.

[197] C. Avigo *et al.*, "Novel organosilicon phantoms as testing material for photoacoustic imaging," *Prog. Biomed. Opt. Imaging - Proc. SPIE*, vol. 9700, pp. 1–8, 2016.

[198] C. Avigo *et al.*, "Organosilicon phantom for photoacoustic imaging," *J. Biomed. Opt.*, 2015.

[199] F. Conti, *Fisiologia medica*. Mc-Graw Hill, 2010.

[200] F. Sabri, M. E. Sebelik, R. Meacham, J. D. Boughter, M. J. Challis, and N. Leventis, "In Vivo Ultrasonic Detection of Polyurea Crosslinked Silica Aerogel Implants," *PLoS One*, 2013.

[201] S. Meucci, "Engineered environments for biomedical applications: anisotropic nanotopographies and microfluidic devices," 2014.

[202] F. Ayers, A. Grant, D. Kuo, D. J. Cuccia, and A. J. Durkin, "Fabrication and characterization of silicone-based tissue phantoms with tunable optical properties in the visible and near infrared domain," vol. 6870, p. 687007, 2008.

[203] M. F. Refojo and F. -L Leong, "Poly(methyl acrylate-co-hydroxyethyl acrylate) hydrogel implant material of strength and softness," *J. Biomed. Mater. Res.*, 1981.

[204] S. H. Baxamusa and K. K. Gleason, "Random Copolymer Films with Molecular-Scale Compositional Heterogeneities that Interfere with Protein Adsorption," *Adv. Funct. Mater.*, vol. 19, no. 21, pp. 3489–3496, 2009.

[205] M. E. Alf, T. A. Hatton, and K. K. Gleason, "Initiated chemical vapor deposition of responsive polymeric surfaces," in *Thin Solid Films*, 2011.

[206] O. Wichterle and D. Lim, "Hydrophilic Gels for Biological Use," *Nature*, vol. 185, p. 117, Jan. 1960.

[207] M. J. Lydon, T. W. Minett, and B. J. Tighe, "Cellular interactions with synthetic polymer surfaces in culture," *Biomaterials*, vol. 6, no. 6, pp. 396–402, 1985.

[208] R. Klein, "Cell sorting during regenerative tissue formation," *Cell*, vol. 143, no. 1, pp. 32–34, 2010.

[209] S. Parrinello *et al.*, "EphB signaling directs peripheral nerve regeneration through Sox2-dependent Schwann cell Sorting," *Cell*, vol. 143, no. 1, pp. 145–155, 2010.

[210] N. Tucher, O. Höhn, H. Hauser, C. Müller, and B. Bläsi, "Characterizing the degradation of PDMS stamps in nanoimprint lithography," *Microelectron. Eng.*, 2017.

[211] J. P. Rolland, E. C. Hagberg, G. M. Denison, K. R. Carter, and J. M. De Simone, "High-resolution soft lithography: Enabling materials for nanotechnologies," *Angew. Chemie - Int. Ed.*, vol. 43, no. 43, pp. 5796–5799, 2004.

[212] J. N. Lee, C. Park, and G. M. Whitesides, "Solvent Compatibility of Poly(dimethylsiloxane)-Based Microfluidic Devices," *Anal. Chem.*, vol. 75, no. 23, pp. 6544–6554, Dec. 2003.

[213] K. M. Choi and J. A. Rogers, "A Photocurable Poly(dimethylsiloxane) Chemistry Designed for Soft Lithographic Molding and Printing in the Nanometer Regime," *J. Am. Chem. Soc.*, vol. 125, no. 14, pp. 4060–4061, Apr. 2003.

[214] L. M. Campos *et al.*, "Highly Versatile and Robust Materials for Soft Imprint Lithography Based on Thiol-ene Click Chemistry," *Adv. Mater.*, vol. 20, no. 19, pp. 3728–3733, 2008.

[215] Z. Li *et al.*, "Hybrid Nanoimprint–Soft Lithography with Sub-15 nm Resolution," *Nano Lett.*, vol. 9, no. 6, pp. 2306–2310, Jun. 2009.

[216] S. S. Williams, S. Retterer, R. Lopez, R. Ruiz, E. T. Samulski, and J. M. Desimone, "High-resolution PFPE-based molding techniques for nanofabrication of high-pattern density, Sub-20 nm features: A fundamental materials approach," *Nano Lett.*, vol. 10, no. 4, pp. 1421–1428, 2010.

[217] B. Ameduri, B. Boutevin, and G. Kostov, "Fluoroelastomers: synthesis, properties and applications," *Prog. Polym. Sci.*, 2001.

[218] J. P. Rolland, R. M. Van Dam, D. A. Schorzman, S. R. Quake, and J. M. DeSimone, "Solvent-Resistant Photocurable 'Liquid Teflon' for Microfluidic Device Fabrication," *J. Am. Chem. Soc.*, vol. 126, no. 8, pp. 2322–2323, Mar. 2004.

[219] C. Masciullo, A. Sonato, F. Romanato, and M. Cecchini, "Perfluoropolyether (PFPE) Intermediate Molds for High-Resolution Thermal Nanoimprint Lithography," *Nanomater. (Basel, Switzerland)*, vol. 8, no. 8, 2018.

[220] I. D. Johnston, D. K. McCluskey, C. K. L. Tan, and M. C. Tracey, "Mechanical characterization of bulk Sylgard 184 for microfluidics and microengineering," *J. Micromechanics Microengineering*, 2014.

[221] T. T. Truong *et al.*, "Soft lithography using acryloxy perfluoropolyether composite stamps," *Langmuir*, 2007.

[222] J. K. Park and S. H. Cho, "Flexible gratings fabricated in polymeric plate using femtosecond laser irradiation," *Opt. Lasers Eng.*, 2011.

[223] H. Cho *et al.*, "Replication of flexible polymer membranes with geometry-controllable nano-apertures via a hierarchical mould-based dewetting," *Nat. Commun.*, vol. 5, no. May 2013, pp. 1–10, 2014.

[224] K. S. Kim, J. H. Kim, H. J. Lee, and S. R. Lee, "Tribology issues in nanoimprint lithography," *Journal of Mechanical Science and Technology*. 2010.

[225] A. Meneghello *et al.*, "Label-free efficient and accurate detection of cystic fibrosis causing mutations using an azimuthally rotated GC-SPR platform," *Anal. Chem.*, vol. 86, no. 23, pp. 11773–11781, 2014.

[226] R. Dell'Anna *et al.*, "Multiscale structured germanium nanoripples as templates for bioactive surfaces," *RSC Adv.*, 2017.

[227] W. L. Chan and E. Chason, "Making waves: Kinetic processes controlling surface evolution during low energy ion sputtering," *J. Appl. Phys.*, 2007.

[228] S. Facsko *et al.*, "Formation of ordered nanoscale semiconductor dots by ion sputtering," *Science (80-.).*, 1999.

[229] A. Keller and S. Facsko, "Ion-induced nanoscale ripple patterns on Si surfaces: Theory and experiment," *Materials (Basel).*, 2010.

[230] B. Teshome, S. Facsko, and A. Keller, "Topography-controlled alignment of DNA origami nanotubes on nanopatterned surfaces," *Nanoscale*, 2014.

[231] A. Launay, F. Thominette, and J. Verdu, "Hydrolysis of poly(ethylene terephthalate): a kinetic study," *Polym. Degrad. Stab.*, vol. 46, no. 3, pp. 319–324, 1994.

[232] D. Paszun and T. Spychaj, "Chemical Recycling of Poly Ethylene Terephthalate Wastes," *Ind. Eng. Chem. Res.*, 1997.

[233] M. Cecchini, F. Signori, P. Pingue, S. Bronco, F. Ciardelli, and F. Beltram, "High-resolution poly(ethylene terephthalate) (PET) hot embossing at low temperature: thermal, mechanical, and optical analysis of nanopatterned films.," *Langmuir*, vol. 24, no. 21, pp. 12581–6, 2008.

[234] M. C. Choi, Y. Kim, and C. S. Ha, "Polymers for flexible displays: From material selection to device applications," *Progress in Polymer Science (Oxford)*. 2008.

[235] C. Chollet *et al.*, "The effect of RGD density on osteoblast and endothelial cell behavior on RGD-grafted polyethylene terephthalate surfaces," *Biomaterials*, 2009.

[236] F. Gentile *et al.*, "Cells preferentially grow on rough substrates," *Biomaterials*, 2010.

[237] R. C. De Guzman, J. A. Loeb, and P. J. Vandevord, "Electrospinning of matrigel to deposit a basal lamina-like nanofiber surface," *J. Biomater. Sci. Polym. Ed.*, 2010.

[238] T. Ushiki, S. Hayashi, and C. Ide, "The filamentous meshwork in the Schwann cell basement membrane as revealed by transmission and scanning electron microscopy.," *Arch. Histol. Cytol.*, 1990.

[239] D. Quéré, "Wetting and Roughness," *Annu. Rev. Mater. Res.*, 2008.

[240] M. Lampin, R. Warocquier-Clérout, C. Legris, M. Degrange, and M. F.

Sigot-Luizard, “Correlation between substratum roughness and wettability, cell adhesion, and cell migration,” *J. Biomed. Mater. Res.*, 1997.

[241] A. Atala, R. Lanza, J. A. Thomson, and R. M. Nerem, *Principles of Regenerative Medicine*. 2008.

[242] I. Tonazzini, A. Cecchini, Y. Elgersma, and M. Cecchini, “Interaction of SH-SY5Y cells with nanogratings during neuronal differentiation: Comparison with primary neurons,” *Adv. Healthc. Mater.*, vol. 3, no. 4, pp. 581–587, 2014.

[243] I. Tonazzini, S. Meucci, G. M. Van Woerden, Y. Elgersma, and M. Cecchini, “Impaired Neurite Contact Guidance in Ubiquitin Ligase E3a (Ube3a)-Deficient Hippocampal Neurons on Nanostructured Substrates,” *Adv. Healthc. Mater.*, vol. 5, no. 7, pp. 850–862, 2016.

[244] I. Nagata, N. Nakatsuji, and A. Kawana, “Perpendicular contact guidance of CNS neuroblasts exhibited on artificial microstructures,” *Neurosci. Res. Suppl.*, 1991.

[245] P. Pedraz *et al.*, “Adhesion modification of neural stem cells induced by nanoscale ripple patterns,” *Nanotechnology*, 2016.

[246] A. I. Teixeira, G. A. McKie, J. D. Foley, P. J. Bertics, P. F. Nealey, and C. J. Murphy, “The effect of environmental factors on the response of human corneal epithelial cells to nanoscale substrate topography,” *Biomaterials*, 2006.

[247] J. Albuschies and V. Vogel, “The role of filopodia in the recognition of nanotopographies,” *Sci. Rep.*, vol. 3, 2013.

[248] A. Mogilner and B. Rubinstein, “The Physics of Filopodial Protrusion,” *Biophys. J.*, vol. 89, no. 2, pp. 782–795, 2005.

[249] L. A. Lowery and D. Van Vactor, “The trip of the tip: understanding the growth cone machinery,” *Nat. Rev. Mol. Cell Biol.*, vol. 10, no. 5, pp. 332–343, May 2009.

[250] M. Cecchini, G. Bumma, M. Serresi, and F. Beltram, “PC12 differentiation on biopolymer nanostructures,” *Nanotechnology*, vol. 18, no. 50, 2007.

[251] M. Cecchini, A. Ferrari, and F. Beltram, “PC12 polarity on biopolymer nanogratings,” *J. Phys. Conf. Ser.*, vol. 100, no. 1, pp. 1–4, 2008.

[252] A. Ferrari, P. Faraci, M. Cecchini, and F. Beltram, “The effect of alternative neuronal differentiation pathways on PC12 cell adhesion and neurite alignment to nanogratings,” *Biomaterials*, vol. 31, no. 9, pp. 2565–2573, 2010.

[253] A. Ferrari, M. Cecchini, M. Serresi, P. Faraci, D. Pisignano, and F. Beltram, “Neuronal polarity selection by topography-induced focal adhesion

control," *Biomaterials*, 2010.

[254] P. N. Sergi, I. Morana Roccasalvo, I. Tonazzini, M. Cecchini, and S. Micera, "Cell Guidance on Nanogratings: A Computational Model of the Interplay between PC12 Growth Cones and Nanostructures," *PLoS One*, 2013.

[255] Y. Wu, L. Wang, T. Hu, P. X. Ma, and B. Guo, "Conductive micropatterned polyurethane films as tissue engineering scaffolds for Schwann cells and PC12 cells," *J. Colloid Interface Sci.*, vol. 518, pp. 252–262, 2018.

[256] A. Niapour *et al.*, "Novel method to obtain highly enriched cultures of adult rat Schwann cells," *Biotechnol. Lett.*, vol. 32, no. 6, pp. 781–786, 2010.

[257] L. A. Greene and A. S. Tischler, "PC12 Pheochromocytoma Cultures in Neurobiological Research," in *Advances in Cellular Neurobiology*, vol. 3, S. Fedoroff and L. B. T.-A. in C. N. Hertz, Eds. Elsevier, 1982, pp. 373–414.

[258] R. Levi-Montalcini and P. U. Angeletti, "Nerve growth factor.," *Physiol. Rev.*, vol. 48, no. 3, pp. 534–569, Jul. 1968.

[259] A. S. Tischler and J. F. Powers, "Culturing Pheochromocytoma Cells," *Cell Biol. Chromaffin Cell*, pp. 187–190, 2004.

[260] T. P. Driscoll, B. D. Cosgrove, S. J. Heo, Z. E. Shurden, and R. L. Mauck, "Cytoskeletal to Nuclear Strain Transfer Regulates YAP Signaling in Mesenchymal Stem Cells," *Biophys. J.*, vol. 108, no. 12, pp. 2783–2793, 2015.

[261] A. T. Bertrand *et al.*, "Cellular microenvironments reveal defective mechanosensing responses and elevated YAP signaling in LMNA-mutated muscle precursors," *J. Cell Sci.*, vol. 127, no. 13, pp. 2873–2884, 2014.

[262] G. S. Stein *et al.*, "Organitation of transcriptional regulatory machinery in nuclear microenvironments: implications for biological control and cancer.," *Adv. Enzym. Regul.*, vol. 47, pp. 242–250, 2009.

[263] C. H. Thomas, J. H. Collier, C. S. Sfeir, and K. E. Healy, "Engineering gene expression and protein synthesis by modulation of nuclear shape," *Proc. Natl. Acad. Sci.*, vol. 99, no. 4, pp. 1972–1977, 2002.

[264] S. E. Szczesny and R. L. Mauck, "The Nuclear Option: Evidence Implicating the Cell Nucleus in Mechanotransduction," *J. Biomech. Eng.*, vol. 139, no. 2, pp. 21006–21016, Jan. 2017.

[265] I. Tonazzini, S. Meucci, P. Faraci, F. Beltram, and M. Cecchini, "Neuronal differentiation on anisotropic substrates and the influence ofnanotopographical noise on neurite contact guidance," *Biomaterials*, vol. 34, no. 25, pp. 6027–6036, 2013.

[266] B. Geiger, A. Bershadsky, R. Pankov, and K. M. Yamada, "Transmembrane

crosstalk between the extracellular matrix and the cytoskeleton," *Nat. Rev. Mol. Cell Biol.*, vol. 2, p. 793, Nov. 2001.

[267] D. Pesen and D. B. Haviland, "Modulation of Cell Adhesion Complexes by Surface Protein Patterns," *ACS Appl. Mater. Interfaces*, vol. 1, no. 3, pp. 543–548, Mar. 2009.

[268] M. Arnold *et al.*, "Cell interactions with hierarchically structured nano-patterned adhesive surfaces," *Soft Matter*, vol. 5, no. 1, pp. 72–77, Jan. 2009.

[269] C. W. Kuo, D.-Y. Chueh, and P. Chen, "Investigation of size-dependent cell adhesion on nanostructured interfaces," *J. Nanobiotechnology*, vol. 12, p. 54, Dec. 2014.

[270] E. I. Liang, E. J. Mah, A. F. Yee, and M. A. Digman, "Correlation of focal adhesion assembly and disassembly with cell migration on nanotopography," *Integr. Biol.*, vol. 9, no. 2, pp. 145–155, 2017.

[271] R. Zaidel-Bar, C. Ballestrem, Z. Kam, and B. Geiger, "Early molecular events in the assembly of matrix adhesions at the leading edge of migrating cells," *J. Cell Sci.*, vol. 116, no. 22, pp. 4605–4613, 2003.

[272] R. Zaidel-Bar, M. Cohen, L. Addadi, and B. Geiger, "Hierarchical assembly of cell-matrix adhesion complexes," *Biochem. Soc. Trans.*, vol. 32, no. 3, pp. 416–420, 2004.

[273] T. P. Lele, J. Pendse, S. Kumar, M. Salanga, J. Karavitis, and D. E. Ingber, "Mechanical forces alter zyxin unbinding kinetics within focal adhesions of living cells," *J. Cell. Physiol.*, vol. 207, no. 1, pp. 187–194, Apr. 2006.

[274] Y.-C. Chang, P. Nalbant, J. Birkenfeld, Z.-F. Chang, G. M. Bokoch, and P. Forscher, "GEF-H1 Couples Nocodazole-induced Microtubule Disassembly to Cell Contractility via RhoA," *Mol. Biol. Cell*, vol. 19, no. 5, pp. 2147–2153, Feb. 2008.

[275] Y. Poitelon *et al.*, "YAP and TAZ control peripheral myelination and the expression of laminin receptors in Schwann cells," *Nat. Neurosci.*, vol. 19, no. 7, pp. 879–887, 2016.

[276] C. Yang, M. W. Tibbitt, L. Basta, and K. S. Anseth, "Mechanical memory and dosing influence stem cell fate," *Nat. Mater.*, vol. 13, p. 645, Mar. 2014.

[277] A. Ferrari *et al.*, "Nanotopographic control of neuronal polarity," *Nano Lett.*, 2011.

[278] S. Meucci, I. Tonazzini, F. Beltram, and M. Cecchini, "Biocompatible noisy nanotopographies with specific directionality for controlled anisotropic cell cultures," *Soft Matter*, vol. 8, no. 4, pp. 1109–1119, 2012.

[279] R. Sunyer *et al.*, "Collective cell durotaxis emerges from long-range intercellular force transmission," *Science (80-.).*, 2016.

[280] G. Stefopoulos, F. Robotti, V. Falk, D. Poulikakos, and A. Ferrari, "Endothelialization of Rationally Microtextured Surfaces with Minimal Cell Seeding Under Flow," *Small*, vol. 12, no. 30, pp. 4113–4126, 2016.

[281] S. Bottan *et al.*, "Surface-structured bacterial cellulose with guided assembly-based biolithography (GAB)," *ACS Nano*, 2015.

[282] D. Franco *et al.*, "Control of initial endothelial spreading by topographic activation of focal adhesion kinase," *Soft Matter*, 2011.

[283] A. Ferrari, A. Veligodskiy, U. Berge, M. S. Lucas, and R. Kroschewski, "ROCK-mediated contractility, tight junctions and channels contribute to the conversion of a preapical patch into apical surface during isochoric lumen initiation," *J. Cell Sci.*, vol. 121, no. 21, p. 3649 LP-3663, Nov. 2008.

[284] S. Jungbauer, H. Gao, J. P. Spatz, and R. Kemkemer, "Two characteristic regimes in frequency-dependent dynamic reorientation of fibroblasts on cyclically stretched substrates," *Biophys. J.*, 2008.

[285] M. Panagiotakopoulou, M. Bergert, A. Taubenberger, J. Guck, D. Poulikakos, and A. Ferrari, "A Nanoprinted Model of Interstitial Cancer Migration Reveals a Link between Cell Deformability and Proliferation," *ACS Nano*, 2016.